INFERRING ATMOSPHERIC AEROSOL PROPERTIES FROM SATELLITE OBSERVATIONS AND A GLOBAL CHEMICAL TRANSPORT MODEL

by

Melanie S. Hammer

Submitted in partial fulfilment of the requirements
for the degree of Doctor of Philosophy

at

Dalhousie University
Halifax, Nova Scotia
August 2019

Table of Contents

List of Tables

List of Figures

Abstract

Atmospheric aerosols have significant impacts on climate and human health. However, the exact magnitude of the climate and health effects of aerosols remains highly uncertain, due to the large variability in aerosol physical and chemical properties. The use of satellite observations of aerosol properties in conjunction with global chemical transport models can improve our understanding of the interactions of aerosols with radiation and their impacts on health.

Using GEOS-Chem coupled with a radiative transfer model, we develop a global simulation of the Ultraviolet Aerosol Index (UVAI) to interpret satellite UVAI observations. This simulation allows us to constrain the absorption by brown carbon (BrC) aerosol produced from biomass burning. Inclusion of absorption by BrC in GEOS-Chem reduces tropospheric hydroxyl radical by reducing the frequency of the photolysis of ozone. We calculate the direct radiative effect (DRE) of BrC, and find that absorbing BrC changes the global annual mean all-sky top of atmosphere DRE by +0.03 W m^{-2} and all-sky surface DRE by −0.08 W m^{-2}.

We interpret trends in satellite observed UVAI values using our UVAI simulation for 2005-2015 to improve our understanding of trends in global aerosol composition. Trends in absorption by dust dominate the simulated UVAI trends over desert regions. The UVAI simulation underestimates positive UVAI trends over Central Asia, possibly due to an increasing dust source from the desiccating Aral Sea that may not yet be represented by models. Trends in absorption by BrC dominate UVAI trends over biomass burning regions. Trends in scattering by secondary inorganic aerosol dominate UVAI trends over the eastern United States and eastern India.

We estimate surface $PM_{2.5}$ concentrations using information from satellites, simulation, and ground monitors for the years 2000-2017. These combined $PM_{2.5}$ estimates benefit from recent updates to satellite AOD sources, developments in chemical transport models, and expanded ground monitor measurements. We find improved agreement between our $PM_{2.5}$ estimates and ground monitors versus prior work. We use our improved estimates to calculate trends in $PM_{2.5}$ both globally and regionally in order to understand the exposures of the global population.

List of Abbreviations and Symbols Used

Symbol	Units	Description
A	m^2	Cross-Sectional Area
AAE		Absorbing Angstrom Exponent
AAOD		Aerosol Absorption Optical Depth
AERONET		Aerosol Robotic Network
AFCID		Anthropogenic, Fugitive, Combustion, and Industrial Dust
AOD		Aerosol Optical Depth
BC		Black Carbon
b_{ext}	m^{-1}	Extinction Coefficient
Br-SOA		Brown Secondary Organic Aerosol
BRAVO		Big Bend Regional AEROSOL and Visibility Observational Study
BrC		Brown Carbon
C6		Collection 6
C6.1		Collection 6.1
CALIOP		Cloud-Aerosol Lidar with Orthogonal Polarization
χ		Size Parameter
CO_2		Carbon Dioxide
CTM		Chemical Transport Model
DB		Deep Blue
DMS		Dimethyl Sulfide
DRE		Direct Radiative Effect
DRF		Direct Radiative Forcing
DT		Dark Target
EDGAR		Emissions Database for Global Atmospheric Research
EMEP		European Monitoring and Evaluation Programme
η		Simulated Relationship of PM25 to AOD
GADS		Global Aerosol Dataset
GEMS		Geostationary Environment Monitoring Spectrometer
GEOS		Goddard Earth Observation System
GFED		Global Fire Emissions Database
GLS		Generalized Least-Squares Regression
GMAO		Global Modeling and Assimilation Office
GWR		Geographically Weighted Regression
HNO_3		Nitric Acid
I	$W\ m^{-2}$	Radiance

I_0	W m^{-2}	Incident Radiance
IR		Infrared
$J(O^1D)$	s^{-1}	Ozone Photolysis Frequency
$k(\lambda)$		Imaginary Part of the Complex Refractive Index
λ	nm	Wavelength
LER		Lambert Equivalent Reflectivity
LUR		Land Use Regression
LW		Longwave
M	kg m^{-2}	Column Mass Loading
MAIA		Multi-Angle Imager for Aerosols
MAIAC		Multi-Angle Implementation of Atmospheric Correction
MERRA		Modern-Era Retrospective Analysis for Research and Applications
MISR		Multi-angle Imaging Spectroradiometer
MODIS		Moderate Resolution Imaging Spectroradiometer
$N(\lambda)$		Complex Refractive Index
$n(\lambda)$		Real Part of the Complex Refractive Index
NASA		National Aeronautics and Space Administration
NEI		National Emissions Inventory
NH_3		Ammonia
NO		Nitrogen Oxide
NO_3		Nitrogen Dioxide
NO_x		Nitrogen Oxides
NRMSD		Normalized Root Mean Square Difference
O_3		Ozone
OA		Organic Aerosol
OC		Organic Carbon
OH		Hydroxyl Radical
OMAERUV		OMI Near-UV Algorithm
ω		Single Scattering Albedo
OMI		Ozone Monitoring Instrument
π		~3.1415926535
$PM_{2.5}$	μg m^{-3}	Fine Particulate Matter
POA		Primary Organic Aerosol
POC		Primary Organic Carbon
Q_{ext}		Extinction Efficiency
Q_{scat}		Scattering Efficiency
r	m	Particle Radius
R^2		Correlation Coefficient

r_{eff}		Effective Radius
ρ	kg m^{-3}	Particle Density
RMSE		Root Mean Square Error
RRTMG		Rapid Raditive Transfer Model for General Circulation Models

Acknowledgements

This work would not have been possible without the invaluable insight and guidance from my supervisor Dr. Randall Martin. I would like to thank him for all of the incredible knowledge he has shared throughout my degree. I would also like to thank my thesis committee, Dr. Glen Lesins and Dr. Rachel Chang, for their guidance and insight.

The members of my research group have been such an incredible resource for scientific discussion and technical help. Thank you to Chi Li, Brian Boys, Matthew Cooper, Betty Croft, Crystal Weagle, Colin Lee, Max Manning, Junwei Xu, Jun Meng, and Sajeev Philip for all of your help and support. In particular I would like to thank Aaron van Donkelaar who has been a mentor since the very beginning of my degree and without whom this work, especially Chapter 4, would not have been possible.

I would like to thank all of the external coauthors on my published works for their invaluable contributions; Virginie Buchard, Omar Torres, Robert Spurr, and David Ridley. I would also like to thank the anonymous reviewers for their comments.

Thank you to Ross Dickson and Balagopal Pillai for all of their computing help. I would also like to thank Dr. Randall Martin, the Killam Trusts Foundation, National Science and Engineering Research Council (NSERC), and the Nova Scotia government for their financial support.

Chapter 1: Introduction

1.1 Aerosols

Aerosols are solid or liquid particles suspended in Earth's atmosphere. They are emitted from a variety of sources, both natural (e.g. uplifted desert dust, ocean spray,) and anthropogenic (e.g. combustion of fossil fuels). These particles consist of a range of chemical compositions and sizes. The main mechanisms for removal from the atmosphere are wet and dry deposition, giving aerosols atmospheric lifetimes ranging from ~ 1 day to ~ 1 week.

Aerosols have significant climate impacts due to their interactions with solar radiation. Scattering aerosols have a cooling effect as they reflect solar radiation to outer-space. Aerosols that absorb solar radiation have a warming effect on the atmosphere and a cooling effect on the surface. The surface cooling due to the presence of aerosols over the past 45 years is estimated to have masked approximately one third of the warming due to greenhouse gases (Storelvmo et al., 2016), while aerosol absorption is estimated to be the second largest source of atmospheric warming after carbon dioxide (Ramanathan and Carmichael, 2008; Bond et al., 2013; IPCC, 2014; Saleh et al., 2014). Although the radiative effects of aerosols are agreed to be significant, their overall magnitudes remain highly uncertain due to the large variability in aerosol chemical and physical properties as well as their various emission sources (Andreae and Gelencsér, 2006a; Mann and Emanuel, 2006; Mauritsen, 2016). Absorption of ultraviolet (UV) radiation by aerosols also decreases photolysis frequencies, leading to a reduction in the concentrations of atmospheric oxidants (Dickerson et al., 1997; Jacobson, 1998; Liao et al., 2003; Martin et al., 2003).

Aerosols have significant impacts on air quality and human health. Aerosol particles with diameters less than 2.5 μm are commonly referred to as $PM_{2.5}$ (PM for particulate matter). Particles in this size range are sufficiently small that when inhaled they can enter the lungs and be subsequently absorbed into the bloodstream, causing various respiratory and cardiovascular related illnesses. The Global Burden of Disease (GBD) estimates that in 2016, exposure to $PM_{2.5}$ was responsible for 4.1 million deaths worldwide due to heart disease and stroke, lung cancer, chronic lung disease, and respiratory infections, making it the leading environmental risk factor for premature mortality (GBD 2016 Risk Factors Collaborators et al., 2017). The most highly polluted areas are often megacities with high populations, particularly in South and East Asia (HEI, 2018). In recent decades, government regulations for specific air pollutants, including $PM_{2.5}$, along

with emissions controls and technological changes have been remarkably effective at driving air quality improvements in North America and Western Europe, leading to demonstrable increases in life expectancy in these regions (Pope et al., 2009; Turnock et al., 2016). Despite this progress, there still remain many questions regarding the scientific understanding of particulate air pollution and its impacts on health (West et al., 2016).

1.2 Aerosol Species

Aerosols can be emitted directly to the atmosphere as particles, or they can be formed in the atmosphere through gas-to-particle conversion. Aerosols emitted directly as particles are known as primary aerosols while aerosols formed through secondary processes are known as secondary aerosols.

1.2.1 Primary Aerosols

Mineral dust is a main component of natural aerosol and is emitted directly to the atmosphere through wind acting on soil particles. The largest sources are the major desert regions of central Asia and the Sahara-Sahel in North Africa. Although most dust falls out of the atmosphere close to the source, fine dust can be transported long distances to the Caribbean from North Africa and to North America from central Asia (Fairlie et al., 2007). There are also significant anthropogenic dust emissions due to the disturbing of soils by human activities such as land use changes, deforestation, and agriculture (Tegen and Lacis, 1996), as well as anthropogenic fugitive, combustion, and industrial dust from urban sources (Philip et al., 2017). Mineral dust aerosol predominantly absorbs solar radiation and is a substantial contributor to the overall radiative effects of aerosol (Tegen and Lacis, 1996; Sokolik and Toon, 1996, 1999; Colarco et al., 2002) .

Sea salt is another main component of natural aerosol and is emitted to the atmosphere through the bursting of bubbles at the surface of the ocean. Sea salt emissions remain highly uncertain because they are primarily determined by wind speed (Jaeglé et al., 2011). Sea salt aerosols predominantly scatter solar radiation due to their ability to readily uptake water, and significantly affect the global radiation budget over the ocean (Ayash et al., 2008).

Primary carbonaceous aerosols include black carbon (BC) and primary organic carbon (POC) aerosols. Both are predominantly emitted through the combustion of biomass and fossil

fuels. BC has a graphite-like structure and strongly absorbs radiation at all wavelengths (Bergstrom et al., 2002a). POC aerosols are a complex mixture of hundreds of organic compounds; the term "organic carbon" refers only to a fraction of the total organic material because the carbon fraction is typically measured directly (Seinfeld and Pandis, 2006). Measured OC values are multiplied by a conversion factor to obtain the total organic mass. POC emitted from fossil fuel combustion is largely non-absorbing (Saleh et al., 2014), while POC emitted from biomass burning has been found to display absorption that is strongest at ultraviolet wavelengths and decreases into the visible and near-infrared (Kirchstetter et al., 2004; Bergstrom et al., 2007; Yang et al., 2008; Martins et al., 2009; Chen and Bond, 2010; Saleh et al., 2014). This absorbing component of POC is commonly referred to as "brown carbon (BrC)" and is discussed in detail in Chapter 2.

1.2.2 Secondary Aerosols

Secondary inorganic aerosols (SIA) consist of sulfate, nitrate, and ammonium. The main sources of atmospheric sulfate are the oxidation of sulfur dioxide (SO_2) in the gas phase by OH or in cloud droplets by hydrogen peroxide (Adams et al., 1999). SO_2 is emitted to the atmosphere anthropogenically through biomass burning and fossil fuel combustion, and naturally through volcanic activity and the oxidation of oceanic dimethyl sulfide (DMS). Sulfate aerosols can be totally or partially neutralized by ammonia (NH_3) to form ammonium sulfate (Park et al., 2004a). NH_3 is emitted mainly from livestock and fertilizer use. Nitrogen oxides ($NO_x \equiv NO + NO_2$) are emitted to the atmosphere from the combustion of fossil fuel, lightning, soils, and wildfires. NO_x can be oxidized to form nitric acid, which can dissolve directly in an aqueous aerosol solution or react with NH_3 to form ammonium nitrate aerosol, if excess ammonia is available after sulfate neutralization. Secondary inorganic aerosols are highly scattering due to their sizes being in the range of shortwave radiation with highest scattering efficiency, and contribute significantly to the global radiation budget and the cooling effect of aerosols (Schwartz, 1996).

Secondary organic aerosols (SOA) are formed when the atmospheric oxidation products of volatile organic compounds (VOCs) undergo gas-to-particle conversion. The formation of the low volatile (semi-volatile and possibly non-volatile) compounds that make up SOA is governed by a complex series of reactions of a large number of organic species. Overall, SOA formation is dominated by a few classes of VOCs. Biogenic precursors such as monoterpenes, sesquiterpenes, and isoprene are the main contributors in forested areas and on a global scale, while anthropogenic

precursors of aromatic hydrocarbons are the dominate component of SOA in large urban areas (Seinfeld and Pandis, 2006; Hallquist et al., 2009). Biogenic SOA has been found to be largely unabsorbing, while there is evidence of a light absorbing or "brown" SOA formed from aromatic hydrocarbons, however the light absorption properties of SOA remain highly uncertain (Xie et al., 2017).

1.3 Interactions of Aerosols with Radiation

The optical properties of aerosols vary with their chemical composition, hygroscopicity, sizes, and shapes. Mie theory describes the scattering and absorption of radiation by spherical particles. According to Mie theory, the principal parameters that govern the scattering and absorption of light by a particle are the wavelength of the incident light, the particle size, and the wavelength-dependent complex refractive index $N(\lambda)$ (Seinfeld and Pandis, 2006):

$$N(\lambda) = n(\lambda) + ik(\lambda) \tag{1-1}$$

where $n(\lambda)$ is the non-absorbing real part and $k(\lambda)$ is the absorbing imaginary part. Larger values of $k(\lambda)$ are associated with larger absorption. BC exhibits strong absorption at all wavelengths, reflected in its large $k(\lambda)$ values. The refractive index of a particle is determined primarily by its chemical composition.

Particle size can be expressed as the dimensionless size parameter:

$$\chi = \frac{2\pi r}{\lambda} \tag{1-2}$$

where r is the particle radius. χ describes the relationship between particle size and wavelength. The range of χ describes three main scattering regimes:

$\chi << 1$, where the particle is small compared to the wavelength, is the Rayleigh scattering regime. Rayleigh scattering is often referred to as molecular scattering. An ideal atmosphere composed solely of air molecules and free of particles is referred to as a Rayleigh atmosphere. In the Rayleigh regime, the pattern of scattered radiation is symmetrical in the forward and backward directions and the amount of scattered radiation is proportional to λ^{-4}. Therefore small particles scatter light at short wavelengths more efficiently than longer wavelengths.

$\chi \approx 1$, where the particle is approximately the same size as the wavelength, is the Mie scattering regime. It is this regime where scattering is most efficient. SIA aerosols typically lie in this regime for visible radiation, which is why they scatter solar radiation so effectively.

$\chi >> 1$, where the particle is large compared to the wavelength, is the geometric scattering regime. In this regime, the scattering is described by geometrical optics of reflection, refraction, and diffraction, and is strongly dependent on particle shape and orientation relative to the incoming beam. As particle size increases, the amount of radiation scattered in the forward direction increases compared to the backward direction.

The amount of energy removed from an incident beam of light by a particle is described by the wavelength-dependent single particle extinction cross section (units: m^2) , which is equal to the sum of the scattering and absorption cross sections:

$$\sigma_{ext} = \sigma_{scat} + \sigma_{abs} \tag{1-3}$$

The extinction efficiency is the ratio of the extinction cross section and the cross-sectional area of the particle:

$$Q_{ext} = \frac{\sigma_{ext}}{A} \tag{1-4}$$

Then, for a monodisperse ensemble of particles, the extinction coefficient (b_{ext}) can be used to describe the total extinction cross sections of particles per unit volume:

$$b_{ext} = \pi\, r^2\, N\, Q_{ext} \tag{1-5}$$

where r is particle radius and N is the total number concentration (particles per m^{-3}). The integration of the extinction coefficient over a vertical column of the atmosphere gives the total column aerosol optical depth (τ):

$$\tau = \int_0^{z_{TOA}} b_{ext}\, dz \tag{1-6}$$

The aerosol optical depth τ can also be obtained from the column aerosol mass loading per unit area (M), the particle extinction efficiency, the particle density ρ, and the particle effective radius r_{eff} is the effective radius (cross-section weighted radius over the size distribution (Tegen and Lacis, 1996)):

$$\tau = \frac{3\, M Q_{ext}}{4\, \rho\, r_{eff}} \tag{1-7}$$

The attenuation of the initial radiance over a path length z can be given by the Beer-Lambert Law:

$$\frac{I}{dz} = -I_o \, b_{ext} \tag{1-8}$$

which is equivalent to:

$$\frac{I}{I_0} = -\tau \tag{1-9}$$

Therefore the loss of light passing through the atmosphere is equal to the columnar extinction due to the presence of aerosols, i.e. the aerosol optical depth (AOD).

Other parameters helpful for describing the scattering and absorption by aerosols include the single-scatter albedo, ω, which is the ratio of the scattering efficiency to the extinction efficiency Q_{scat}/Q_{ext}. $\omega \approx 1$ indicates a completely scattering particle, while $\omega \approx 0$ indicates a completely absorbing particle. The scattering phase function describes the angular distribution of radiation scattered by a particle, and is the scattered radiance at a particle angle relative to the incident beam normalized by the integral of the scattered radiation at all angles.

1.4 Satellite remote sensing of aerosols

The interactions of aerosols with solar radiation allow for their detection using satellite remote sensing. Satellites measure the top of atmosphere (TOA) radiance. In a cloud free atmosphere, the TOA radiance is influenced by the scattering and absorption by aerosols, absorption by atmospheric gases, scattering by air molecules, and the surface reflectance. The most commonly used metric for aerosol information obtained from satellites is AOD (τ). In order to obtain AOD from satellite measured radiances, it is necessary to make assumptions about parameters such as aerosol size, aerosol chemical composition, and surface reflectivity. Due to the necessity of these assumptions, the calculation of AOD is considered to be a "retrieval" and not a direct measurement. It is therefore not possible to obtain independent information on aerosol composition from satellite AOD retrievals. It is possible to estimate surface concentrations of fine particulate matter $PM_{2.5}$ from satellite AOD using the geophysical relationship between AOD and $PM_{2.5}$ simulated with global Chemical Transport Models (CTMs).

At ultraviolet (UV) wavelengths, interaction of radiation with atmospheric gases is negligible and surface reflectance is very low. Aerosols and air molecules have the primary influence on TOA radiances in the UV. The presence of scattering aerosol increases the TOA UV radiance, while the presence of absorbing aerosol decreases the TOA UV radiance. The Ultraviolet Aerosol Index (UVAI) is a method of detecting aerosol absorption from the ratio of TOA radiances at two UV wavelengths. The UV-absorbing aerosols detected with the UVAI include biomass burning aerosol (black and brown carbon), and desert dust. Because the UVAI is calculated directly from measured radiances, it is therefore possible to obtain independent aerosol composition information. The UVAI is discussed in detail in Chapter 2.

1.5 Chemical Transport Models (CTMs)

Chemical transport models (CTMS) are 3-D numerical models that simulate the processes of transport, chemistry, and emissions to describe the spatial and temporal variability of atmospheric aerosols and gases (Brasseur and Jacob, 2017). They do so by solving the mass conservation continuity equations for atmospheric constituents. CTMs use meteorological information generated from general circulation models or meteorological reanalysis as inputs to represent atmospheric dynamics. In this work we use the 3-D global chemical transport model GEOS-Chem (http://geos-chem.org). GEOS-Chem is an Eulerian model that divides the atmosphere into millions of grid boxes, and solves the mass continuity equations for hundreds of species in each grid box.

1.6 Goals of This Work

In this work we will use satellite observations of aerosol properties in conjunction with the global chemical transport model GEOS-Chem to improve our understanding of the interactions of aerosols with radiation and their impacts on global air quality and human health.

We develop a simulation of the Ultraviolet Aerosol Index (UVAI) using GEOS-Chem coupled with the vector radiative transfer model VLIDORT to interpret UVAI observations from NASA's Ozone Monitoring Instrument (OMI) in Chapter 2. We use this simulation to constrain the absorption by brown carbon (BrC) aerosol produced from biomass burning. We then examine the impacts of the constrained BrC absorption on atmospheric photochemistry and the global radiation budget.

We use our UVAI simulation to interpret trends in OMI observed UVAI values for 2005-2015 in Chapter 3, to improve our understanding of trends in global aerosol composition. We also examine the contributions of individual aerosol species and their trends to the UVAI, improving our understanding of the underlying influence of changes in specific atmospheric constituents to the interactions of aerosols with radiation.

In Chapter 4, we estimate surface $PM_{2.5}$ concentrations using information from satellites, simulation, and ground monitors for the years 2001-2017. We use GEOS-Chem to simulate the geophysical relationship of surface $PM_{2.5}$ and AOD, which is then applied to satellite retrievals of AOD to obtain global estimates of surface $PM_{2.5}$ concentrations. We apply Geographically Weighted Regression (GWR) following van Donkelaar et al. (2016) to incorporate information from ground monitors. These combined $PM_{2.5}$ estimates benefit from recent updates to satellite AOD sources, developments in chemical transport models, and expanded ground monitor measurements.

Chapter 2: Interpreting the Ultraviolet Aerosol Index Observed with the OMI Satellite Instrument to Understand Absorption by Organic Aerosols: Implications for Atmospheric Oxidation and Direct Radiative Effects

2.1 Abstract

Satellite observations of the Ultraviolet Aerosol Index (UVAI) are sensitive to absorption of solar radiation by aerosols; this absorption affects photolysis frequencies and radiative forcing. We develop a global simulation of the UVAI using the 3-D chemical transport model GEOS-Chem coupled with the Vector Linearized Discrete Ordinate Radiative Transfer model (VLIDORT). The simulation is applied to interpret UVAI observations from the Ozone Monitoring Instrument (OMI) for the year 2007. Simulated and observed values are highly consistent in regions where mineral dust dominates the UVAI, but a large negative bias (-0.32 to -0.97) exists between simulated and observed values in biomass burning regions. We determine effective optical properties for absorbing organic aerosol, known as brown carbon (BrC), and implement them into GEOS-Chem to better represent observed UVAI values over biomass burning regions. The addition of absorbing BrC decreases the mean bias between simulated and OMI UVAI values from -0.57 to -0.09 over West Africa in January, from -0.32 to +0.0002 over South Asia in April, from -0.97 to -0.22 over southern Africa in July, and from -0.50 to +0.33 over South America in September. The spectral dependence of absorption after adding BrC to the model is broadly consistent with reported observations for biomass burning aerosol, with Absorbing Angstrom Exponent (AAE) values ranging from 2.9 in the ultraviolet (UV) to 1.3 across the UV-Near IR spectrum. We assess the effect of the additional UV absorption by BrC on atmospheric photochemistry by examining tropospheric hydroxyl radical (OH) concentrations in GEOS-Chem. The inclusion of BrC decreases OH by up to 35% over South America in September, up to 25% over southern Africa in July, and up to 20% over other biomass burning regions. Global annual

mean OH concentrations in GEOS-Chem decrease due to the presence of absorbing BrC, increasing the methyl chloroform lifetime from 5.62 years to 5.68 years, thus reducing the bias against observed values. We calculate the direct radiative effect (DRE) of BrC using GEOS-Chem coupled with the radiative transfer model RRTMG (GC-RT). The addition of absorbing BrC to organic aerosol changes the global annual mean all-sky top of atmosphere (TOA) DRE by +0.05 W m^{-2} and all-sky surface DRE by -0.06 W m^{-2}. Regional changes of up to +0.5 W m^{-2} at TOA and down to -1 W m^{-2} at the surface are found over major biomass burning regions.

2.2 Introduction

Absorption of solar radiation by aerosols plays a major role in radiative forcing and atmospheric photochemistry. Aerosol absorption has been estimated to be the second largest source of radiative forcing after carbon dioxide (Bond et al., 2013; IPCC, 2014; Ramanathan and Carmichael, 2008), although considerable uncertainty remains regarding the magnitude of the forcing (Stier et al., 2007; Wang et al., 2014). Absorption of ultraviolet (UV) radiation by aerosols decreases photolysis frequencies, leading to a reduction in the concentrations of atmospheric oxidants (Dickerson et al., 1997; Jacobson, 1998; Liao et al., 2003; Martin et al., 2003). Many atmospheric chemistry models tend to overestimate tropospheric hydroxyl radical (OH) concentrations compared to observations (Mao et al., 2013; Naik et al., 2013). Accurately representing aerosol absorption could help rectify the discrepancies between simulated and observed OH concentrations, and offer constraints on radiative forcing.

The Ultraviolet Aerosol Index (UVAI) is a method of detecting aerosol absorption using satellite measurements. The UVAI is calculated by separating the spectral contrast of radiances due to aerosol effects from those due to Rayleigh scattering at two wavelengths in the near-UV region (Herman et al., 1997; Torres et al., 1998, 2007). Two attributes of the UVAI method are 1) that aerosol optical properties are more readily detected over surfaces with low reflectance such as found in the UV (Torres et al., 2005), and 2) that the strong interaction between aerosol absorption and molecular scattering in the near-UV increases the sensitivity of UV-radiances to aerosol absorption (Torres et al., 1998). These attributes enhance the ability of the UVAI to detect aerosol absorption that affects UV photolysis and radiative forcing.

Traditionally, black carbon (BC) is treated as the predominant absorbing carbonaceous aerosol, and all organic carbon is assumed to be only very weakly absorbing. However, a growing

number of observations have found evidence of significant absorption by a subset of organic carbon, known as "brown carbon" (BrC), which is strongest in the ultraviolet and decreases into the visible and near-IR wavelength regions (Bergstrom et al., 2007; Chen and Bond, 2010; Kirchstetter et al., 2004; Martins et al., 2009; Yang et al., 2008; Zhong and Jang, 2014). The majority of BrC is emitted to the atmosphere through low-temperature, incomplete combustion of biomass and biofuel (Chen and Bond, 2010; Kirchstetter et al., 2004; Zhong and Jang, 2014). There is evidence of a possible source from residential coal burning (Bond, 2001), while the high-temperature environment associated with other fossil fuel combustion is unfavorable to BrC formation (Andreae and Gelencsér, 2006b; Saleh et al., 2014). BrC has been observed to contribute significantly to the overall absorption by biomass burning aerosol, especially in the UV (Clarke et al., 2007; Corr et al., 2012; Kirchstetter and Thatcher, 2012). The UVAI is sensitive to this absorption (Jethva and Torres, 2011).

Several studies have estimated the direct radiative effect (DRE) and/or direct radiative forcing (DRF) by BrC. In Heald et al. (2014) a clear distinction is made between the DRE, which is the instantaneous imbalance of out-going longwave and incoming shortwave radiation due to the presence of an atmospheric constituent, and the DRF, which is the difference in DRE between present-day and preindustrial conditions. Prior estimates of the change in all-sky top of atmosphere (TOA) DRE from treating organic aerosol as brown rather than weakly absorbing range from +0.04 W m^{-2} to +0.25 W m^{-2} globally (Chung et al., 2012; Feng et al., 2013), with estimates of regional seasonal DRE of organic aerosol including absorbing BrC ranging from +0.5-1 W m^{-2} (Arola et al., 2015). Most studies estimate a TOA DRF between 0.07 and 0.57 W m^{-2} due to absorption by BrC (Lin et al., 2014; Park et al., 2010; Wang et al., 2014). To our knowledge, no chemical transport models have considered the effect of absorption by BrC on atmospheric photochemistry.

In this work we introduce brown carbon to the chemical transport model GEOS-Chem and examine its effect on atmospheric absorption and photochemistry, in particular in known biomass burning regions. To evaluate aerosol absorption, section 2.4 develops a simulation of the UVAI following Buchard et al. (2015) using the Vector Linearized Discrete Radiative Transfer model (VLIDORT) coupled with aerosol fields from GEOS-Chem. Section 2.5 compares the simulated UVAI values to observations from the Ozone Monitoring Instrument (OMI). The change in reflected solar radiation as observed by the UVAI tests the effective representation of the absorption of UV radiation by BrC. Section 2.6 examines the effect of the added BrC absorption

on ozone photolysis frequencies and tropospheric OH concentrations in the GEOS-Chem simulation. Section 2.7 calculates the DRE of absorbing brown carbon. Section 2.8 reports the conclusions.

2.3 Observations

2.3.1 OMI Ultraviolet Aerosol Index

The OMI Ultraviolet Aerosol Index is a method of detecting absorbing aerosols from satellite measurements in the near-UV wavelength region. The UVAI was first observed from the Nimbus-7 TOMS (Total Ozone Mapping Spectrometer) (Herman et al., 1997; Torres et al., 1998) and is currently a product of the OMI Near-UV algorithm (OMAERUV) (Torres et al., 2007). OMI flies on NASA's Aura satellite and has been taking global daily measurements since 2004. The OMAERUV algorithm uses the 354 and 388 nm radiances measured by OMI to calculate the UVAI according to Torres et al. (1998, 2007):

$$\mathrm{UVAI} = -100 \log_{10}\left[\frac{I_{354}^{\mathrm{meas}}}{I_{354}^{\mathrm{calc}}\left(R_{354}^{*}\right)}\right] \tag{2-1}$$

where I_{354}^{meas} is the TOA at 354 nm as measured by OMI, and I_{354}^{calc} is the radiance at 354 nm calculated for a purely Rayleigh scattering atmosphere bounded by a Lambertian surface of reflectance R_{354}^{*}, which is known as the adjusted Lambert Equivalent Reflectivity (LER) (Dave, 1978). R_{354}^{*} is calculated by correcting the LER at 388 nm (R_{388}^{*}) for the spectral dependence of the surface reflectance at 354 nm.

Positive UVAI values indicate absorbing aerosol while negative values indicate non-absorbing aerosol, and near-zero values indicate clouds, minimal aerosol, or other non-aerosol related effects such as unaccounted for land surface albedo wavelength dependence, ocean color effects or specular ocean reflection (i.e. sun glint). These second order effects yield UVAI values ± 0.5 within the noise level (Torres et al., 2007). The OMAERUV product identifies clouds using the measured scene reflectivity and the UVAI (Torres et al., 2013). We reject cloudy conditions (quality flag of 1) to focus on cloud free conditions (quality flag 0).

In this work we use the OMI UVAI to evaluate simulated UVAI values, as described in section 2.4.

2.3.2 Absorption Angstrom Exponent (AAE)

We use observations of the Absorption Angstrom Exponent (AAE) for biomass burning aerosol to test our representation of the spectral dependence of absorption. The AAE is the slope of aerosol absorption optical depth (AAOD) versus wavelength (λ) with intercept k in log-log space. Using the AAE, the AAOD can be related to wavelength with the power-law relationship:

$$\text{AAOD} = k\lambda^{-\text{AAE}} \tag{2-2}$$

Aerosols with spectrally independent absorption display an AAE of about 1, while aerosols with spectrally dependent absorption have an AAE > 1. BC exhibits spectrally independent absorption, and is often accepted as having an AAE close to 1 (Bergstrom et al., 2002b; Bond and Bergstrom, 2006). The AAE over the near-UV to near-IR spectral regions can indicate aerosol type, with urban pollution aerosols dominated by BC exhibiting an AAE near 1, biomass burning aerosols displaying an AAE near 2, and desert dust having an AAE > 2 (Bergstrom et al., 2007; Russell et al., 2009).

Several recent studies have attributed the spectrally dependent absorption by biomass burning aerosols to the presence of BrC (Clarke et al., 2007; Corr et al., 2012; Kirchstetter and Thatcher, 2012; Rizzo et al., 2011; Zhong and Jang, 2014). Kirchstetter et al. (2004) measured over the 300-1000 nm range an AAE of ~ 2 for biomass burning aerosol and an AAE of ~ 1 for motor vehicle aerosol. They found that after extracting the organic carbon from the samples using acetone, the AAE of the biomass burning aerosol decreased to around 1, while the motor vehicle aerosol AAE remained unchanged. They concluded that the spectral dependence of absorption by biomass burning aerosol was due to BrC, while the absorption by motor vehicle emissions was due to BC.

Table 2-1 contains a summary of measured AAE values for biomass burning aerosol. AAE values increase toward UV wavelengths as expected for BrC absorption. Variability in the AAE at visible wavelengths may reflect differences in burn conditions and fuel type. Observations in the ultraviolet, such as the UVAI, offer an exciting opportunity to exploit the large AAE of biomass burning aerosol at short wavelengths to assess the global magnitude of BrC absorption (Jethva and Torres, 2011).

Table 2-1: Absorption Angstrom Exponent (AAE) values for biomass burning regions from the literature.

Wavelength (nm)	AAE value	Region	Reference
350-400 nm			
350-400	2.5-3.0	South America	Jethva and Torres, 2011
350-700 nm			
360-700	1.9	Rural California	Kirchstetter and Thatcher, 2012
450-550 nm			
470-532	1.9	North-central Canada	Corr et al. 2012
470-532	1.4	"	"
Mean ± St. Dev = 1.7 ± 0.35			
400-700 nm			
400-700	1.5-1.9	Laboratory	Schnaiter et al. 2005
440-670	1.8	Boreal Forest	Russell et al. 2010
440-670	1.3	Southern Africa	"
440-670	1.4	South America	"
440-670	1.6	Amazon	"
470-660	1.7	Arctic	Corr et al. 2012
470-660	1.3	Arctic	"
470-660	1.5	Outside Beijing	Yang et al. 2009
470-660	2.1	North America	Clarke et al. 2007
Mean ± St. Dev = 1.6 ±0.26			
450-700 nm			
470-660	2.2	North America	Liu et al. 2015
300-1000 nm			
325-1000	1.1	Southern Africa	Bergstrom et al. 2007
325-1685	1.5	Southern Africa	"
330-1000	2	Southern Africa	Kirchstetter et al. 2004
370-950	1.5	Outside Beijing	Yang et al. 2009
Mean ± St. Dev = 1.5 ± 0.37			
400-1000 nm			
440-870	1.6	Boreal Forest	Russell et al. 2010
440-870	1.3	Southern Africa	"
440-870	1.4	South America	"
440-870	1.4	Amazon	"
440-1020	1.5	Boreal Forest	"
440-1020	1.3	Southern Africa	"
440-1020	1.3	South America	"
440-1020	1.4	Amazon	"
450-950	1.7	Amazon	Rizzo et al. 2011
Mean ± St. Dev = 1.4 ± 0.14			

2.4. Simulated Ultraviolet Aerosol Index

We simulate the UVAI following Buchard et al. (2015) using the VLIDORT model (Spurr, 2006), which includes polarization effects and uses the discrete ordinates method to solve the radiative transfer equation. We supply VLIDORT with the OMI pixel viewing geometry to calculate the UVAI for that pixel. The UVAI values are calculated from TOA radiances computed by VLIDORT at 354 and 388 nm, the wavelengths used by the OMAERUV product.

Following Buchard et al. (2015) we calculate simulated UVAI values as:

$$\mathrm{UVAI} = -\,100 \log_{10}\left[\frac{I_{354}^{\mathrm{RAY+AER}}}{I_{354}^{\mathrm{RAY}}\left(R_{354}^{*}\right)}\right] \tag{2-3}$$

where $I_{354}^{\mathrm{RAY+AER}}$ is the TOA radiance calculated with VLIDORT at 354 nm assuming an atmosphere containing aerosol and Rayleigh effects, and I_{354}^{RAY} is the TOA radiance calculated with VLIDORT at 354 nm assuming a purely Rayleigh scattering atmosphere bounded by a Lambertian surface of reflectance R_{354}^{*} (adjusted Lambert Equivalent Reflectivity).

R_{354}^{*} is calculated by correcting the Lambert Equivalent Reflectivity at 388 nm (R_{388}^{*}) for wavelength dependence:

$$R_{354}^{*} = R_{388}^{*} - (R_{388} - R_{354}) \tag{2-4}$$

where R_{388} and R_{354} are surface reflectance values from a revisited TOMS-based climatology dataset (Torres et al., 2013).

R_{388}^{*} is calculated by relating TOA radiance to diffuse reflectivity using the equation (Buchard et al., 2015):

$$R_{388}^{*} = \frac{I_{388}^{\mathrm{RAY+AER}} - I_{388}^{\mathrm{RAY}}}{T_{388}^{\mathrm{RAY}} + S_{b388}^{\mathrm{RAY}}\left(I_{388}^{\mathrm{RAY+AER}} - I_{388}^{\mathrm{RAY}}\right)} \tag{2-5}$$

where $I_{388}^{\mathrm{RAY+AER}}$ is the TOA radiance calculated with VLIDORT at 388 nm assuming an atmosphere containing aerosol and Rayleigh effects, I_{388}^{RAY} is the TOA radiance at 388 nm calculated with VLIDORT for a purely Rayleigh scattering atmosphere bounded by a Lambertian surface, T_{388}^{RAY} is the simulated transmittance at 388 nm for a Rayleigh atmosphere, and S_{b388}^{RAY} is the spherical albedo of a Rayleigh atmosphere at 388 nm.

For the calculation of TOA radiances, we provide VLIDORT with vertical profiles of aerosol extinction, single scattering albedo, and 32 Legendre-function expansion coefficients of the scattering phase function. We assume all aerosol particles are spherical. We obtain these aerosol optical properties using daily-averaged aerosol fields from GEOS-Chem version 9-01-03 (http://geos-chem.org), a global three dimensional chemical transport model driven by assimilated meteorological data from the Goddard Earth Observation System (GEOS-5) of the NASA Global Modeling and Assimilation Office (GMAO). Our simulation is conducted at a spatial resolution of 2°x2.5° with 47 vertical levels for the year 2007.

GEOS-Chem contains a detailed oxidant-aerosol chemical mechanism (Bey et al., 2001; Park et al., 2004a). The aerosol simulation includes the sulfate-nitrate-ammonium system (Fountoukis and Nenes, 2007; Park et al., 2004a; Pye et al., 2009a), primary carbonaceous aerosol (Park et al., 2003), secondary organic aerosol (Henze et al., 2008; Henze and Seinfeld, 2006; Liao et al., 2007), mineral dust (Fairlie et al., 2007), and sea salt (Jaeglé et al., 2011). Aerosol optical properties are based on the Global Aerosol Data Set (GADS) (Köepke et al., 1997) as implemented by Martin et al., (2003), with updates for organics and secondary inorganics from aircraft observations (Drury et al., 2010), and for mineral dust (Lee et al., 2009; Ridley et al., 2012). We assume all aerosol particles are externally mixed as per the standard treatment used in GEOS-Chem. We treat the density of organic aerosol as 1.3 g cm^{-3} (Duplissy et al., 2011; Kuwata et al., 2012) and assume an organic aerosol mass to organic carbon fraction of 2.1 (Canagaratna et al., 2015).

Anthropogenic emissions are from the EDGAR v32-FT2000 global inventory for 2000 (Olivier et al., 2005) with emissions overwritten in areas with regional inventories for the United States (NEI 2005), Mexico (BRAVO; Kuhns et al., 2005), Europe (EMEP; http://www.emep.int/), and East Asia (Zhang et al., 2009). Emissions are scaled to the year 2007 following emissions of related CO_2 sources as described in van Donkelaar et al. (2008). Global biofuel emissions (Yevich and Logan, 2003), global anthropogenic emissions for carbonaceous aerosols (Bond et al., 2007; Leibensperger et al., 2012), and emissions from open fires for individual years from the GFED3 inventory (Mu et al., 2011) are included.

We calculate UVAI values for two cases. The base case simulation treats the aerosol optical properties as currently implemented in GEOS-Chem in which all organic carbon aerosols

are very weakly absorbing (Table 2-2). The second case adds the more strongly absorbing BrC as described in section 2.5.2 below.

Table 2-2: Imaginary part of the refractive index (k) values for the base case with weakly absorbing "white" organic carbon, and case 2 with brown carbon. Case 2 includes k values associated with multiple densities (ρ), and multiple fractions of brown carbon to primary organic carbon (BrC/POC). All four columns for case 2 yield the same absorption.

	Base Case	**Case 2 with BrC (ρ = 1.3 g cm^{-3})**		**Case 2 with BrC (ρ = 1.8 g cm^{-3})**	
Wavelength (nm)	**BrC/POC = 0**	**BrC/POC = 0.50**	**BrC/POC = 1.0**	**BrC/POC = 0.50**	**BrC/POC=1.0**
300	0.008	0.11	0.051	0.16	0.071
350	0.005	0.077	0.037	0.11	0.051
400	0.005	0.052	0.025	0.073	0.035
450	0.005	0.035	0.014	0.049	0.019
500	0.005	0.023	0.009	0.032	0.013
550	0.006	0.015	0.007	0.021	0.010

2.5 Comparison of simulated and OMI UVAI

2.5.1 Base case simulation

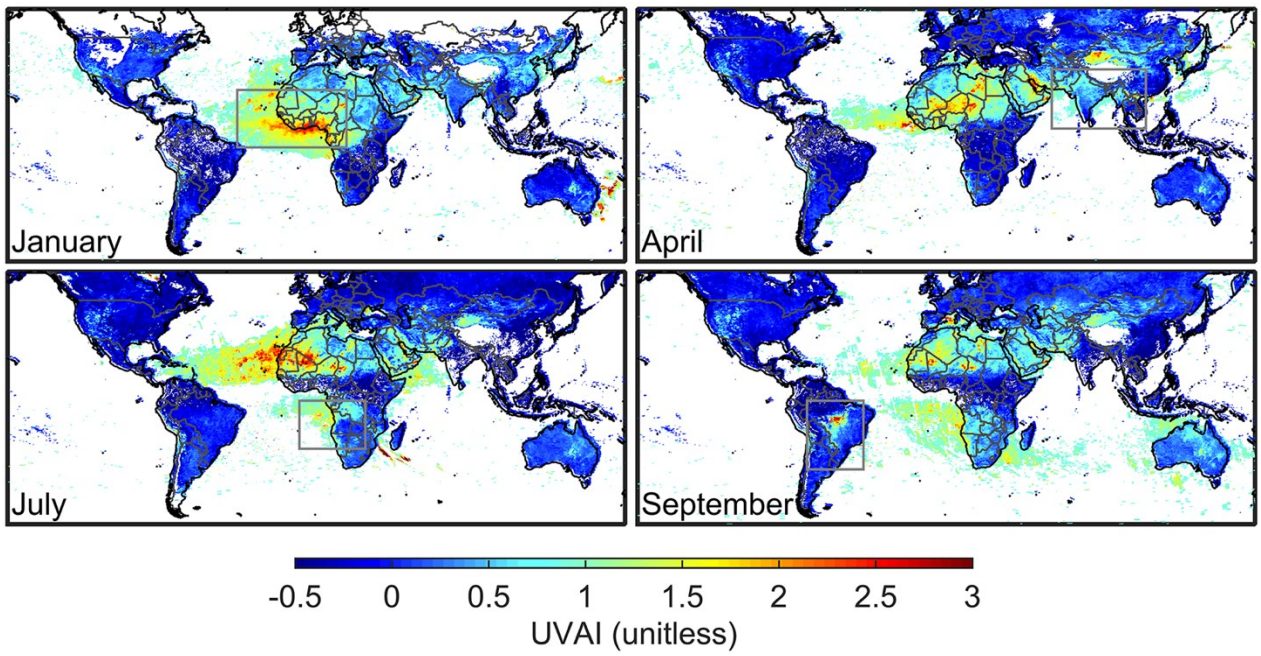

Figure 2-1: Monthly mean Ultraviolet Aerosol Index (UVAI) observations from the OMI satellite instrument for 2007. White space indicates cloud or snow contamination. Grey boxes outline regions examined in Tables 2-3 and 2-4.

Figure 2-1 shows the monthly mean OMI UVAI observations for January, April, July, and September of 2007. Clear signals are apparent over regions dominated by mineral dust and biomass burning (Herman et al., 1997; Torres et al., 1998). Absorption over desert regions occurs for all four months, giving UVAI values between 1 and 3, particularly over the Saharan, Iranian, and Thar deserts. Aerosol absorption from biomass burning primarily follows the seasonal cycle of agricultural burning (Duncan et al., 2003). In January, absorption over West Africa yields UVAI values between 1 and 2.5. In April aerosol absorption is visible over South Asia with UVAI values between 0.5 and 1. UVAI values of 1-1.7 occur over southern Africa in both July and September, while UVAI values of up to 3 occur over South America in September.

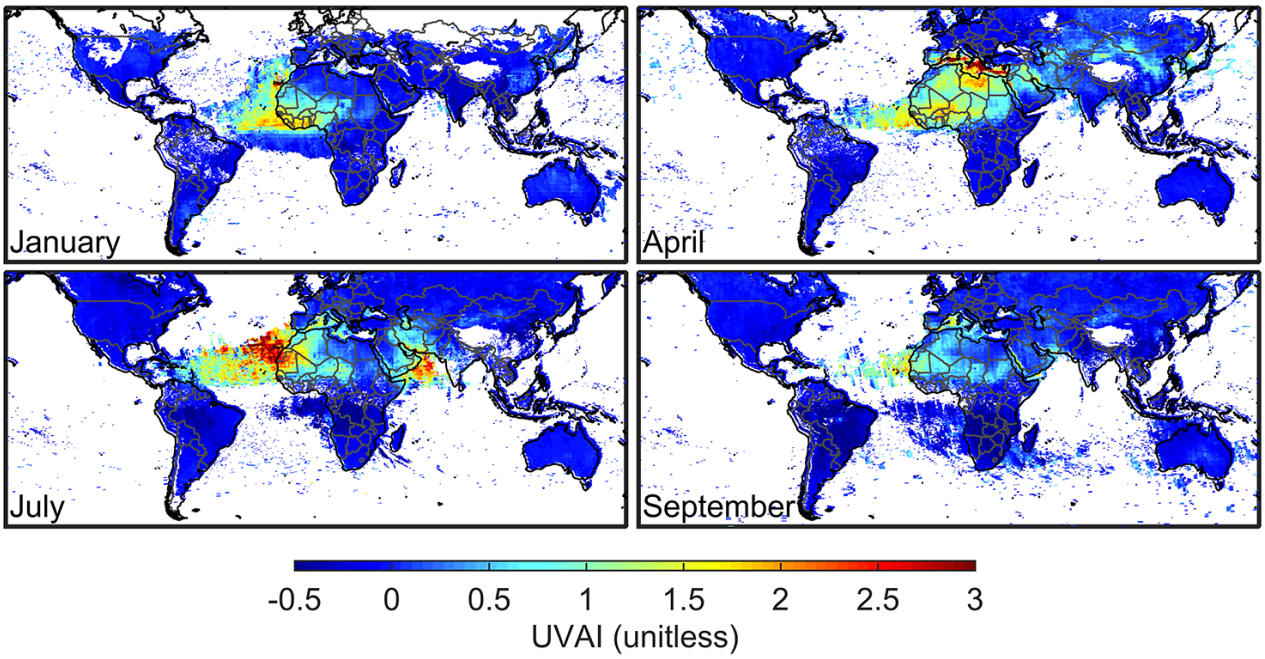

Figure 2-2: Monthly mean UVAI values for 2007 simulated for OMI observing conditions using the vector radiative transfer model VLIDORT coupled with GEOS-Chem aerosol fields for the base case, which treats organic carbon aerosol as weakly absorbing, for 2007. White space indicates cloud or snow contamination.

Figure 2-2 shows the monthly mean UVAI values for our base case simulation, which treats organic carbon aerosol as weakly absorbing. The simulation captures the major absorption features compared to OMI over the desert regions, giving UVAI values of 1-3, however it fails to capture the absorption by biomass burning aerosol, giving UVAI values between -2 and 0 in all biomass burning regions for the four months. These negative values indicate that the UVAI simulation is insensitive to the absorption by BC and is dominated by the scattering from the weakly absorbing

organic carbon aerosol. A sensitivity test with doubled BC concentrations increased UVAI values by only ~0.1. We also conducted a sensitivity test to determine if the heights of the biomass burning plumes could explain the underestimated absorption. Raising the aerosol layer height to unrealistic altitudes (~10 km above the surface) increased the UVAI by only 0.1-0.3, which is insufficient to account for the differences between the simulation and observations.

To further analyze the discrepancies between simulated and observed UVAI, we choose four regions corresponding to the seasonal biomass burning outlined in Figure 2-1: West Africa (5°S-25°N, 40°W-20°E) in January, South Asia (5-35°N, 60-110°E) in April, southern Africa (0-30°S, 5°W-30°E) in July, and South America (0-40°S, 40-70°W) in September. Table 2-3 contains the correlation coefficients (r) between the simulated and OMI UVAI as well as the mean bias (simulated-OMI UVAI). The correlation between the OMI and simulated UVAI is low (0.09-0.48) in all regions, with large mean biases of -0.32 to -0.97

Uncertainty in aerosol optical depth also cannot explain the UVAI bias. Table 4 shows the simulated AOD compared with AOD retrieved from the MODIS (Moderate Resolution Imaging Spectroradiometer) and MISR (Multi-angle Imaging Spectroradiometer) satellite instruments. Overall the simulated values are within the range of satellite retrieved AOD values. The maximum difference in simulated versus satellite AOD is found with the MODIS Dark Target algorithm over South America in September. Matching the simulated AOD to the satellite AOD changed the UVAI by less than 0.1.

We attempt to reconcile the differences between the simulated and OMI UVAI in biomass burning regions by introducing absorbing BrC into GEOS-Chem, as described below.

Table 2-3: Comparison of the simulated versus observed (OMI) UVAI values for the biomass burning regions in the months examined. The base case corresponds to a simulation assuming weakly absorbing organic carbon, while Case 2 corresponds to a simulation including absorbing BrC.

			Mean	Base Case		Case 2 with BrC	
Region[d]	**n[c]**	**Month**	**OMI UVAI**	**r[a]**	**Mean Bias[b]**	**r**	**Mean Bias**
West Africa	381	January	1.25	0.48	-0.57	0.68	-0.09
South Asia	280	April	0.34	0.46	-0.32	0.66	+0.0002
Southern Africa	184	July	0.66	0.09	-0.97	0.63	-0.22
South America	230	September	0.30	0.40	-0.50	0.57	+0.33

[a] r: Pearson correlation coefficient

[b] Mean bias = simulated UVAI – observed UVAI

[c] n = number of GEOS-Chem grid boxes in region

[d] regions are defined in Figure 1

Table 2-4: The mean AOD values for each region from the GEOS-Chem (GC) base case simulation, the MISR instrument, and the MODIS Terra satellite instrument. The MODIS values are included for both the collection 6 Deep Blue and Dark Target algorithms.

	Mean AOD			
Region[a]	**GC**	**MISR**	**MODIS Deep Blue**	**MODIS Dark Target**
West Africa	0.42	0.42	0.45	0.51
South Asia	0.32	0.32	0.30	0.37
Southern Africa	0.19	0.19	0.13	0.24
South America	0.31	0.36	0.39	0.57

[a] regions are defined in Figure 1

2.5.2 Treatment of brown carbon

A great deal of uncertainty exists regarding the fraction of total primary organic carbon that is brown (BrC/POC). This uncertainty arises from the variety of methods used to measure BrC absorption as well as the variable nature of organic aerosols themselves. BrC absorption is often measured by subtracting the absorption attributed to black carbon from the total measured aerosol absorption, and attributing the difference to BrC (e.g. Arola et al., 2011; Yang et al., 2009). Lack and Langridge (2013) argue that this method is subject to the uncertainties associated with the measured absorption of BC as well as the possible presence of absorbing mineral dust. Filter-based measurements where the organic carbon is extracted from the total biomass burning aerosol sample

with the use of solvents provide a more robust estimate (Liu et al., 2013). Chen and Bond (2010) used methanol to extract organic carbon from a variety of burning wood samples generated in a laboratory and found that 92% of the total organic carbon present in the samples was brown. Kirchstetter et al. (2004) extracted organic carbon from biomass burning samples taken in southern Africa using acetone and found that 50-80% of the total organic carbon could be attributed to BrC. A broad range of BrC/POC values have been used to simulate absorption by brown carbon. For example, Feng et al. (2013) assume 66% of primary organic carbon from biomass and biofuel emissions is brown, Wang et al. (2014) assume 50% of POC from biomass and 25% of POC from biofuel emissions is brown, while Lin et al. (2014) assume 100% POC from biomass and biofuel emissions is brown.

Evidence for the existence of brown secondary organic carbon (Br-SOA) also exists. The majority of Br-SOA is from anthropogenic sources (Liu et al., 2013, 2014; Zhang et al., 2013b), while SOA formed from biogenic carbon is only very weakly absorbing (Flores et al., 2014; Liu et al., 2014). On a global scale it is estimated that the majority of SOA is formed from biogenic carbon (Hallquist et al., 2009b; Lack et al., 2004; Tsigaridis and Kanakidou, 2003). Therefore we do not modify the optical properties of SOA. We tested this approach in a sensitivity study by assigning 100% SOA as brown, and found that the contribution to overall absorption by SOA was negligible (UVAI changed by less than 0.1).

Several estimates of BrC absorption exist, but they all differ significantly. The imaginary part of the refractive index (k) for BrC derived by Kirchstetter et al. (2004) and Chen and Bond (2010) are often taken, respectively, as the upper ($k \sim 0.168$ at 350 nm) and lower ($k \sim 0.074$ at 350 nm) limits in modelling studies (Arola et al., 2011; Feng et al., 2013; Lin et al., 2014). Different observations may reflect different burn conditions (Saleh et al., 2014) as well as chemical loss and evaporation of BrC (Forrister et al., 2015; Zhong and Jang, 2014).

Here we apply the OMI UVAI observations to estimate the effective absorption by BrC. We exploit the fact that the TOA radiances used in the OMI UVAI retrievals contain implicit information on the BrC from actual burn conditions, on the BrC that remains after chemical loss or evaporation, on Br-SOA, and on the BrC/POC fraction. We use the term effective to denote the implicit dependence of the UVAI upon these multiple processes. Through sensitivity simulations, we derive the effective k values for BrC and the BrC/POC fraction required to reproduce the

observed absorption by the OMI UVAI. This is accomplished by conducting the sensitivity simulations for several cases of BrC/POC fraction and assuming the same fixed spectral dependence for each case. We then adjust the magnitude of the effective k values to match the OMI UVAI. We treat the relative spectral dependence of k, $\log(\Delta k)/\log(\Delta\lambda)$, as 3 for wavelengths between 300 and 600 nm to represent the mean from laboratory and field measurements of 3.2 ± 0.7 (Kirchstetter et al., 2004; Zhang et al., 2013; Zhong and Jang, 2014). At wavelengths $\geq$ 600 nm we leave the absorption properties of POC unchanged since BrC absorption decreases significantly into the visible and near-IR (Bergstrom et al., 2007; Chen and Bond, 2010; Yang et al., 2008).

The filled circles in Figure 2-3 show the effective k values of BrC derived from seven sensitivity simulations that all achieve the same simulated UVAI. Only the BrC/POC fraction varies between simulations. The choice of simulated UVAI was selected to represent the global OMI UVAI over major biomass burning regions. The imaginary part of the refractive index decreases with increasing wavelength following an exponential relationship as prescribed based on laboratory and field measurements, and decreases with increasing BrC/POC fraction as required to reproduce the OMI UVAI. The effective k values increase with decreasing BrC/POC fraction because as there is less BrC present, in order to match the absorption observed by OMI, the individual BrC particles must become more absorbing in order to counteract the scattering from the remaining fraction of very weakly absorbing organic carbon. Given the smoothly varying

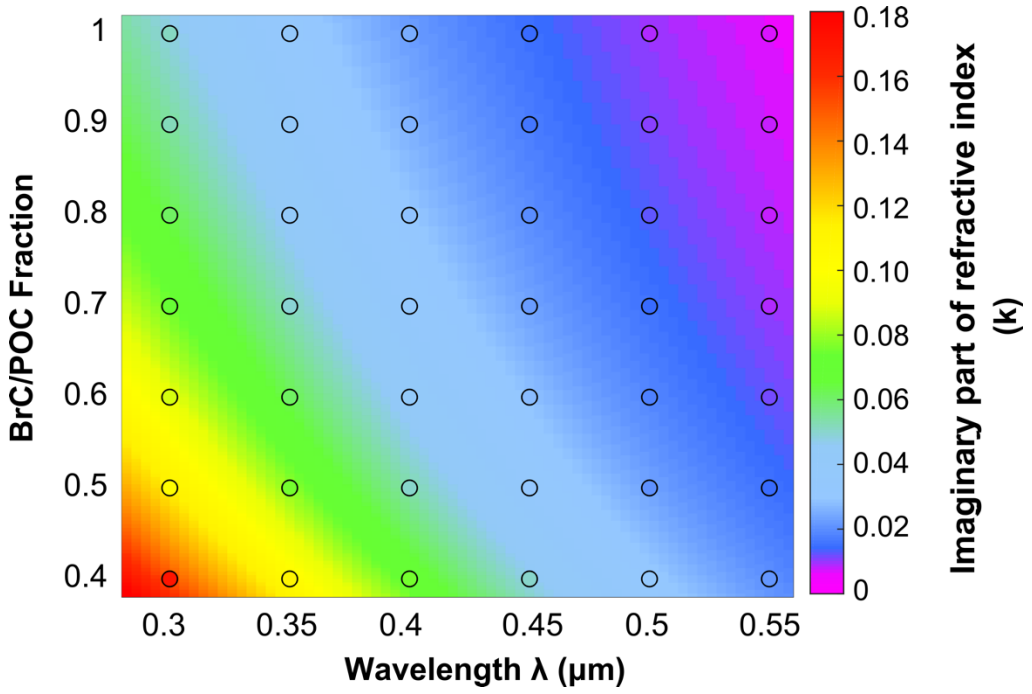

Figure 2-3: Imaginary part of the refractive index (k) values for BrC as a function of wavelength and the fraction of primary organic carbon that is brown (BrC/POC). The background spectrum represents k values calculated using Eq. (6). The filled circles represent the k values obtained from sensitivity simulations. An organic carbon density of 1.3 g cm^{-3} is assumed.

relationship between k and BrC/POC we develop the following expression to represent this relationship:

$$k = c \cdot \rho \cdot \lambda \cdot \left[35.4\left(\frac{BrC}{POC}\right)^{-1.25} \cdot \exp(-10.5\lambda)\right]; \quad \text{BrC/POC} \geq 0.4 \qquad (2\text{-}6)$$

where λ is wavelength (μm), ρ is the density of organic carbon (g μm^{-3}), and c is a conversion constant equal to 1.0x10^{12}/4π μm^2 g^{-1}.

The background spectrum of Figure 2-3 shows the k values calculated using Eq. (2-6). This expression reproduces the full radiative transfer sensitivity simulations with a root mean squared error (RMSE) of 0.004 and a coefficient of determination (r^2) value of 0.99. Equation (2-6) does not apply for BrC/POC fractions less than 0.4 since they do not reproduce the absorption observed by OMI. We emphasize that multiple choices of k and BrC/POC will yield the same TOA radiance and UVAI. The effects on tropospheric OH concentrations and radiative forcing remain unaffected as BrC/POC and effective k vary together, since the distribution of scattering and absorption remains the same.

Table 2-2 contains our derived imaginary parts of the refractive index for BrC/POC fractions of 0.5 and 1.0, compared to the *k* values for the weakly absorbing organic carbon used in our base case simulation. Table 2-2 also contains effective k values derived for an organic carbon density of 1.8 g cm^{-3} which has been assumed in prior studies of BrC. The range of values for k covered by varying the BrC/POC fraction encompasses the range of values for BrC found in the literature (Chen and Bond, 2010; Feng et al., 2013; Kirchstetter et al., 2004; Lin et al., 2014; Sun et al., 2007; Zhang et al., 2013; Zhong and Jang, 2014). The four columns with BrC yield identical wavelength dependent global distributions of scattering and absorption that in turn yield the same UVAI, OH, and DRE.

2.5.3 Simulation including brown carbon

Figure 2-4 shows the monthly mean UVAI values for the simulation including brown carbon for the months of January, April, July, and September of 2007. The simulated absorption features including BrC are much more consistent than the base case simulation at reproducing the OMI UVAI over biomass burning regions (Figure 2-2). The simulated UVAI in the four biomass burning regions now ranges from 0.5-3. As summarized in Table 2-3, the correlation coefficients between the simulated and OMI UVAI for the four biomass burning regions now range from 0.57-0.68, with mean biases of -0.22 to +0.33.

The simulated UVAI using global mean *k* values underestimates the OMI observations for the West Africa and southern Africa regions, but overestimates observations in the South American region. We tested how *k* would need to change to explain the regional UVAI bias if *k* were the only error source. We find that these regional biases could be eliminated by changing *k* at 350 nm by +2% over West Africa, by +10% over southern Africa, and by -30% over South America. The presence of more absorbing BrC over West and southern Africa where savannah fires dominate, and less absorbing over the South America region where forest fires dominate, is consistent with work by Saleh et al. (2014) that found the absorptivity of BrC from biomass burning is greater for flaming fires associated with burning grasslands than for smoldering fires associated with burning forest.

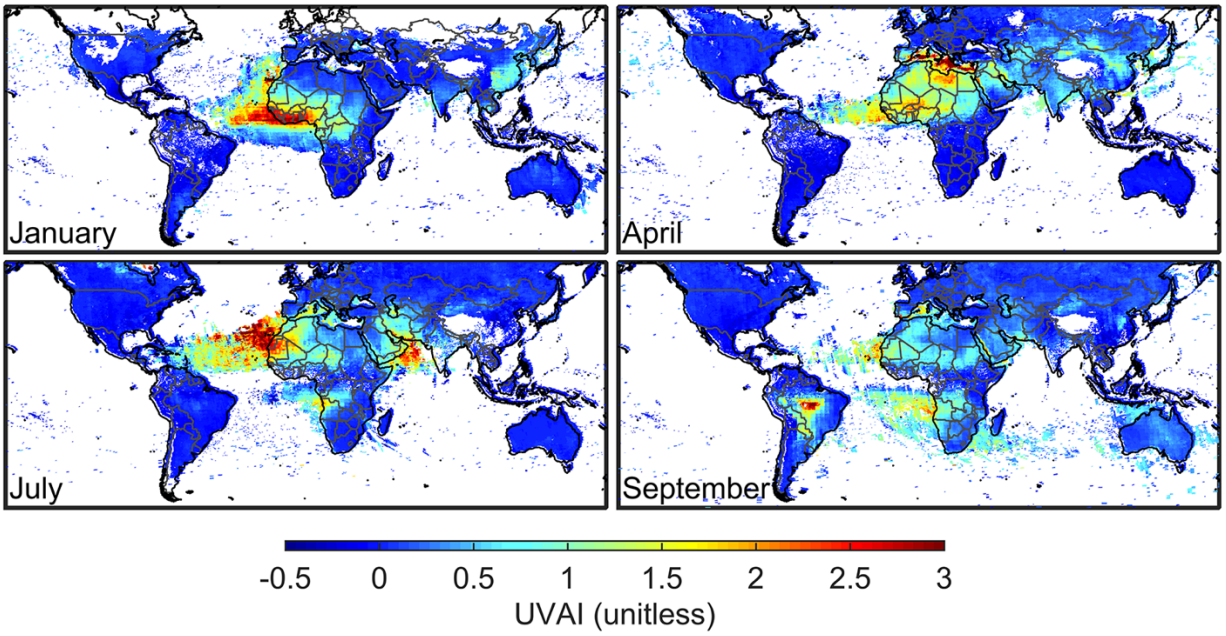

Figure 2-4: Monthly mean UVAI values for 2007 simulated for OMI observing conditions using the vector radiative transfer model VLIDORT coupled with GEOS-Chem aerosol fields for case 2, which assumes the presence of absorbing BrC aerosol. White space indicates clouds or snow contamination.

The absorption in the West and southern Africa cases appears to be concentrated closer to the source for the simulated values (Figure 2-4) compared to the OMI values (Figure 2-1), which show an even distribution of UVAI values away from the source. By contrast, the absorption in the South American region appears to be distributed farther from the source in the simulation than in the OMI observations. Evidence exists of atmospheric photochemical loss and evaporation of brown carbon that causes it to become less absorbing over a lifetime of less than a day (Forrister et al., 2015; Zhong and Jang, 2014). Representing these processes would improve the simulation in the South American region but degrade the simulation in the West Africa and southern Africa regions. Regional treatment of BrC loss processes may be warranted in future work. The current implementation offers our best representation of the effective BrC absorption at the global scale.

Table 2-5 shows the calculated AAE values for biomass burning aerosol (i.e. black carbon + organic carbon aerosol) from our simulations for comparison with the literature values in Table 2-1. Large biases are apparent for the base case simulation without BrC. We evaluate the case 2

Table 2-5: The Absorption Angstrom Exponent (AAE) values for major biomass burning regions and seasons obtained from the base case simulation assuming weakly absorbing organic carbon and the case 2 simulation including absorbing BrC.

Wavelength (nm)	January (West Africa)	April (South Asia)	July (Southern Africa)	September (South America)	Mean ± St. Dev
Base Case					
350-400	1.2	1.2	1.2	1.2	1.2 ± 0.00
350-700	1.0	1.2	1.0	1.1	1.1 ± 0.09
450-550	0.8	1.1	0.7	1.0	0.9 ± 0.18
400-700	1.0	1.2	0.9	1.1	1.1 ± 0.13
450-700	1.0	1.1	0.9	1.0	1.0 ± 0.08
300-1000	0.9	1.1	0.9	0.9	0.9 ± 0.10
400-1000	0.7	0.9	0.7	0.7	0.8 ± 0.10
Case 2					
350-400	2.9	2.5	3	2.9	2.8 ± 0.22
350-700	2.3	2	2.4	2.3	2.2 ± 0.17
450-550	2.5	2.3	2.6	2.6	2.5 ± 0.14
400-700	2.2	1.9	2.2	2.2	2.1 ± 0.15
450-700	1.9	1.7	1.9	1.9	1.8 ± 0.10
300-1000	1.8	1.6	1.8	1.8	1.7 ± 0.15
400-1000	1.3	1.3	1.3	1.3	1.3 ± 0.00

simulation including BrC in detail. For the 350-400 nm wavelength region our mean AAE value of 2.8±0.22 for the four biomass burning regions is within the recommended values of 2.5-3.0 by Jethva and Torres (2011). In the 350-700 nm range our mean AAE of 2.2±0.17 is close to the value of 1.9 from Kirchstetter and Thatcher (2012). The slight positive bias could arise from the fact that Kirchstetter and Thatcher (2012) took their absorption measurements from wood smoke emitted from houses in rural California during the winter, which have different conditions than the tropical open burning considered here. We obtain a mean AAE value of 1.7 ± 0.15 for the 300-1000 nm range, which falls within the literature values of 1.1 to 2. For the 450-550 nm wavelength region, we obtain a mean AAE value of 2.5 ± 0.14, which is biased high compared to the values from Corr et al. (2012) extracted from an examination of biomass burning plumes in North-Central

Canada, where burn conditions differ from the mostly tropical regions considered in our analysis. Over the 400-700 nm region we obtain a mean AAE of 2.1 $\pm$ 0.15, falling within the range of the literature values (1.3-2.1). In the 400-1000 nm region, we obtain a mean AAE value of 1.3 $\pm$ 0.005, which is at the low end of the literature values (1.3-1.7). The overall consistency between observed and simulated AAE provides a measure of confidence in spectral dependence of aerosol optical properties from the UV to the IR. We now examine the implications of this absorption for OH and DRE.

2.6. Analysis of the effect of absorption by BrC on OH concentrations in GEOS-Chem

The strong absorption in the UV by brown carbon aerosol decreases photolysis frequencies, which has implications for ozone photolysis and OH production. Here we examine the effect of the added absorption by BrC on the $O_3 \rightarrow O(^1D)$ photolysis frequency, $J(O(^1D))$, and tropospheric OH concentrations.

Figure 2-5 shows the percent differences in lower tropospheric OH concentrations between the GEOS-Chem simulation including absorbing brown carbon versus the base case simulation with weakly absorbing organic carbon. The most significant decreases correspond with the major biomass burning regions. The addition of BrC decreases OH concentrations by up to 35% over the South American biomass burning region in September and up to 25% over the southern Africa biomass burning region in July. OH concentrations decrease by up to 20% over West Africa in January and southern Africa in September, with decreases of up to 15% over North America in July, South America in July, and South Asia in all four months. The spatial and seasonal pattern of $J(O^1(D))$ differences closely reproduces the changes in OH ($r^2 = 0.85$) (not shown).

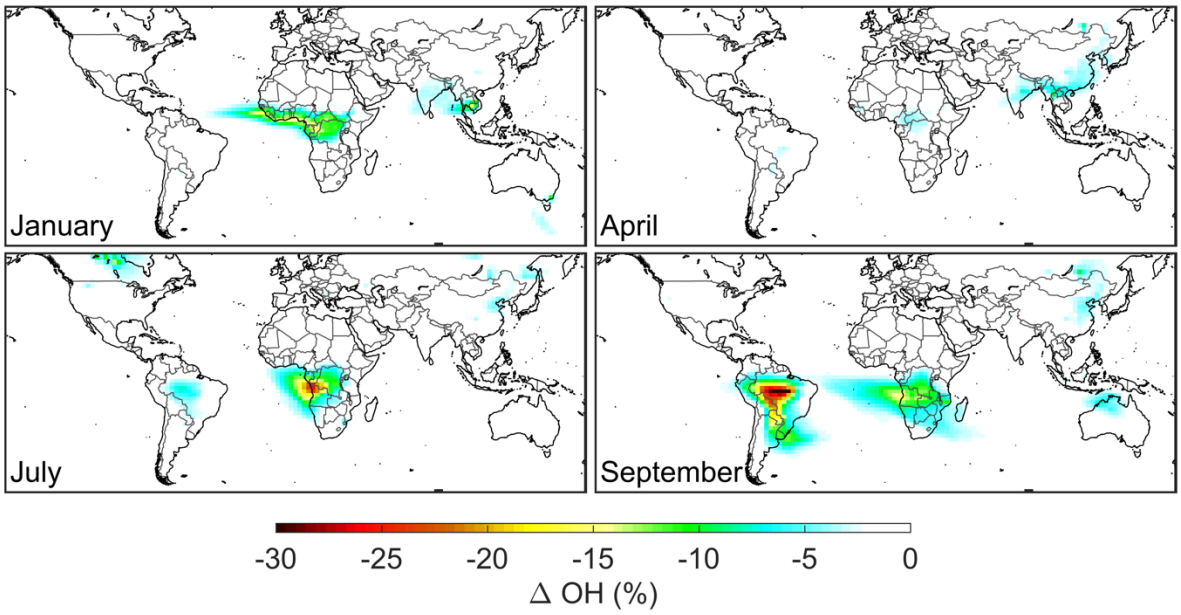

Figure 2-5: Percent difference between OH concentrations in the lower troposphere from a GEOS-Chem simulation including absorbing BrC minus a simulation including weakly absorbing organic carbon. The values are monthly means for January, April, July, and September of 2007.

Methyl chloroform observations provide a valuable constraint on global OH (Prather et al., 2012; Spivakovsky et al., 2000). The addition of BrC to the GEOS-Chem simulation reduces global mean tropospheric OH concentrations. The reduction in global mean OH concentrations increases the methyl chloroform lifetime to tropospheric OH from 5.62 years to 5.68 years. This change is noteworthy given the buffered nature of OH. This change yields better agreement with estimates from observations giving a methyl chloroform lifetime of 6.0 (+0.5, -0.4) years (Prinn et al., 2005).

2.7 Radiative impact of brown carbon

We calculate the direct radiative effect (DRE) of absorbing BrC relative to that of the weakly absorbing organic carbon assumed in our base case simulation. We use GEOS-Chem coupled with the radiative transfer model RRTMG (Iacono et al., 2008), a configuration known as GC-RT, that is described in Heald et al. (2014). GC-RT calculates both the longwave (LW) and shortwave (SW) instantaneous total radiative fluxes as well as the flux differences due to a specific constituent of the atmosphere (e.g. organic aerosol). The DRE is calculated by adding the LW and SW flux differences determined through perturbation of the constituent of interest. Our GC-RT simulations use version 10.1 of GEOS-Chem with the same aerosol emissions described in section 3 (e.g. GFED3 open fire emissions). We calculate the DRE of absorption by BrC as the difference

in the DRE of organic aerosol when including BrC (Case 2) minus the DRE of organic aerosol when assuming weakly absorbing organic carbon (base case). We focus on the DRE rather than the DRF to avoid ambiguity in preindustrial BrC.

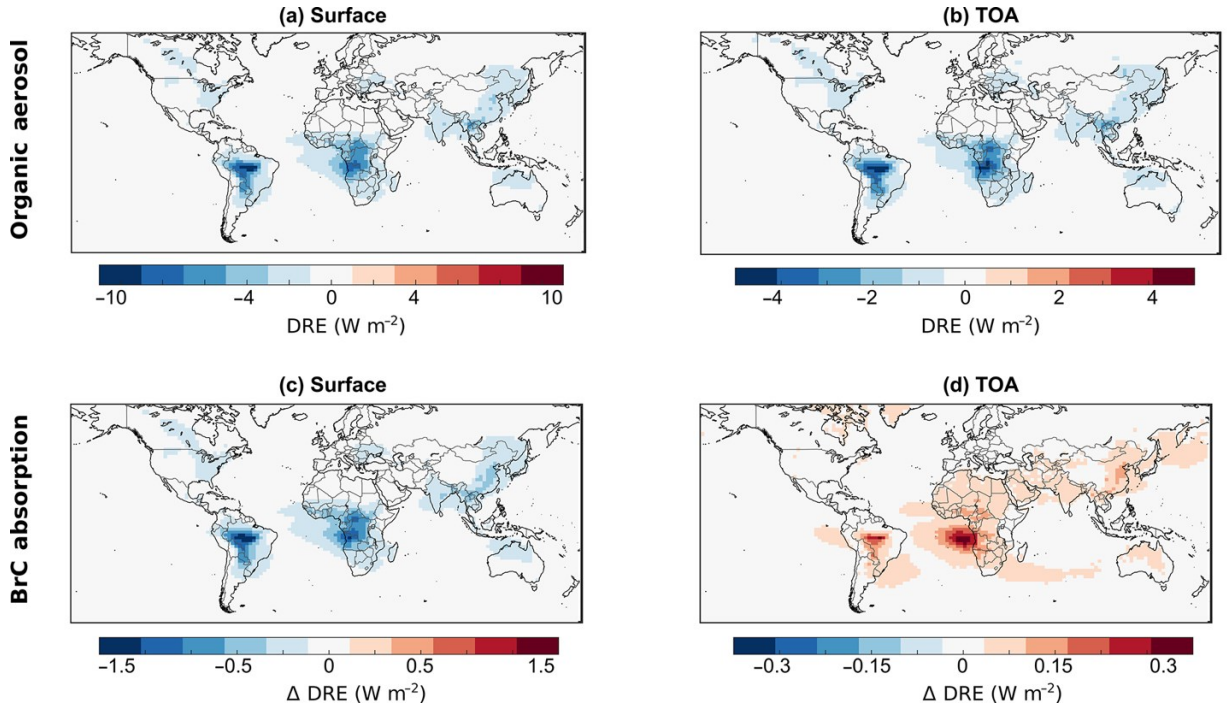

Figure 2-6. Annual mean all-sky DRE values for 2007 (W m^{-2}). The top two panels are the DRE values for organic aerosol from the case 2 simulation including BrC at (a) the surface and (b) TOA. The bottom two panels are the change in DRE values for absorption by BrC calculated as the difference between the DRE values for organic aerosol from the case 2 simulation and the base case simulation (without BrC) at (c) the surface and (d) TOA.

Figure 2-6 shows all-sky DRE values for 2007. The top two panels are the DRE values for organic aerosol from the case 2 simulation including BrC. The overall DRE of organic aerosol including BrC is negative, with the largest effects over major biomass burning regions. The bottom two panels show the DRE for absorption by BrC, calculated as the difference between the DRE of organic aerosol for the case 2 simulation including BrC minus the base case simulation with weakly absorbing organic carbon. At the surface BrC absorption reduces the DRE by -1.25 Wm^{-2} over South America and southern Africa, and by -0.5 to -0.25 Wm^{-2} over South Asia, North America, West Africa, Australia, and Europe. At TOA, BrC absorption reduces the DRE by 0.55 Wm^{-2} over South America and southern Africa, and by 0.1 to 0.25 Wm^{-2} over broad regions. This

overall cooling effect at the surface and a warming effect on the atmosphere is consistent with previous work (e.g. Chen and Bond, 2010).

Table 2-6 contains LW and SW global annual mean flux differences as well as the resulting DRE values for both organic aerosol and brown carbon absorption. The values for organic aerosol are from the base case simulation assuming weakly absorbing organic carbon and the case 2 simulation including BrC, while the values for BrC absorption are calculated as their difference. Absorption by BrC has a mean all-sky DRE at TOA of +0.05 W m^{-2} and at the surface of -0.06 W m^{-2}.

Our findings fall within the range of values from other studies that estimate the DRE of BrC absorption. Feng et al. (2013) introduce absorption by BrC based on the optical properties from Kirchstetter et al. (2004) and Chen and Bond (2010) into a global model, and calculate an all-sky TOA DRE for BrC absorption of 0.04 to 0.11 W m^{-2}, and an all-sky surface DRE for BrC absorption of -0.06 to -0.14 W m^{-2}. Chung et al. (2012) estimate BrC absorption by subtracting the absorption by BC and desert dust from total aerosol AAE values from AERONET to calculate an all-sky TOA DRE for organic aerosol when including BrC between -0.15 and +0.12 W m^{-2} and an all-sky surface DRE between -1.50 and -0.75 W m^{-2}. Arola et al. (2015) use AERONET retrieved imaginary parts of the refractive index for brown carbon at 440, 670, 870, and 1020 nm to estimate over the Indo-Gangetic plain monthly all-sky TOA DRE values for organic aerosol including BrC absorption up to +0.5 W m^{-2} in spring and as low as -1 W m^{-2} in the winter.

Table 2-6: Global annual mean LW and SW flux differences and resulting DRE values for 2007 at TOA and the surface. The values for organic aerosol are shown for both the base case simulation with weakly absorbing organic carbon and the case 2 simulation including absorbing brown carbon. The DRE values for BrC absorption are calculated as the difference between the DRE of organic aerosol from case 2 minus the base case.

	Organic Aerosol		**BrC Absorption**
	Base Case	**Case 2**	**Case 2 – Base Case**
TOA DRE, Clear Sky (Wm^{-2})	-0.41	-0.37	+0.040
LW	+0.0044	+0.0044	
SW	-0.41	-0.37	
TOA DRE, All Sky (Wm^{-2})	-0.30	-0.25	+0.05
LW	+0.0033	+0.0033	
SW	-0.30	-0.25	
Surface DRE, Clear Sky (Wm^{-2})	-0.67	-0.74	-0.07
LW	+0.0076	+0.0076	
SW	-0.67	-0.75	
Surface DRE, All Sky (Wm^{-2})	-0.53	-0.59	-0.06
LW	0.0062	0.0062	
SW	-0.54	-0.60	

2.8. Conclusion

We interpret OMI observations of the Ultraviolet Aerosol Index (UVAI), which provides a measure of absorbing aerosols, by developing a simulation of the UVAI using the vector radiative transfer model VLIDORT coupled with GEOS-Chem aerosol fields. The base case simulation, which treats organic carbon as weakly absorbing, well represents the observed UVAI in most of the world but significantly underestimates the absorption in biomass burning regions. We apply the OMI UVAI to estimate absorption by brown carbon (BrC). This approach exploits the strong absorption by BrC at ultraviolet wavelengths and its effect on top of atmosphere (TOA) radiance. We express the imaginary part of the refractive index of BrC that is required to obtain near-identical TOA radiance values as a function of the fraction of primary organic carbon that is brown. This effective refractive index and effective BrC fraction provide a measure of the degree of browness needed to represent the complex processes (e.g. burn conditions, photochemical loss) affecting global BrC and in turn the UVAI.

The simulation including absorbing BrC is much more consistent than the base case at reproducing the OMI UVAI over biomass burning regions. The mean bias between simulated and OMI UVAI values is reduced from -0.57 to -0.09 over West Africa in January, from -0.32 to +0.0002 over South Asia in April, from -0.97 to -0.22 over southern Africa in July, and from -0.50 to +0.33 over South America in September. The updated optical properties for BrC result in AAE values for biomass burning aerosol ranging from 2.9 in the UV to 1.3 across the UV-Near IR, which are broadly consistent with field observations.

We apply this constraint on ultraviolet absorption to examine implications for the $O_3 \rightarrow O(^1D)$ photolysis frequency. We find that the inclusion of absorbing BrC into GEOS-Chem decreases $J(O(^1D))$ and lower tropospheric OH by up to 35% over South America in September, up to 25% over southern Africa in July, up to 20% over West Africa in January and southern Africa in September, and up to 15% over North America in January, South America in July, and South Asia in all four months. The decrease in global mean OH concentration in GEOS-Chem increases the methyl chloroform lifetime to tropospheric OH from 5.62 years to 5.68 years, which is in better agreement with estimates from observations of 6.0 (+0.5, -0.4) years.

We calculate the direct radiative effect (DRE) of BrC using GEOS-Chem coupled with the radiative transfer model RRTMG (GC-RT). We obtain global annual mean all-sky TOA DRE

values for BrC absorption of 0.05 Wm^{-2} and values of -0.06 Wm^{-2} at the surface. Regional changes of up to +0.5 W m^{-2} at TOA and down to -1 W m^{-2} at the surface are found over major biomass burning regions. Our results are within the range of prior estimates of DRE for BrC absorption.

Ample opportunities exist to further develop the simulations of BrC and more generally of the UVAI. These opportunities include explicitly accounting for the range of processes affecting BrC such as burn conditions, photochemical loss, secondary production, as well as regional treatment of BrC. Interpretation of the long observational record of the UVAI from 1979 to the present should offer constraints on trends in aerosol composition, ultraviolet absorption, and radiative effects. The forthcoming TROPOMI instrument and geostationary constellation (e.g. TEMPO, Sentinel-4, and GEMS) will offer UVAI observations at 5-20 times higher spatial resolution, as well as information on diurnal variation, both of which may offer additional constraints on BrC evolution.

2.9 Acknowledgements: This work was supported by the Natural Science and Engineering Research Council of Canada. Computational facilities were provided in part by the Atlantic Computational Excellence Network consortium of Compute Canada. We thank Farhan Khan for assistance during the early stages of this work.

Chapter 3: Insight into global trends in aerosol composition from 2005 to 2015 inferred from the OMI Ultraviolet Aerosol Index

3.1 Abstract.

Observations of aerosol scattering and absorption offer valuable information about aerosol composition. We apply a simulation of the Ultraviolet Aerosol Index (UVAI), a method of detecting aerosol absorption from satellite observations, to interpret UVAI values observed by the Ozone Monitoring Instrument (OMI) from 2005 to 2015 to understand global trends in aerosol composition. We conduct our simulation using the vector radiative transfer model VLIDORT with aerosol fields from the global chemical transport model GEOS-Chem. We examine the 2005–2015 trends in individual aerosol species from GEOS-Chem and apply these trends to the UVAI simulation to calculate the change in simulated UVAI due to the trends in individual aerosol species. We find that global trends in the UVAI are largely explained by trends in absorption by mineral dust, absorption by brown carbon, and scattering by secondary inorganic aerosol. Trends in absorption by mineral dust dominate the simulated UVAI trends over North Africa, the Middle-East, East Asia, and Australia. The UVAI simulation resolves observed negative UVAI trends well over Australia, but underestimates positive UVAI trends over North Africa and Central Asia near the Aral Sea and underestimates negative UVAI trends over East Asia. We find evidence of an increasing dust source from the desiccating Aral Sea that may not be well represented by the current generation of models. Trends in absorption by brown carbon dominate the simulated UVAI trends over biomass burning regions. The UVAI simulation reproduces observed negative trends over central South America and West Africa, but underestimates observed UVAI trends over boreal forests. Trends in scattering by secondary inorganic aerosol dominate the simulated UVAI trends over the eastern United States and eastern India. The UVAI simulation slightly overestimates the observed positive UVAI trends over the eastern United States and

underestimates the observed negative UVAI trends over India. Quantitative simulation of the OMI UVAI offers new insight into global trends in aerosol composition.

3.2 Introduction

Atmospheric aerosols have significant climate impacts due to their ability to scatter and absorb solar radiation and to their indirect effect through modification of cloud properties. The exact magnitude of the direct radiative forcing remains highly uncertain (IPCC, 2014), although most studies agree it is significant (Andreae and Gelencsér, 2006; Mann and Emanuel, 2006; Mauritsen, 2016). Storelvmo et al. (2016) estimate that changes in global aerosol loading over the past 45 years have caused cooling (direct and indirect) that masks about one-third of the atmospheric warming due to increasing greenhouse gas emissions. Aerosol absorption has been estimated to be the second-largest source of atmospheric warming after carbon dioxide (Ramanathan and Carmichael, 2008; Bond et al., 2013; IPCC, 2014), although considerable uncertainty remains regarding the exact magnitude (Stier et al., 2007). The large uncertainty regarding the direct radiative impacts of aerosols on climate is driven by the large variability in aerosol physical and chemical properties, as well as their various emission sources, making it extremely difficult to fully understand their interactions with radiation (Pöschl, 2005; Moosmüller et al., 2009; Curci et al., 2015; Kristiansen et al., 2016). Global observations of trends in aerosol scattering and absorption would offer valuable constraints on trends in aerosol sources and composition.

The emissions of aerosols and their precursors have changed significantly over the past decade. In North America and Europe, the anthropogenic emissions of most aerosol species (e.g. black carbon, organic aerosols) and aerosol precursors (e.g. sulfur dioxide and nitrogen oxides) have decreased due to pollution controls (Leibensperger et al., 2012; Klimont et al., 2013; Curier et al., 2014; Simon et al., 2015; Xing et al., 2015; Li et al., 2017). By contrast, emissions of aerosols and aerosol precursors have increased in developing countries due to increased industrial activity, particularly in China and India. Chinese emissions of black carbon (BC), organic carbon (OC), and nitrogen oxides (NO_x) have been increasing over the past decade (Cui et al., 2015; Zhao et al., 2013), although in the most recent years NOx emissions have been declining, driven by denitration devices at power plants (Liu et al., 2016a). Due to the wide implementation of flue-gas desulfurization equipment in most power plants in China, emissions of sulfur dioxide (SO_2) in

some regions have been decreasing since about 2006–2008 (Lu et al., 2011; Wang et al., 2015; Fioletov et al., 2016). Indian emissions of anthropogenic aerosols and their precursors have been increasing over the past decade (Lu et al., 2011; Klimont et al., 2017). There have also been significant changes in global dust and biomass burning emissions. Shao et al. (2013) use synoptic data to estimate a global decrease in dust emissions between 1974 and 2012, driven largely by reductions from North Africa with weaker contributions from Northeast Asia, South America, and South Africa. By examining trends in burned area, Giglio et al. (2013) estimate a decrease in global biomass burning emissions between 2000 and 2012. Trends in aerosol composition produced by these changing emissions may be detectable from satellite observations of aerosol scattering and absorption.

Detection of aerosol composition from passive nadir satellite observations is exceedingly difficult; few methods exist. The aerosol-type classification provided by retrievals from the MISR instrument, enabled by multi-angle viewing, is one such source of information about aerosol composition from constraints on particle size, shape, and single scattering albedo (SSA) (Kahn and Gaitley, 2015). MISR retrievals have been used to classify particles relating to events such as biomass burning, desert dust, volcanic eruptions, and pollution events (e.g. Liu et al., 2007; Kalashnikova and Kahn, 2008; Dey and Di Girolamo, 2011; Scollo et al., 2012; Guo et al., 2013). The most commonly used satellite product for aerosol information is aerosol optical depth (AOD), the columnar extinction of radiation by atmospheric aerosols. AOD can be retrieved from satellite measurements of top-of-atmosphere (TOA) radiance in combination with prior knowledge of aerosol optical properties. Several studies have examined trends in satellite AOD. Following trends in emissions, over the past decade positive trends in satellite AOD have been observed over Asia and Africa, corresponding to regions experiencing industrial growth (de Meij et al., 2012; Chin et al., 2014; Mao et al., 2014; Mehta et al., 2016), while negative trends in satellite AOD have been observed over North America and Europe, largely due to pollution controls

(Hsu et al., 2012; de Meij et al., 2012; Chin et al., 2014; Mehta et al., 2016). Studies such as these demonstrate the information about the evolution of aerosol abundance offered by total column AOD retrievals, but measurements of absorption would complement the scattering information in AOD retrievals by providing independent information on aerosol composition.

The Ultraviolet Aerosol Index (UVAI) is a method of detecting aerosol absorption from satellite-measured radiances (Herman et al., 1997; Torres et al., 1998). Because the UVAI is calculated from measured radiances, a priori assumptions about aerosol composition are not required for its calculation, thus yielding independent information on aerosol scattering (Herman et al., 1997; Torres et al., 1998, 2007; de Graaf et al., 2005; Penning de Vries et al., 2009) and absorption. The UVAI has been widely applied to examine mineral dust (Israelevich et al., 2002; Schepanski et al., 2007; Badarinath et al., 2010; Huang et al., 2010) and biomass burning aerosols (Duncan et al., 2003; Guan et al., 2010; Torres et al., 2010; Kaskaoutis et al., 2011; Mielonen et al., 2012) including brown carbon (BrC) (Jethva and Torres, 2011; Hammer et al., 2016). The UVAI is not typically used to examine scattering aerosol, but aerosol scattering causes a net decrease in the overall value of the UVAI, meaning that the UVAI could be used to detect changes due to both aerosol absorption and scattering. Prior interpretation of the UVAI has been complicated by its dependence on geophysical parameters, such as aerosol layer height (Herman et al., 1997; Torres et al., 1998; de Graaf et al., 2005). Examining trends in the UVAI would provide an exciting opportunity to investigate the evolution of aerosol absorption and scattering over time, if the multiple parameters affecting the UVAI could be accounted for through simulation.

In this work, we apply a simulation of the UVAI, which was developed and evaluated regionally and seasonally in Hammer et al. (2016), to interpret trends in recently reprocessed Ozone Monitoring Instrument (OMI) UVAI observations for 2005–2015 to understand global changes in aerosol composition. We interpret observed UVAI values by using a radiative transfer model (VLIDORT) to calculate UVAI values as a function of simulated aerosol composition from the global 3-D chemical transport model GEOS-Chem. By using scene-dependent OMI viewing geometry together with scene-dependent modelled atmospheric composition we enable quantitative comparison of model results with observations. Comparison of trends in observed OMI UVAI values to the trends in simulated UVAI values, which are calculated using known aerosol composition, enables qualification of how changes in aerosol absorption and scattering could influence the observed UVAI trends and identification of model development needs. We conduct our analysis at the global scale to understand trends worldwide. Section 3.3 describes the OMI UVAI observations and our UVAI simulation. Section 3.4 examines the trends in emissions of GEOS-Chem aerosols and their precursors for 2005–2015 to provide context for the trends in

our simulated UVAI. Section 3.5 compares the mean values during 2005–2015 of the OMI UVAI and our simulated UVAI. Section 3.6 compares the 2005–2015 trends in OMI and simulated UVAI values. In Sect. 3.7 we examine the sensitivity of the UVAI to changes in the abundance of individual aerosol species. Trends in our UVAI simulation are interpreted by applying the trends in the GEOS-Chem aerosol species to calculate the associated change in UVAI. Section 3.8 reports the conclusions.

3.3 Methods

3.3.1 OMI Ultraviolet Aerosol Index

The OMI UVAI is a method of detecting absorbing aerosols from satellite measurements in the near-UV wavelength region and is a product of the OMI near-UV algorithm (OMAERUV) (Herman et al., 1997; Torres et al., 1998, 2007). The OMAERUV algorithm uses the 354 and 388 nm radiances measured by OMI to calculate the UVAI as a measure of the deviation from a purely Rayleigh scattering atmosphere bounded by a Lambertian reflecting surface. Positive UVAI values indicate absorbing aerosol while negative values indicate non-absorbing aerosol. Near-zero values occur when clouds and Rayleigh scattering dominate. Negative UVAI values due to aerosol scattering are often weak and have historically been affected by noise in previous datasets (Torres et al., 2007; Penning de Vries et al., 2015). Because UVAI values are calculated from TOA radiance which contains total aerosol effects, the presence (or absence) of scattering aerosol along with absorbing aerosol can either weaken (or strengthen) the absorption signal. Therefore the UVAI could be used to detect changes over time due to both aerosol absorption and scattering.

The main source of error affecting a trend analysis of the UVAI is the OMI row anomaly, which has reduced the sensor viewing capability for specific scan angles since 2008 (http://projects.knmi.nl/omi/research/ product/rowanomaly-background.php, last access: 22 August 2017). The sudden suppression of observations for specific viewing geometries (i.e. the row anomaly) could cause an additional spurious trend in the UVAI trend calculation. We address this concern by considering only scan positions 3–23, which remain unaffected by the row anomaly, and also by using the recently reprocessed OMAERUV UVAI that is less sensitive to scan-angle-dependent cloud artifacts due to the implementation of a Mie-scattering-based water cloud model (Torres et al., 2018). We focus on cloud-filtered observations by excluding scenes with OMI UVAI radiative cloud fraction exceeding 5 % to further reduce uncertainty due to clouds. Furthermore,

we focus on 10 years of observations so that multiple observations can reduce the random error of UVAI observations.

Because the OMI UVAI is calculated directly from OMI- measured radiances, instrument degradation over time could be a significant source of uncertainty (Povey and Grainger, 2015). Schenkeveld et al. (2017) found that the OMI radiances in the channel used for the UVAI have changed by only ~ 1–1.15 % over the entire OMI record. Applying this change to the radiances results in a change in the ab- solute UVAI of ~ 10^{-4} , which is negligible. Schenkeveld et al. (2017) also calculated the trend in the ratio of the 354/380nm radiances measured by OMI for pixels unaffected by the OMI row anomaly and over the tropical Pacific where the presence of aerosol is expected to be minimal, to assess the change in the spectral dependence of OMI's over- all radiance calibration over the course of the mission. They found that the trend in the 354/380 nm radiance ratio over the entire OMI record was < 0.5 % per decade. We estimate the effect of instrument degradation on our trend analysis by calculating the change in UVAI associated with the 0.5 % per decade trend in the 354/380 nm radiance ratio. Applying the trend in 354/380 nm radiance ratio to the UVAI calculation globally resulted in a negligible change in the UVAI of $\sim 2 \times 10^{-4}$ yr^{-1}. To avoid the influence of any possible spurious trends due to instrument degradation on our trend analysis, we subtract the trend in global mean UVAI from the cloud-filtered UVAI prior to interpretation.

We perform trend analysis on monthly mean time series data for the years 2005–2015 using generalized least squares (GLS) regression, as described by Boys et al. (2014). Prior to regression, the data are aggregated to monthly mean values, and the monthly time series data are deseasonalized by subtracting the monthly mean for the period 2005–2015 to focus on the long-term trend. Deseasonalization is a recommended method to accurately calculate a long-term trend in a seasonally varying time series (Weatherhead et al., 1998, 2002; Wilks, 2011) and is widely employed for the trend analysis of geophysical data including temperature, chemical species concentrations, relative humidity, cloud cover, and aerosol parameters (Reynolds and Reynolds, 1988; Prinn et al., 1992; Pelletier and Turcotte, 1997; Zhang et al., 1997; Dai, 2006; Norris and Wild, 2007; Boys et al., 2014; Ma et al., 2016). Each pixel is required to have data for at least 60 % of the time period before regression is performed. In the following section, we discuss our UVAI simulation and the implementation of the new UVAI algorithm in the simulation.

3.3.2 Simulated UVAI

We simulate the UVAI using the VLIDORT radiative transfer model (Spurr, 2006), following Buchard et al. (2015) and Hammer et al. (2016). We calculate the TOA radiances at 354 and 388 nm needed for the UVAI calculation by supplying VLIDORT with the OMI viewing geometry for each scene, as well as the GEOS-Chem simulation of vertical profiles of aerosol extinction, spectrally dependent single scattering albedo, and the corresponding spectrally dependent scattering phase function. Thus these parameters account for the sensitivity of the UVAI to aerosol layer height and spectrally dependent aerosol optical properties.

We introduce to the UVAI simulation a Mie-scattering-based water cloud model (Deirmendjian, 1964) for consistency with the reprocessed OMI UVAI dataset. Following Torres et al. (2018), we compute the radiances used in the UVAI calculation as a combination of clear and cloudy sky conditions. We use the same cloud fractions and cloud optical depths used in the OMI UVAI algorithm for coincident OMI pixels. We avoid cloudy scenes by considering only pixels with OMI radiative cloud fraction of less than 5 %. For the UVAI calculation we use the surface reflectance fields provided by OMI. We calculated the 2005–2015 trends in these surface reflectance fields and found that they were statistically insignificant globally and on the order of 10^{-5} yr^{-1}. We calculated the change in UVAI due to a change in surface reflectance of this order of magnitude and found that the change in UVAI was negligible. We also calculated the change in UVAI due to changes in simulated aerosol altitude, but found that the trends in aerosol altitude were negligible (order 10^{-5} hPa yr^{-1}). Therefore we focus our analysis on trends in aerosol composition which have a larger effect on the UVAI as demonstrated below.

We use the GEOS-Chem model v11-01 (http://geos-chem. org, last access: 22 August 2017) as input to the UVAI simulation and to calculate the sensitivity of the UVAI simulation to aerosol composition. The simulation is driven by assimilated meteorological data from MERRA-2 Reanalysis of the NASA Global Modeling and Assimilation Office (GMAO). Our simulation is conducted at a spatial resolution of $2^{\circ} \times 2.5^{\circ}$ with 47 vertical levels for the years 2005–2015. We supply VLIDORT with GEOS-Chem aerosol fields coincident with OMI observations.

GEOS-Chem contains a detailed oxidant-aerosol chemical mechanism (Bey et al., 2001; Park et al., 2004). The aerosol simulation includes the sulfate–nitrate–ammonium system (Park et al., 2004; Fountoukis and Nenes, 2007; Pye et al., 2009), primary carbonaceous aerosol (Park et

al., 2003) mineral dust (Duncan Fairlie et al., 2007), and sea salt (Jaeglé et al., 2011). Semivolatile primary organic carbon and secondary organic aerosol (SOA) formation is described in Pye et al. (2010). We update the original semi-volatile partitioning of SOA formed from isoprene with the irreversible up-take scheme in Marais et al. (2016). HNO_3 concentrations are reduced following Heald et al. (2012). Aerosol optical properties are based on the Global Aerosol Data Set (GADS) (Koepke et al., 1997) as originally implemented by Martin et al. (2003) with updates for organics and secondary in- organics from aircraft observations (Drury et al., 2010), for mineral dust (Lee et al., 2009; Ridley et al., 2012), and for absorbing BrC (Hammer et al., 2016). Here we update the mineral dust optics at ultraviolet wavelengths using a refractive index that minimizes the difference between the mean simulated and OMI UVAI values to allow focus on trends. Aerosols are treated as externally mixed.

Anthropogenic emissions are from the EDGARv4.3.1 global inventory (Crippa et al., 2016) with emissions over- written in areas with regional inventories for the United States (NEI11; Travis et al., 2016), Canada (CAC), Mexico (BRAVO; Kuhns et al., 2005), Europe (EMEP; http: //www.emep.int/, last access: 22 August 2017), China (MEIC v1.2; M. Li et al., 2017), and elsewhere in Asia (MIX; C. Li et al., 2017). Emissions from open fires for individual years from the GFED4 inventory (Giglio et al., 2013) are included. The long-term concentrations from this simulation have been extensively evaluated versus ground-based $PM_{2.5}$ composition measurements where available and versus satellite- derived $PM_{2.5}$ trends (Li et al., 2017).

The Supplement evaluates trends in simulated SO_2, NO_2, and AOD versus satellite retrievals from multiple instruments and algorithms. We find broad consistency between our simulated NO_2 and SO_2 column trends with those from OMI (Supplement Figs. 3-S1 and 3-S2). Our simulated AOD trends are generally consistent with the trends in satellite AOD retrievals, with the exception of positive trends in AOD over western North America and near the Aral Sea in most retrieval products and a negative trend in AOD over Mongolia/Inner Mongolia in all retrieval products (Fig. 3-S3).

We filter our GEOS-Chem aerosol simulated fields based on the coincident OMI pixels, which are regridded to the model resolution of $2^{\circ} \times 2.5^{\circ}$. This allows for the direct comparison between our GEOS-Chem simulation and the OMI UVAI observations.

3.4 Trend in emissions of GEOS-Chem aerosols and their precursors

Figure 3-1 shows the trends in emissions of aerosols and their precursors from our GEOS-Chem simulation calculated from the GLS regression of monthly time series values for 2005–2015. Cool colours indicate negative trend values, warm colours indicate positive trend values, and the opacity of the colours indicates the statistical significance of the trends. The trends in emissions of sulfur dioxide (SO_2) and nitrogen oxides (NO_x) follow similar patterns (Fig. 3-1a and b, respectively). Negative trends (−1 to −0.01 kg km^{-2} yr^{-1}) are present over North America and Europe, corresponding to pollution controls (Leibensperger et al., 2012; Klimont et al., 2013;

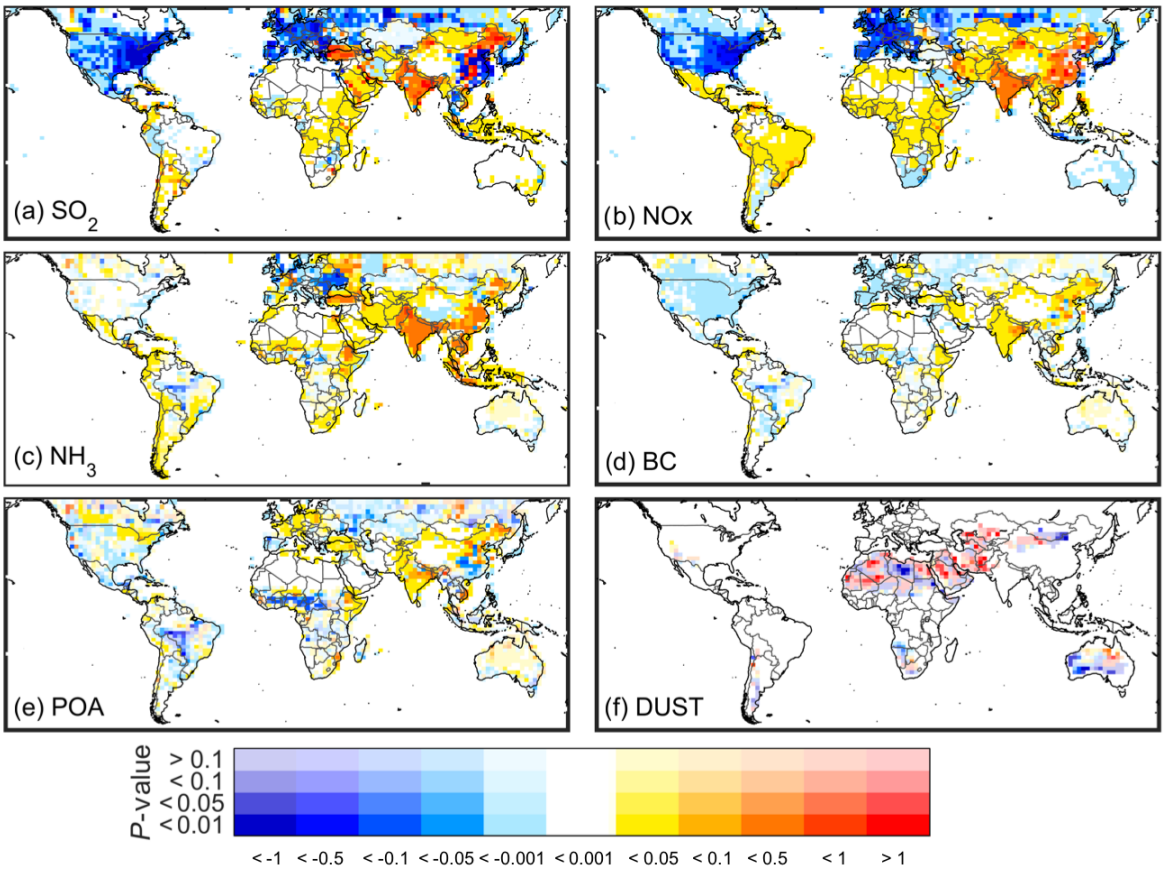

Figure 3-1: Trend in emissions of (a) sulfur dioxide (SO_2) (kg SO_2 km^{-2}yr^{-1}), (b) nitrogen oxides (NO_x) (kg NO km^{-2}yr^{-1}), ammonia (NH_3) (kg NH_3 km^{-2} yr^{-1}), black carbon (BC) (kg C km^{-2} yr^{-1}), primary organic carbon (POA) (kg C km^{-2} yr^{-1}), and dust (kg km^{-2} yr^{-1}) used in our GEOS-Chem simulation. The trends are calculated from the generalized least squares regression of monthly time series values during 2005–2015.

Curier et al., 2014; Simon et al., 2015; Xing et al., 2015; C. Li et al., 2017). Positive trends (0.5 to 1 kg km^{-2} yr^{-1}) in both species are present over India and eastern China, but the positive trends in

emissions of SO_2 over eastern China are interspersed with negative trends (−1 to −0.5 kg km^{-2} yr^{-1}) in SO_2 emissions, corresponding to the deployment of desulfurization equipment in power plants in recent years (Lu et al., 2011; Klimont et al., 2013; Wang et al., 2015). Ammonia (NH_3) emissions (Fig. 3-1c) have positive trends (0.001 to 0.05 kg km^{-2} yr^{-1}) over most of South America, North Africa, the Middle East, and most of Asia with larger trends (0.1 to 0.5 kg km^{-2} yr^{-1}) over India and eastern China. There are positive trends (0.001 to 0.05 kg km^{-2} yr^{-1}) in BC emissions (Fig. 3-1d) over North Africa, Europe, the Middle East, India, and China and negative trends (−0.05 to −0.001 kg km^{-2} yr^{-1}) over North America, Europe, West Africa, and central South America. The trends in primary organic aerosol (POA) emissions (Fig. 3-1e) follow a similar pattern as the trends in BC emissions, except there are negative trends (−0.1 to −0.05 kg km^{-2} yr^{-1}) over eastern China and the negative trends (−1 to −0.1 kg km^{-2} yr^{-1}) over West Africa and central South America are larger in magnitude reflecting regional changes in fire activity (Chen et al., 2013; Andela and van der Werf, 2014). There are also positive trends (0.001 to 0.05 kg km^{-2} yr^{-1}) over the northern United States and Canada. The trends in dust emissions (Fig. 3-1f) show the largest magnitude of all the various species, although many have low statistical significance, with areas of positive and negative trends (> 1 and < −1 kg km^{-2} yr^{-1}) over North Africa, positive trends (> 1 kg km^{-2} yr^{-1}) parts of the Middle East, and negative trends (< −1 kg km^{-2} yr^{-1}) over northern China and southern Australia.

3.5 Mean UVAI values for 2005–2015

We examine the seasonal long-term mean UVAI values for insight into the spatial distribution of the aerosol absorption signals. Figures 3-2 and 3-3 show the seasonal mean UVAI values for 2005–2015 for OMI and the simulation, respectively. Positive UVAI values between 0.2 and 1.5 indicating aerosol absorption are present over major desert regions globally for both OMI and the simulation, particularly over the Saharan, Iranian, and Thar deserts. These positive signals are driven by the absorption by mineral dust (Herman et al., 1997; Torres et al., 1998; Buchard et al., 2015). The simulation underestimates some of the smaller dust features captured by OMI, such as over western North America, South America, Australia, and parts of Asia, perhaps reflecting an underestimation in the simulated mineral dust lifetime (Ridley et al., 2012) and missing dust sources (Ginoux et al., 2012; Huang et al., 2015; Guan et al., 2016; Philip et al., 2017). The seasonal variation in the observed and simulated UVAI is similar albeit with larger simulated values in spring (MAM) over North Africa. In all seasons, the UVAI values driven by

absorption by dust in the simulation are concentrated mostly over North Africa, while for OMI the UVAI values are more homogeneous over the Middle East and Asia as well. Positive UVAI values of ~ 0.2–1 over West and Central Africa appearing in both the OMI and simulated values correspond to absorption by BrC from biomass burning activities in these regions (Jethva and Torres, 2011; Hammer et al., 2016). Over ocean most data are removed by our strict cloud filter.

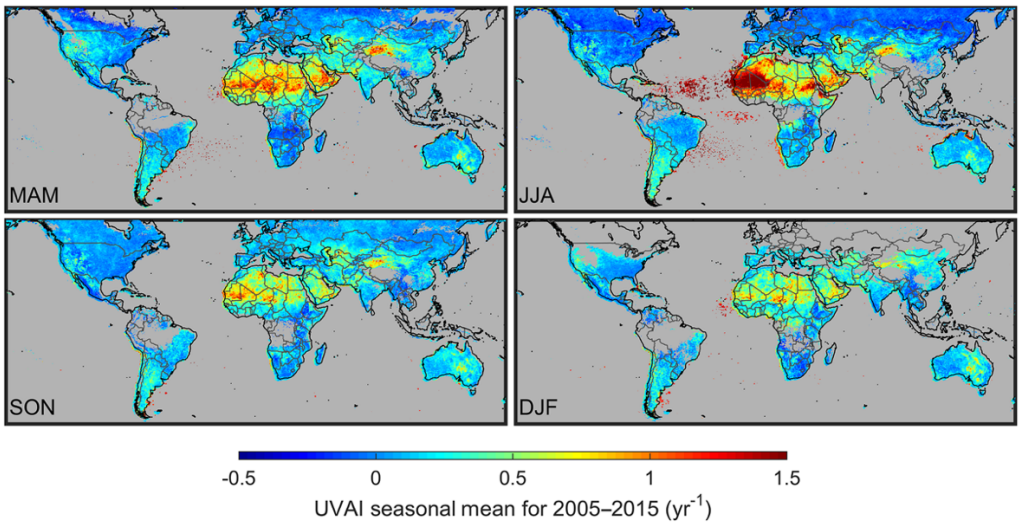

Figure 3-2: Seasonal mean UVAI values for the 2005–2015 period as observed by OMI for MAM (May, April, March), JJA (June, July August), SON (September, October, November), and DJF (December, January, February). Grey indicates persistent cloud fraction greater than 5 %.

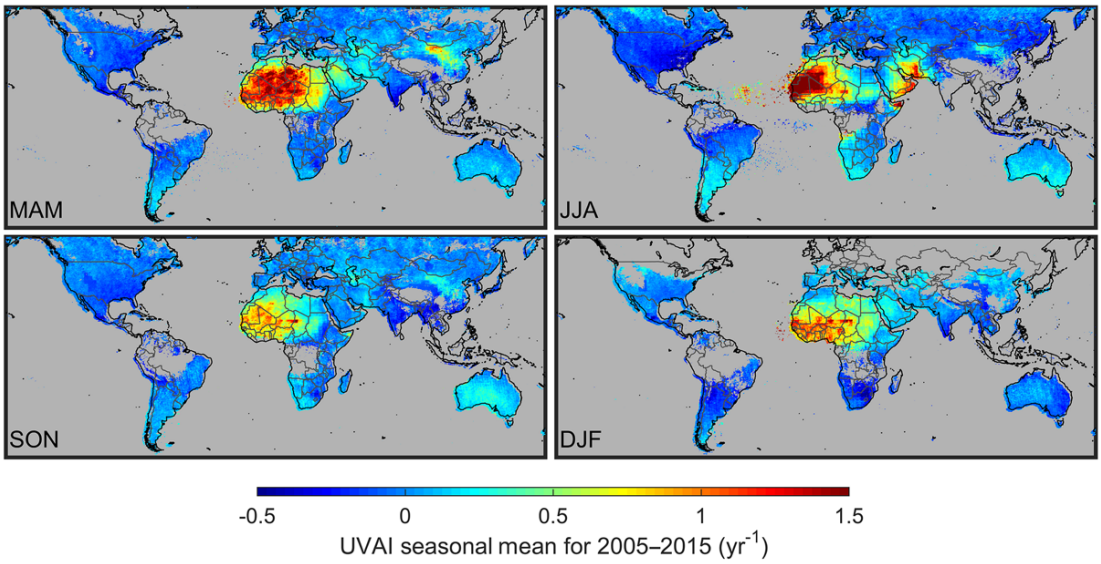

Figure 3-3: Seasonal mean UVAI values for the 2005–2015 period from our simulation coincidently sampled from OMI for MAM (May, April, March), JJA (June, July August), SON (September, October, November), and DJF (December, January, February). Grey indicates persistent cloud fraction greater than 5 %.

3.6 Trend in UVAI values between 2005 and 2015

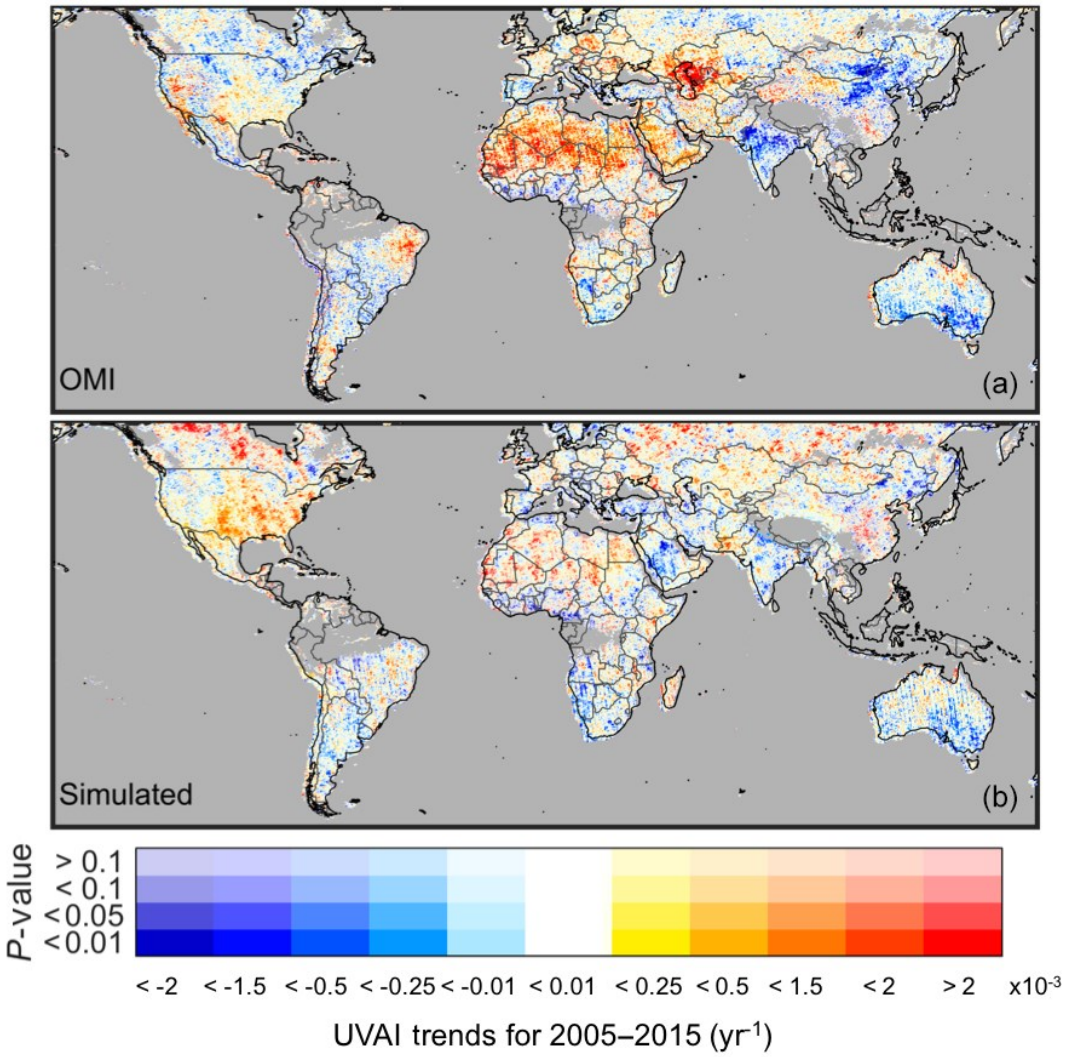

Figure 3-4: Trends in OMI (a) and simulated (b) UVAI values coincidently sampled from OMI calculated from the generalized least squares regression of monthly time series values during 2005–2015. The opacity of the colours indicates the statistical significance of the trend. Grey indicates persistent cloud fraction greater than 5 %.

Figure 3-4 shows the trend in OMI and simulated UVAI values (coincidently sampled from OMI) calculated from the GLS regression of monthly UVAI time series values during 2005–2015. Several regions exhibit consistency between the OMI and simulated UVAI trends. There are statistically significant positive trends in both OMI and simulated UVAI values over the eastern United States (OMI: 1.0×10^{-5} to 2.5×10^{-4} yr^{-1}; simulated: 2.5×10^{-4} to 5.0×10^{-4} yr^{-1}) and Canada and parts of Russia (OMI: 1.0×10^{-5} to 2.5×10^{-4} yr^{-1}; simulated: 5.0×10^{-4} to 2.0×10^{-3} yr^{-1}).

Positive UVAI trends (1.0×10^{-5} to 2.5×10^{-4} yr^{-1}) in both OMI and simulated values are present over Europe, although the simulated trends have low statistical significance. Statistically significant positive UVAI trends (5.0×10^{-4} to 2.0×10^{-3} yr^{-1}) in OMI values are apparent over North Africa, which generally are captured by the simulation but with low statistical significance. Negative UVAI trends (-1.5×10^{-3} to -1.0×10^{-5} yr^{-1}) in both OMI and simulated values are apparent over most of South America, southern Africa, and Australia. Negative UVAI trends (-2×10^{-3} to -5.0×10^{-4} yr^{-1}) in both OMI and simulated values are present over West Africa, with low statistical significance that could be related to the filtering of persistent clouds. OMI and simulated UVAI values show negative trends (-2×10^{-3} to -5×10^{-4} yr^{-1}) over India, although the simulated trends have lower statistical significance.

Some regions have trends in OMI UVAI values which are not captured by the simulation. Statistically significant positive UVAI trends (2.5×10^{-4} to 1.5×10^{-3} yr^{-1}) over the western United States are apparent in the OMI values but not in the simulation. Zhang et al. (2017) found positive trends in aerosol absorption optical depth from OMI retrievals that they attributed to positive trends in mineral dust over the region, which were not captured by their GEOS-Chem simulation. Statistically significant positive UVAI trends (5.0×10^{-4} to 2.0×10^{-3} yr^{-1}) in OMI values exist over the Middle East, while the simulation has negative trends with low statistical significance. The OMI UVAI reveals a region of statistically significant negative trends (-2×10^{-3} to -5.0×10^{-4} yr^{-1}) over Mongolia/Inner Mongolia which is not captured by the simulation. There is also a small area of statistically significant positive UVAI trends (1.5×10^{-3} to 2.0×10^{-3} yr^{-1}) in OMI values of over Central Asia between the Caspian Sea and the Aral Sea which is not captured by the simulation. Trends in surface reflectance from the diminishing Aral Sea cannot solely explain the UVAI trends since they extend over the Caspian Sea. Trends in mineral dust are a more likely explanation as discussed further below.

Figures 3-5 and 3-6 show the seasonality of the OMI and simulated UVAI trends respectively. The positive UVAI trends over the eastern United States are strongest in summer (JJA) for both OMI and the simulation. The positive UVAI trends over North Africa and the Middle East are present for all seasons for OMI and for most seasons in the simulation, except in JJA for North Africa and spring (MAM) for the Middle East. The simulation underestimates the observed UVAI trend over North Africa in SON, perhaps related to an under- estimation in trends in mineral dust emissions in the simulation during this season. He et al. (2014) examined the 2000–

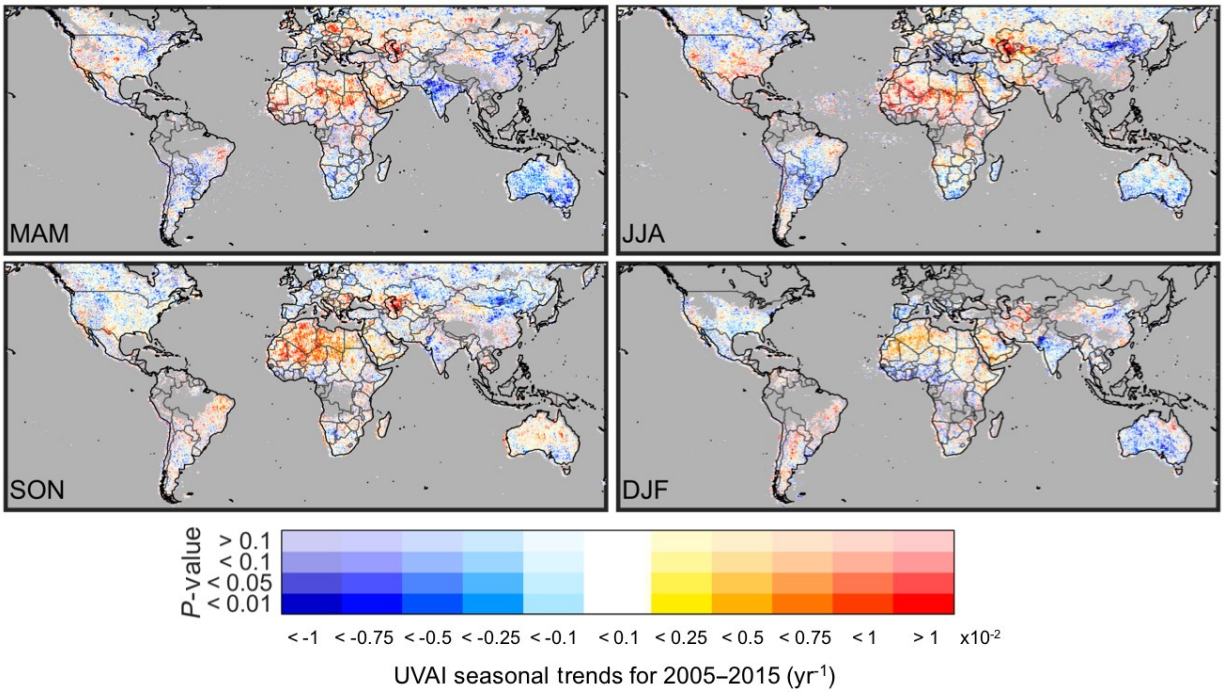

Figure 3-5: Seasonality of the trends in OMI UVAI values calculated from the generalized least squares regression of monthly time series values during 2005–2015 for MAM (May, April, March), JJA (June, July August), SON (September, October, November), and DJF (December, January, February). The opacity of the colours indicates the statistical significance of the trend. Grey indicates persistent cloud fraction greater than 5 %.

2010 trends in global surface albedo using the Global Land Surface Satellites (GLASS) dataset and found no significant trends over this region during SON. The negative trend in UVAI values over West Africa is most apparent in the fall (SON) and winter (DJF) for both OMI and the simulation. The negative OMI UVAI trends over Mongolia/Inner Mongolia and the positive OMI UVAI trends near the Aral Sea are strongest in JJA and weakest in DJF, providing evidence of a mineral dust source. The OMI UVAI trend over Mongolia/Inner Mongolia may be part of a longer-term trend. Guan et al. (2017) examined dust storm data over northern China (including Inner Mongolia) for the period 1960–2007 and found that dust storm frequency has been declining over the region due to a gradual decrease in wind speed. The current generation of chemical transport models is unlikely to represent the source near the Aral Sea without an explicit parameterization of the drying sea. The desiccation of the Aral Sea over recent decades has resulted in a steady decline in water coverage over the area (Shi et al., 2014; Shi and Wang, 2015) and has led to the dried up sea bed becoming an increasing source of dust activity in the region (Spivak et al., 2012). Indoitu et al. (2015) found that most dust events are directed towards the west, consistent with the

OMI observations. An increase in surface reflectance due to the drying up of the sea bed could also positively influence trends in UVAI. He et al. (2014) found a positive trend over 2000–2010 in surface albedo over the region in JJA and SON, corresponding to when the OMI UVAI trends are strongest.

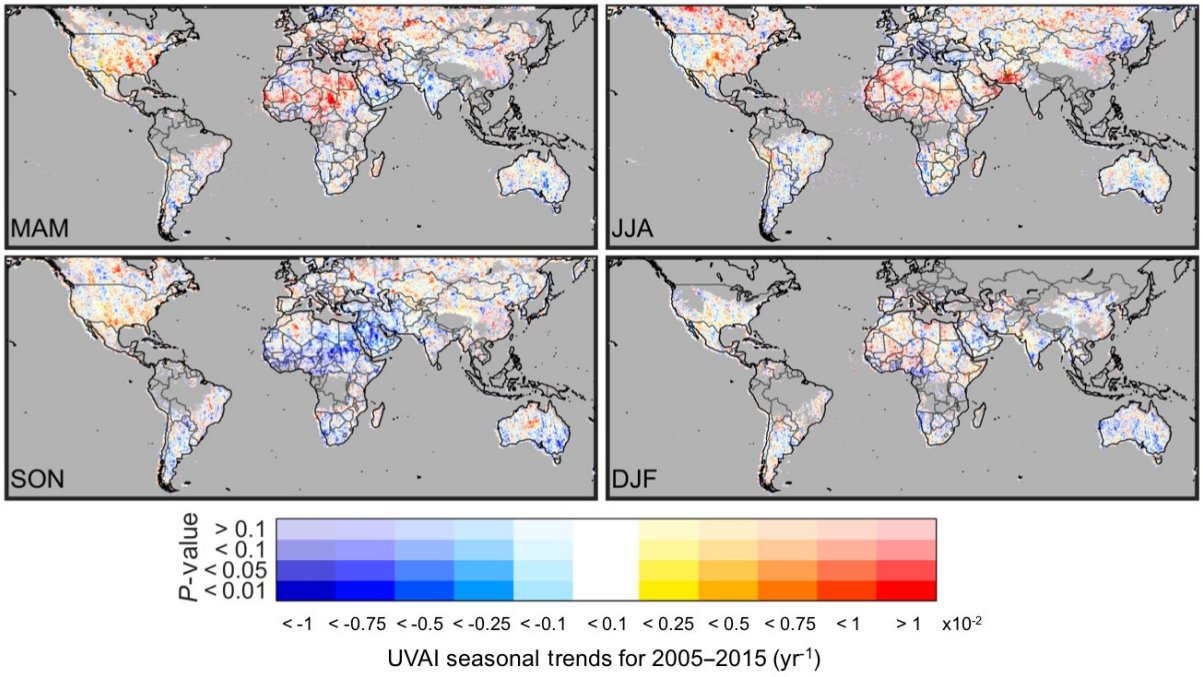

Figure 3-6: Seasonality of the trends in simulated UVAI values coincidently sampled from OMI calculated from the generalized least squares regression of monthly time series values during 2005–2015 for MAM (May, April, March), JJA (June, July August), SON (September, October, November), and DJF (December, January, February). The opacity of the colours indicates the statistical significance of the trend. Grey indicates persistent cloud fraction greater than 5 %.

3.7 Contribution of individual aerosol species to the simulated UVAI

To further interpret the UVAI trends, we examine the trends in aerosol concentrations from our GEOS-Chem simulation (Fig. 3-7). Figure 3-7a shows the trends in secondary inorganic aerosol (SIA). There are statistically significant negative trends over the eastern United States (−1 to −0.05 μg m^{-2} yr^{-1}) and statistically significant positive trends over the Middle East (0.05 to 0.5 μg m^{-2} yr^{-1}), India (0.05 to 1 μg m^{-2} yr^{-1}), South America, and southern Africa (0.05 to 0.25 μg m^{-2} yr^{-1}). Figure 3-7b shows the trends in dust. Similar to the trends in emissions, the trends in dust concentrations are of the largest magnitude of the various species, but often with low statistical significance. There are positive trends over the Middle East (> 2 μg m^{-2} yr^{-1}), India (0.05 to 2 μg m^{-2} yr^{-1}), and northwest China (1 to 2 μg m^{-2} yr^{-1}). There are also positive trends (0.05 to 0.25 μg m^{-2} yr^{-1}) with low statistical significance over the United States, northern South America, southern

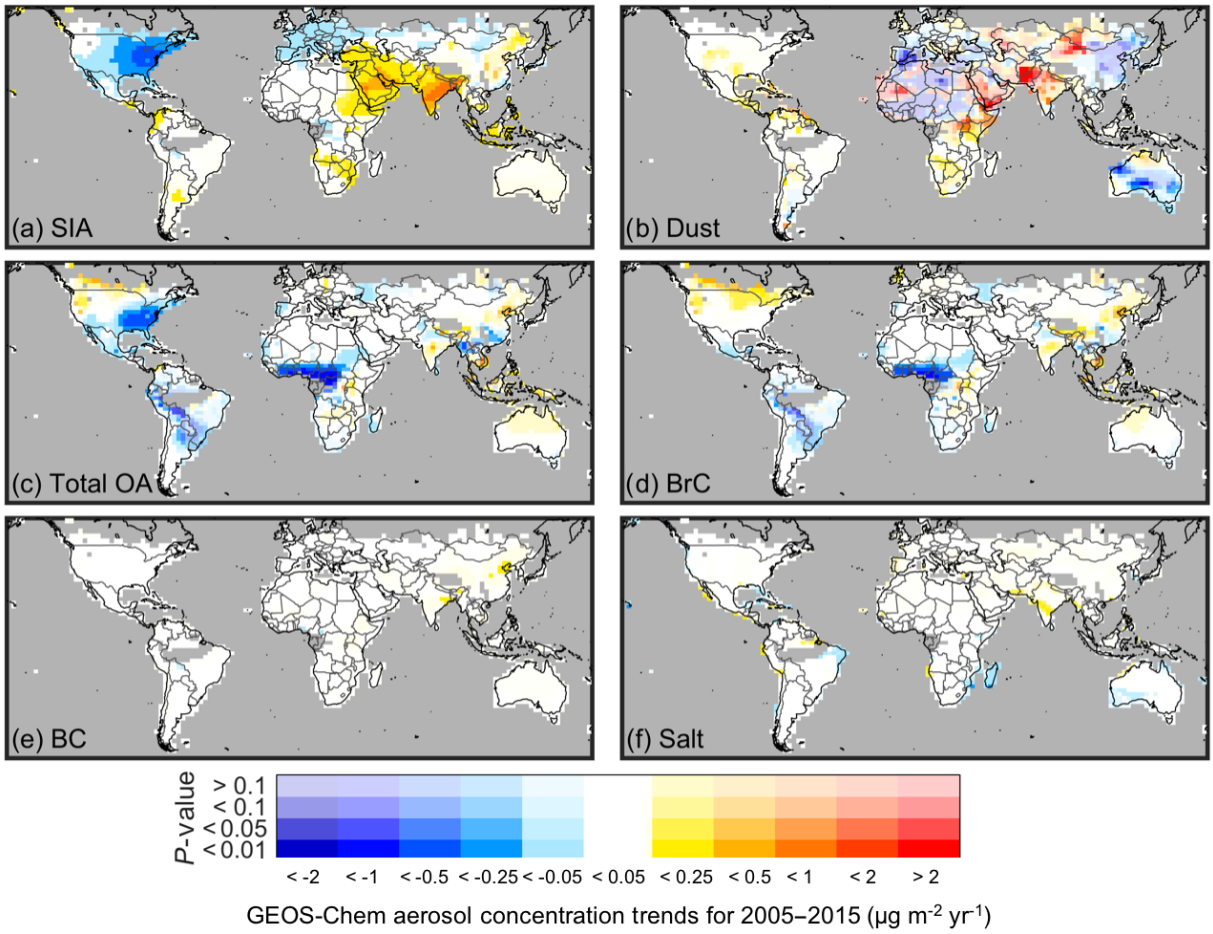

Figure 3-7: Trend in GEOS-Chem aerosol concentrations for (a) secondary inorganic aerosol (SIA), (b) dust, (c) total organic aerosol (OA), (d) brown carbon (BrC), (e) black carbon (BC), and (f) sea salt. The trends are calculated from the GLS regression of monthly aerosol concentration time series values during 2005–2015. The opacity of the colours indicates the statistical significance of the trend. Grey indicates persistent cloud fraction greater than 5 %.

Africa, and northern Australia. There is a combination of positive and negative trends (> 2 and < −2 μg m^{-2} yr^{-1}) over North Africa, and negative trends over China and Mongolia (< −2 μg m^{-2} yr^{-1}) and Australia (−1 to −0.5 μg m^{-2} yr^{-1}). Figure 3-7c and d show the trends in total organic aerosol (OA) and the absorbing BrC component of OA, respectively. Positive trends over Canada and parts of Russia (0.05 to 0.5 μg m^{-2} yr^{-1}) in total OA are mainly due to the positive trend in BrC. Statistically significant negative trends in total OA (−1 to −0.05 μg m^{-2} yr^{-1}) over the eastern United States are dominated by scattering organic aerosol. Statistically significant negative trends (−2 to −0.05 μg m^{-2} yr^{-1}) over West Africa and South America for total OA are dominated by the trend in absorbing BrC. Figure 3-5e and f show the trends in BC and salt, respectively. There are

positive trends (0.05 to 0.25 μg m^{-2} yr^{-1}) in BC with low statistical significance over India and China. Sea salt trends are negligible.

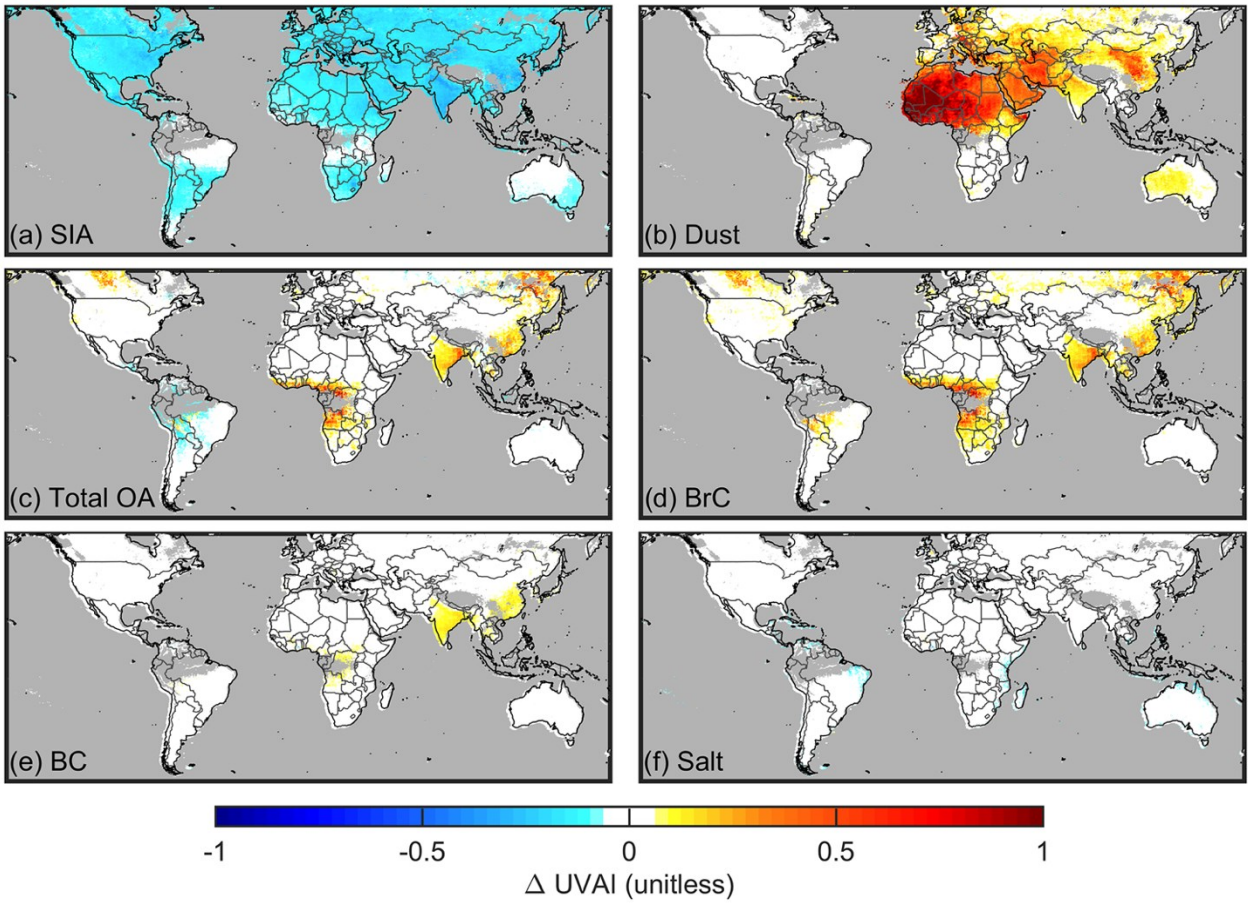

Figure 3-8: Annual mean change in simulated UVAI values for 2008 due to the doubling of concentrations of (a) secondary inorganic aerosol (SIA), (b) dust, (c) total organic aerosol (OA), (d) brown carbon (BrC), (e) black carbon (BC), and (f) sea salt from the GEOS- Chem simulation. Grey indicates persistent cloud fraction greater than 5 %.

To gain further insight into how changes in aerosols effect the trends in simulated UVAI, we examine the sensitivity of the UVAI to changes in individual aerosol species. Figure 3-8 shows the change in annual mean UVAI due to doubling the concentration of individual aerosol species. This information facilitates interpretation of the observed UVAI trends by identifying the chemical components that could explain the observed trends. Doubling scattering SIA concentrations (Fig. 3-8a) decreases the UVAI between −0.25 and −0.1 over most of the globe, with the largest changes over the eastern United States, Europe, parts of the Middle East, India, and southeast China. Doubling dust concentrations (Fig. 3-8b) produces the largest changes in UVAI, causing increases between 0.5 and 1 over North Africa and smaller increases between 0.2 and 0.5 over the

Middle East, Europe, and parts of Asia and Australia. Figure 3-8c and d show the changes in UVAI due to doubling total OA concentrations and the absorbing BrC component, respectively. The doubling of BrC increases the UVAI between 0.1 and 0.5 over Canada, West and Central Africa, India, parts of Russia, eastern China, and central South America. Doubling total OA concentrations over central South America causes a net decrease of ~ -0.1 as the scattering component of total OA cancels out the absorption by BrC. Doubling BC concentrations (Fig. 3-8e) increases the UVAI of 0.1 over Central Africa, India, and southeast China, while doubling sea salt concentrations (Fig. 3-8f) has negligible effect on the UVAI.

Figure 3-9 shows the change in simulated UVAI due to the 2005–2015 trends in individual aerosol species from our GEOS-Chem simulation. The change for each species is calculated by applying the aerosol concentration trends for the individual aerosol type while leaving the concentrations unchanged for the other aerosol species, then taking the difference between this perturbed UVAI simulation and an unperturbed simulation. Negative trends in scattering SIA (Fig. 3-9a) increase the UVAI by 1.0×10^{-4} to 7.5×10^{-3} yr^{-1} over the eastern United States and by 1.0×10^{-4} to 2.5×10^{-3} yr^{-1} over Europe, corresponding to regions of positive UVAI trends in both OMI and the simulation (Fig. 3-4). Increasing SIA decreases the UVAI by -2.5×10^{-3} to -1.0×10^{-4} yr^{-1} over the Middle East, India, and east China. Trends in dust concentrations (Fig. 3-9b) cause the largest change in UVAI with regional increases $> 1\times10^{-2}$ yr^{-1} and regional decreases $< -1\times10^{-2}$ yr^{-1}. Simulated UVAI trends due to mineral dust are mostly negative over North Africa, East Asia, and Australia, while mostly positive over the Middle East. Noisy trends in regional meteorology cause heterogeneous trends in dust and in the UVAI, with low statistical significance. Figure 3-9c and d show the change in UVAI due to the trends in total OA and the absorbing BrC component of total OA, respectively. Most of the changes in UVAI due to the trends in total OA are caused by the trends in the absorbing BrC component, with increases in the UVAI between 2.5×10^{-3} and 1×10^{-2} yr^{-1} over Canada and parts of Russia, corresponding to regions of positive UVAI trends for both OMI and the simulation (Fig. 3-4). There are decreases in the UVAI $< -1\times10^{-2}$ yr^{-1} over central South America and West Africa due to the negative trends in BrC, corresponding to regions of negative UVAI trends for both OMI and the simulation (Fig. 3-4). Over the eastern United States there is a mixture of increases and decreases in the UVAI due to the trends in scattering organic aerosol. Positive trends in BC increase the UVAI (Fig. 3-9e) by 1.0×10^{-4} to 2.5×10^{-3} yr^{-1}

over India and China. There are no obvious changes in the UVAI due to the trends in sea salt (Fig. 3-9f).

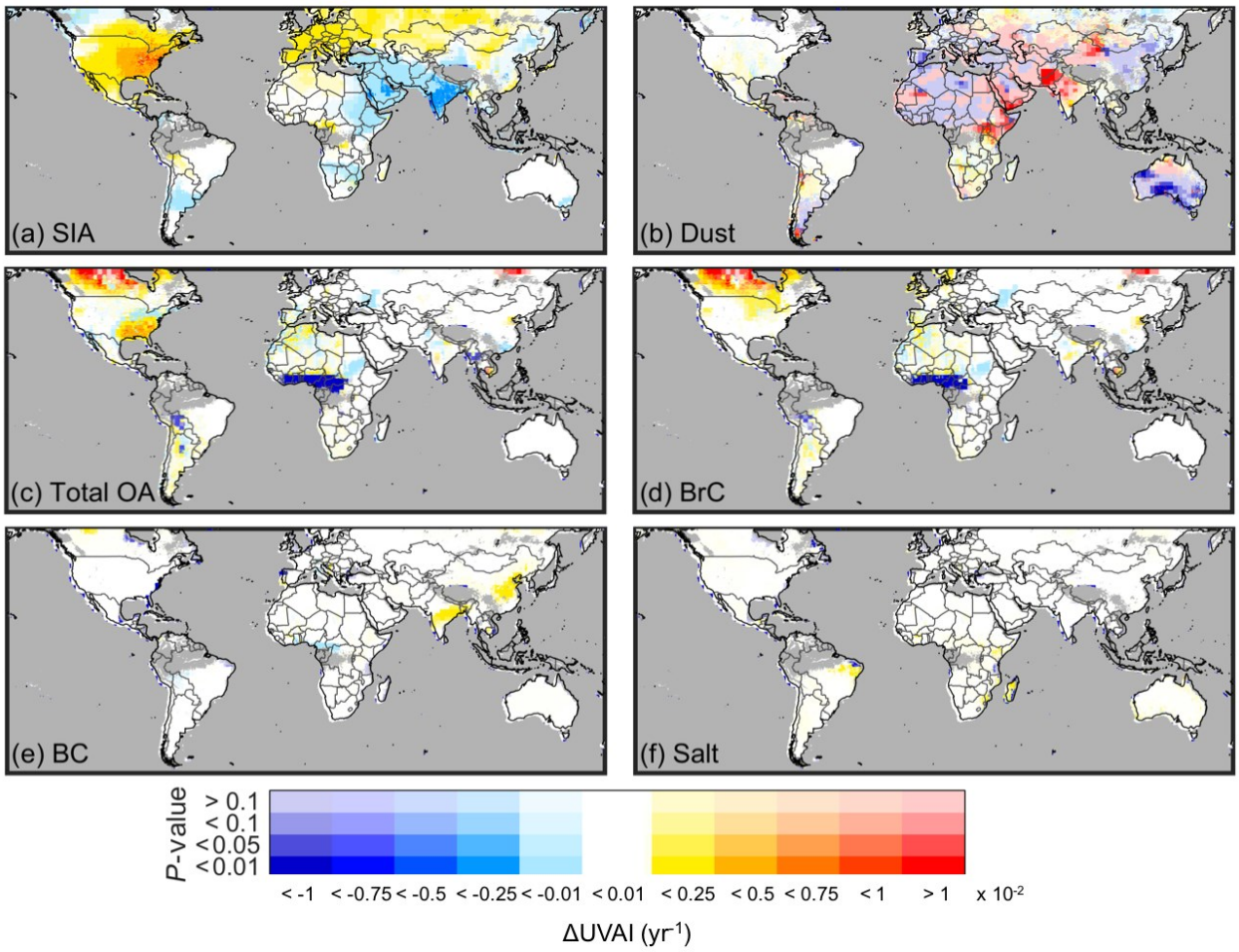

Figure 3-9: Change in simulated UVAI values due to the 2005–2015 trends in (a) secondary inorganic aerosols (SIA), (b) dust, (c) total organic aerosol (OA), (d) brown carbon (BrC), (e) black carbon (BC), and (f) sea salt from the GEOS-Chem simulation. Grey indicates persistent cloud fraction greater than 5 %.

3.8 Conclusions

Observations of aerosol scattering and absorption offer valuable information about aerosol composition. We simulated the UVAI, a method of detecting aerosol absorption using satellite measurements, to interpret trends in OMI observed UVAI during 2005–2015 to understand global trends in aerosol composition. We conducted our simulation using the vector radiative transfer model VLIDORT with aerosol fields from the global chemical transport model GEOS-Chem.

We demonstrated that interpretation of the OMI UVAI with a quantitative simulation of the UVAI offers information about trends in aerosol composition. We found that global trends in the UVAI were largely explained by trends in absorption by mineral dust, absorption by BrC, and scattering by secondary inorganic aerosols. We also identified areas for model development, such as dust emissions from the desiccating Aral Sea.

We examined the 2005–2015 trends in individual aerosol species from GEOS-Chem and applied these trends to the UVAI simulation to calculate the change in simulated UVAI due to the trends in individual aerosol species. The two most prominent positive trends in the observed UVAI were over North Africa and over Central Asia near the desiccating Aral Sea. The simulated UVAI attributes the positive trends over North Africa to increasing mineral dust despite an underestimated simulated trend in fall (SON) that deserves further attention. The positive trends in the observed UVAI over Central Asia near the shrinking Aral Sea are likely due to increased dust emissions, a feature that is unlikely to be represented in most chemical transport models. The most prominent negative trends in the observed UVAI were over East Asia, South Asia, and Australia. The simulation attributed the negative trends over East Asia and Australia to decreasing mineral dust, despite underestimating the trend in East Asia. The simulation attributed the negative trend over South Asia to increasing scattering secondary inorganic aerosols, a trend that the observations imply could be even larger. We found the positive trends in the UVAI over the eastern United States that were strongest in summer (JJA) in both the observations and the simulation were driven by negative trends in scattering secondary inorganic aerosol and organic aerosol. Observed negative trends in winter (DJF) were less well simulated. Over West Africa and South America, negative trends in UVAI were explained by negative trends in absorbing BrC. Thus, trends in the observed UVAI offer valuable information on the evolution of global aerosol composition that can be understood through quantitative simulation of the UVAI.

Looking forward, the availability of the UVAI observations from 1979 to the present offers a unique opportunity to understand long-term trends in aerosol composition. The recent launch of the TROPOspheric Monitoring Instrument (TROPOMI; Veefkind et al., 2012) and the forthcoming geo- stationary constellation offer UVAI observations at finer spatial and temporal resolution. The forthcoming Multi-Angle Imager for Aerosols (MAIA; Diner et al., 2018) satellite instrument offers an exciting opportunity to derive even more information about aerosol

composition by combining measurements at ultraviolet wavelengths with multi-angle observations and polarization sensitivity.

3.9 Acknowledgements

This work was supported by the Natural Science and Engineering Research Council of Canada and the Killam Trusts. Computational facilities were provided in part by the Atlantic Computational Excellence Network and the Graham consortiums of Compute Canada.

3.10 Supplement

3.10.1. Comparison of simulated and OMI SO2 and NO2 columns

We calculate the trends in simulated and OMI SO_2 and NO_2 columns (Figures 3-S1 and 3-S2) to evaluate our GEOS-Chem simulation. There is broad consistency between the trends in our simulated SO_2 and NO_2 columns with those from OMI. There are negative trends in both OMI and simulated SO_2 columns over most of North America, Europe, northern South America, central Africa, and east China. There is a mixture of negative and positive trends in SO_2 over North Africa. There are positive trends in SO_2 over southern South America, southern Africa, the Middle-East, India, most of China, and Australia. The trends in NO_2 columns correspond to the trends in SO_2 columns in almost all regions except for eastern China, which shows positive trends in NO_2 columns for both the simulation and OMI.

3.10.2. Comparison of simulated and satellite AOD

Figure 3-S3 shows the trends in GEOS-Chem and satellite AOD for 2005-2015 filtered based on coincident OMI pixels with persistent cloud fraction greater than 5%. Overall the trends in simulated AOD are consistent with the range of trends in satellite AOD. The GEOS-Chem AOD (Figure 3-S3a) shows negative trends in AOD over the eastern United States and West Africa, and positive trends over the western United States, the Middle-East, India, and most of China. Figure 3-S3b shows the trends in AOD from MISR. Significant negative trends are apparent over the eastern United States, Europe, central South America, parts of North Africa, West Africa, and Mongolia/Inner Mongolia. There are small positive trends over west and central United States, parts of South America, parts of North Africa, southern Africa, parts of the Middle-East, parts of China, and Australia, with stronger positive trends over India. AOD from MODIS Dark Target (Figure 3-S3c) shows negative trends over eastern United States, Europe, and central South America, with small positive trends over southern Africa, most of Asia, and Australia, and stronger positive trends over Canada, southern South America, India, and over Central Asia between the Caspian Sea and the Aral Sea. Figure S3d shows the trends in AOD from MODIS Deep Blue. There small negative trends over eastern United States, central South America, Europe, parts of North Africa and West Africa, with stronger negative trends over the Indo-Gangetic Plain and Mongolia/Inner Mongolia. There are positive trends over southern Africa, most of Asia, and Australia, and stronger positive trends over Canada, southern South America, parts of the Middle-

East, India, and over Central Asia between the Caspian Sea and the Aral Sea. Figures 3-S3e and 3-S3f show the trends in AOD from the OMI OMAERUV algorithm at 388 nm and 500 nm, respectively. Significant negative trends are apparent for both wavelengths over central South America, West Africa, the Indo-Gangetic Plain, and Mongolia/Inner Mongolia. Negative trends over Europe and parts of North Africa are more pronounced in the OMI AOD at 388 nm (Figure 3-S3e) than at 500 nm (Figure 3-S3f). There are small positive trends over west and central United States, parts of South America, parts of North Africa, southern Africa, parts of China, and Australia, with stronger positive trends over Canada, India, and over Central Asia between the Caspian Sea and the Aral Sea.

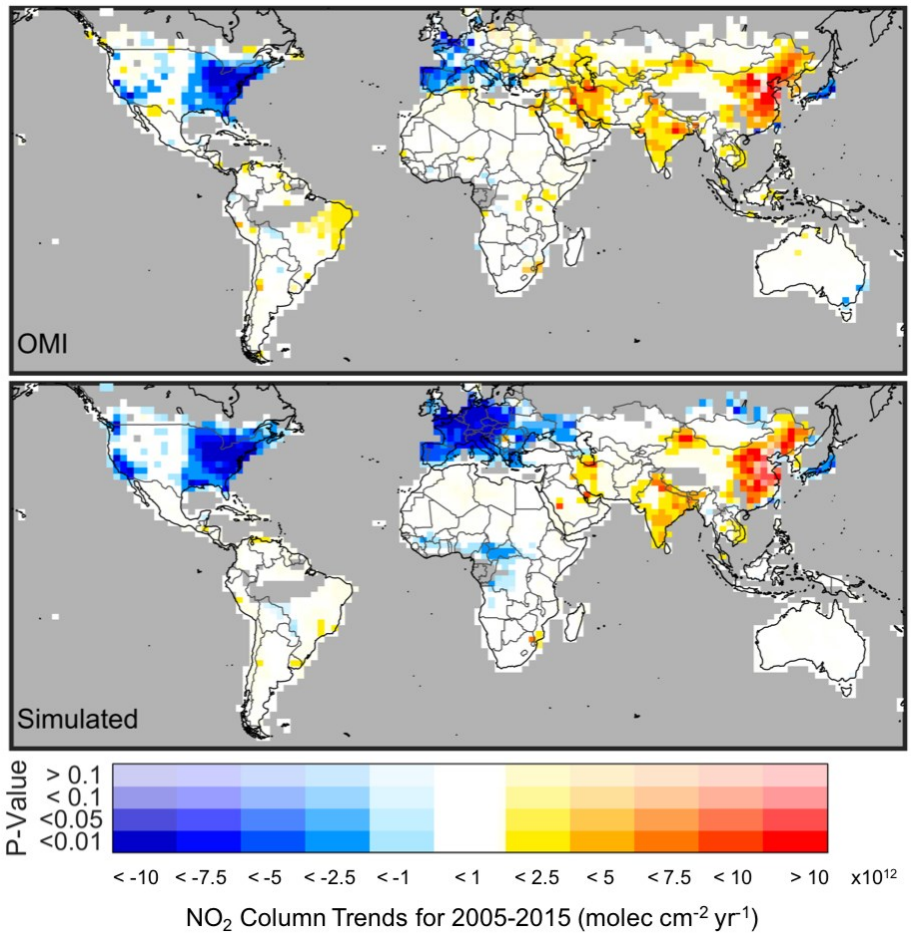

Figure 3-S1: Trends in OMI (top panel) and GEOS-Chem (bottom panel) NO2 columns calculated from the Generalized Least Squares regression of monthly time series values over 2005-2015. The OMI NO2 columns are from NASA's OMNO2 version 2.1 product. The opacity of the colors indicates the statistical significance of the trend. Gray indicates persistent cloud fraction greater than 5%.

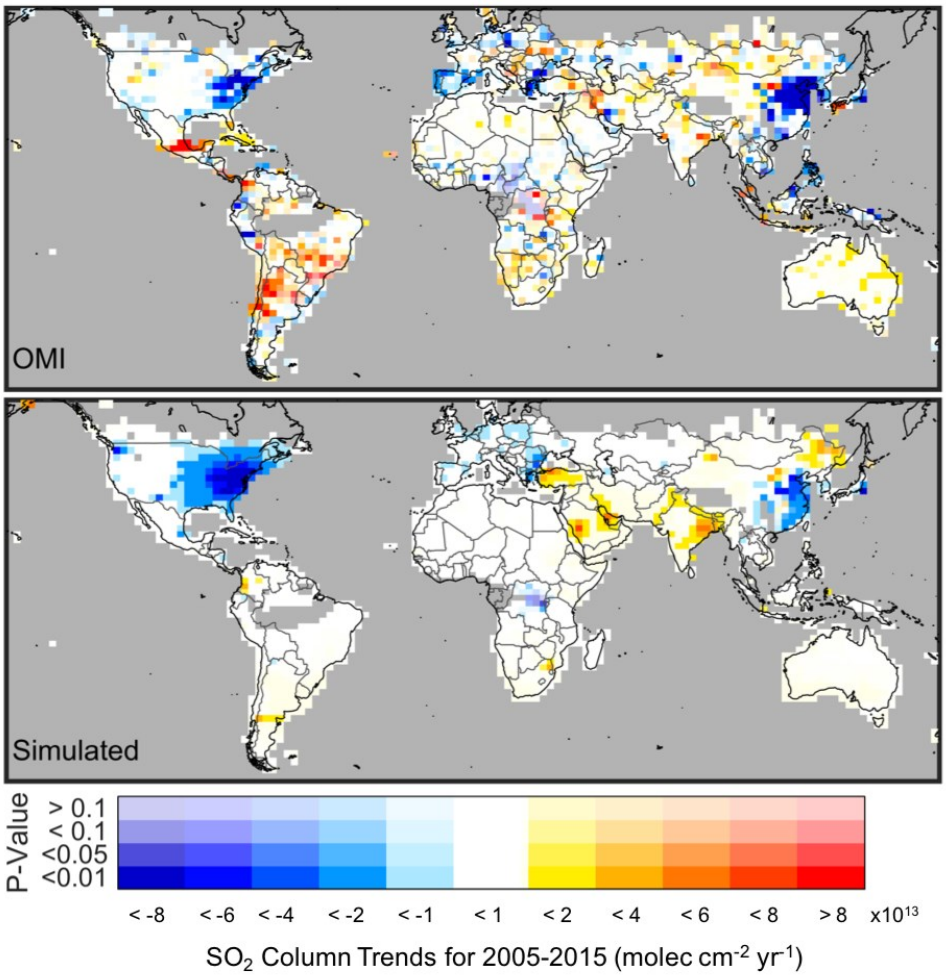

Figure 3-S2: Trends in OMI (top panel) and GEOS-Chem (bottom panel) SO2 columns calculated from the Generalized Least Squares regression of monthly time series values over 2005-2015. The OMI SO2 columns are from NASA's OMSO2 version 1.2.0 product. The opacity of the colors indicates the statistical significance of the trend. Gray indicates persistent cloud fraction greater than 5%.

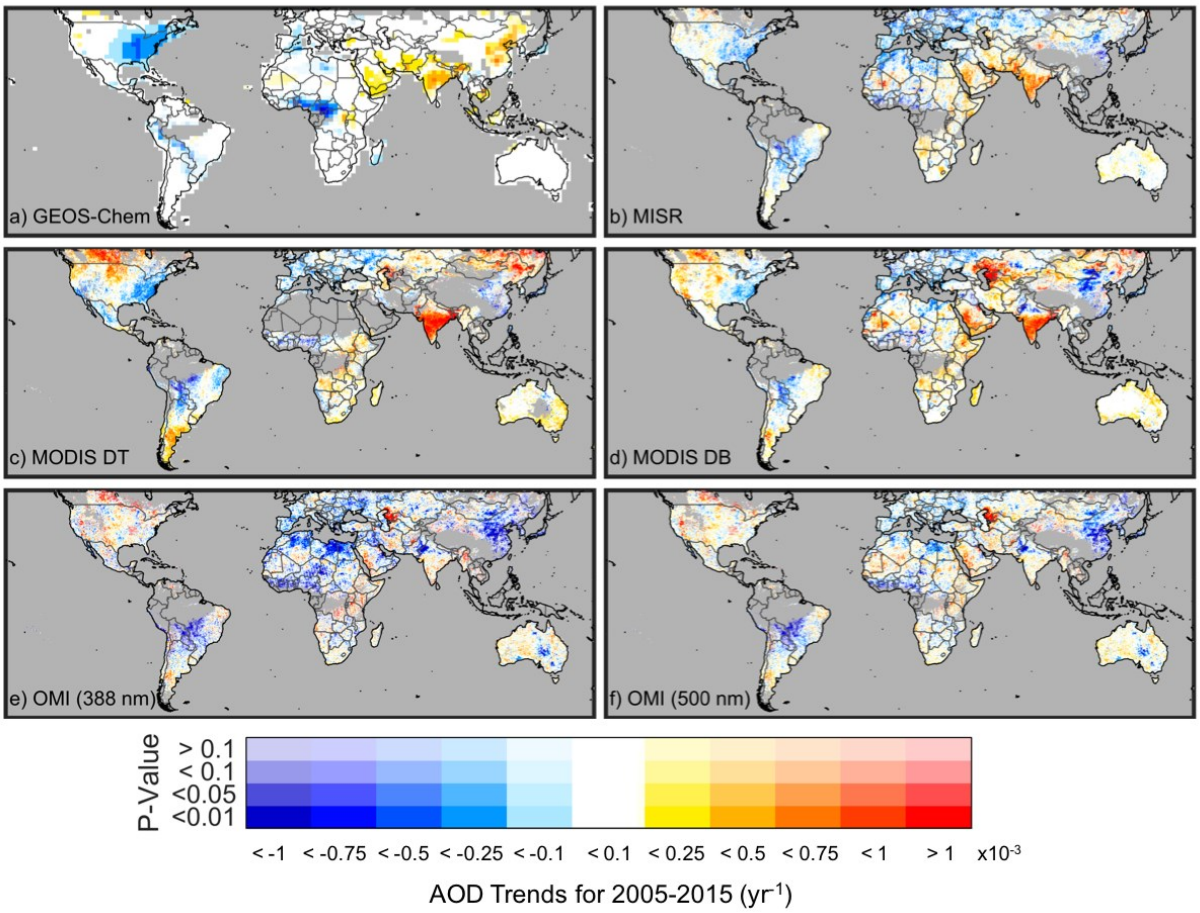

Figure 3-S3: Trends in aerosol optical depth from a) GEOS-Chem (550 nm), b) MISR v22 (550 nm), c) MODIS Terra collection 6 Dark Target algorithm (550 nm), d) the MODIS Terra collection 6 Deep Blue algorithm (550 nm), and the OMI OMAERUV algorithm for e) 388 nm and f) 500 nm. The GEOS-Chem simulation is sampled coincidently with the OMI UVAI product. The trends are calculated from the Generalized Least Squares regression of monthly time series values over 2005-2015. The opacity of the colors indicates the statistical significance of the trend. Gray indicates persistent cloud fraction greater than 5%.

Chapter 4: Improved Global Estimates of Fine Particulate Matter Concentrations and Trends Derived from Updated Satellite Retrievals, Modeling Advances, and Additional Ground-Based Monitors

4.1 Abstract

We investigate the effect of improved geophysical relationships and updated satellite retrieval products on global geophysical and hybrid geophysical-statistical estimates of fine particulate matter ($PM_{2.5}$) concentrations for 2000-2017. We use aerosol optical depth (AOD) from several updated satellite products (MAIAC, MODIS C6.1, and MISR v23), including finer resolution, increased global coverage, and improved long-term stability. We use geophysical relationships between surface $PM_{2.5}$ and AOD simulated by the GEOS-Chem chemical transport model to relate satellite AOD to surface $PM_{2.5}$ concentrations. Updates to the GEOS-Chem simulation include improved dust and secondary organic aerosol chemistry schemes and updated emission inventories. The resultant geophysical $PM_{2.5}$ estimates are highly consistent with ground monitors (R^2=0.81), driven by improvements to the AOD retrievals and GEOS-Chem simulation. We apply geographically weighted regression to the geophysical $PM_{2.5}$ estimates to predict and account for the residual bias with ~9700 $PM_{2.5}$ monitors, yielding further improved agreement (R^2=0.91) with ground monitors, and demonstrating improved agreement compared to earlier estimates (R^2=0.87). The consistent long-term satellite AOD and simulation enables trend assessment over 2000-2017. The populations of North America, Europe, and recently China experienced negative trends in $PM_{2.5}$, while large amounts of the global population experienced positive trends in $PM_{2.5}$ values, particularly in India.

4.2 Introduction

Exposure to fine particulate matter ($PM_{2.5}$) is the leading environmental risk factor for the global burden of disease (GBD 2016 Risk Factors Collaborators et al., 2017) with an estimated 3 million attributable deaths worldwide in 2017. Additionally, the World Health Organization (WHO) estimates that 92% of the world's population lives in areas with annual averaged $PM_{2.5}$ greater than 10 $\mu g/m^3$ (Health Effects Institute, 2019), exceeding their air quality guideline for $PM_{2.5}$ exposure. With limited ground monitoring of $PM_{2.5}$, satellites and global models are critical for constraining the magnitude and trends in concentrations of $PM_{2.5}$ globally, and quantifying exposure-health relationships (West et al., 2016). Recent developments in satellite observations

and retrievals, simulation, and ground monitor sampling offer exciting opportunities to improve global $PM_{2.5}$ estimates.

Several recent advancements in satellite-retrieved aerosol optical depth (AOD) offer the prospect of improving global $PM_{2.5}$ estimates. Collection 6.1 (C6.1) of MODIS (MODerate resolution Imaging Spectroradiometer) retrieved AOD includes updated radiometric calibration improving the stability of MODIS measured radiances over the entire record and important updates to the Dark Target (DT) (Gupta et al., 2016) and Deep Blue (DB) (Hsu et al., 2019; Sayer et al., 2019) algorithms. The MAIAC (Multi-Angle Implementation of Atmospheric Correction) algorithm (Lyapustin et al., 2018a) provides AOD retrieved from MODIS C6 radiances at a resolution of 1 km and is now extended to global coverage for the entire MODIS record. The recently released MISR (Multi-angle Imaging Spectroradiometer) version 23 algorithm (Franklin et al., 2017; Garay et al., 2017) now provides AOD retrievals at 4.4 km resolution, finer than the 17.6 km resolution of the previous version 22.

Concurrent development of chemical transport models offer the prospect of improved characterization of the $PM_{2.5}$ distribution and the geophysical relationship of AOD to $PM_{2.5}$. A recent assimilation (MERRA-2) (Gelaro et al., 2017) provides consistent meteorological inputs for 1979-present. Improved representations of secondary organic aerosol (Pye et al., 2010; Marais et al., 2016) and fine dust (Ginoux et al., 2012; Zhang et al., 2013a) better simulate surface $PM_{2.5}$ concentrations. The development of an anthropogenic fugitive, combustion, and industrial dust (AFCID) emission inventory now represents anthropogenic crustal material (Philip et al., 2017b). An updated fire emissions inventory (GFED4) (Giglio et al., 2013b) provides increased global coverage and finer resolution biomass burning emissions. Significant updates to regional emissions inventories of aerosols and their precursors over China (Li et al., 2017b), elsewhere in Asia (Li et al., 2017b), the United States (Travis et al., 2016), and Europe (http://www.emep.int) provide improved time-varying information, especially for recent years.

The ground-based $PM_{2.5}$ measurement network has expanded considerably in recent years with ~9690 direct $PM_{2.5}$ monitor sites (World Health Organization, 2018), increasing monitor density particularly in China and India. Improved statistical methods have been developed to obtain estimates of surface $PM_{2.5}$ concentrations from satellite AOD and ground monitor data, including empirical relationships between satellite AOD and $PM_{2.5}$ from ground monitors (Liu et al., 2005;

Kumar et al., 2007), Land Use Regression (LUR) models in conjunction with satellite AOD (de Hoogh et al., 2018), and Geographically Weighted Regression (GWR) with meteorological and land use information with satellite AOD at $PM_{2.5}$ monitor sites (Ma et al., 2014; Song et al., 2014). Several studies have found that including geophysical fields from a chemical transport model aids statistical fusion at large spatial scales (Di et al., 2016; van Donkelaar et al., 2015, 2016; Friberg et al., 2017; Shaddick et al., 2018).

In this work, we investigate the effects of recent developments in satellite AOD, simulation, and ground monitor data on satellite-derived $PM_{2.5}$ estimates and produce global $PM_{2.5}$ estimates for the years 2000-2017. We combine satellite AOD from the newly released MAIAC, MISRv23, and C6.1 MODIS products. We conduct an updated simulation using the global chemical transport model GEOS-Chem to represent the geophysical relationship between $PM_{2.5}$ and AOD, and also as an additional AOD source. We investigate the impact of these changes on previous satellite-derived $PM_{2.5}$ estimates that follow a similar methodology (van Donkelaar et al., 2016). Taking advantage of the improved long-term consistency in satellite AOD and simulated meteorology, we calculate the 2000-2017 trends in geophysical $PM_{2.5}$ values, and examine the monthly time-series. We then statistically fuse the geophysical $PM_{2.5}$ surface with the recently released ground monitor dataset from the World Health Organization (WHO), and investigate the impact of increased ground-based monitoring. We examine the regional distributions of population as a function of 1) $PM_{2.5}$ concentrations and 2) 2000-2017 $PM_{2.5}$ trends to gain insight into the distribution of ambient $PM_{2.5}$ effects worldwide.

4.3 Methods

4.3.1 Satellite AOD Sources

A detailed description of the satellite AOD sources used is given in the Supplement. We use AOD at 550 nm retrieved from radiances measured by four satellite instruments: twin MODerate resolution Imaging Spectroradiometer (MODIS) instruments, the Multi-angle Imaging Spectroradiometer (MISR) instrument, and the Sea-viewing Wide Field-of-view Sensor (SeaWiFS) instrument.

The twin MODIS instruments have flown on the Terra and Aqua satellites since 2000 and 2002, respectively, providing daily global coverage (Sayer et al., 2014). We use AOD retrieved from

three retrieval algorithms that process MODIS measured radiances: Dark Target (DT), Deep Blue (DB), and the Multi-Angle Implementation of Atmospheric Correction (MAIAC).

The DT retrieval algorithm (Levy et al., 2013) is designed to retrieve AOD over dark surfaces (e.g. vegetated land surfaces and dark soils). The DB retrieval algorithm (Hsu et al., 2019) uses blue wavelength measurements where the surface reflectance over land tends to be much lower than at longer wavelengths, allowing for the retrieval of aerosol properties over both bright and dark surfaces. We use the recently released collection 6.1 of the MODIS retrieved AOD products, which include spatial resolution of 10 km and several updates to the DT (Gupta et al., 2016) and DB (Hsu et al., 2019; Sayer et al., 2019) algorithms.

The MAIAC algorithm (Lyapustin et al., 2018a) retrieves AOD at a spatial resolution of 1 km over both bright and dark land surfaces. MAIAC was officially released in May 2018, providing AOD globally for the entire MODIS record. However, this work started earlier and used an internally released MAIAC dataset that lacked parts of Canada, eastern Siberia, and the large Indo-Pacific region (see Fig. 4-2).

The SeaWiFS instrument flew on SeaStar and was operational between 1997-2010. SeaWiFS maintained a highly accurate and stable calibration over its lifetime (Sayer et al., 2012) providing daily global coverage. We use the version 4 SeaWiFS Deep Blue (Sayer et al., 2012; Hsu et al., 2013) data set which has a spatial resolution of 13.5 km.

The MISR instrument is also onboard the Terra satellite and has been operational since 2000 providing global coverage once per week (Diner et al., 1998). The MISR retrieval algorithm provides AOD retrievals over bright and dark land surfaces (Martonchik et al., 2009). We use AOD retrieved from the recently released MISRv23 algorithm (Garay et al., 2017), which provides AOD at a spatial resolution of 4.4 km, a significant improvement over the 17.6 km resolution in the previous version of MISRv22.

4.3.2 Simulated relationship of surface $PM_{2.5}$ and total column AOD

To estimate surface concentrations of $PM_{2.5}$ from satellite AOD (AOD_{SAT}), we use the local, coincident ratio (η) of simulated surface $PM_{2.5}$ concentrations ($PM_{2.5,SIM}$) to simulated total column AOD (AOD_{SIM}):

$$PM_{2.5,SAT} = \eta \text{ x } AOD_{SAT} \qquad [4\text{-}1]$$

where

$$\eta = PM_{2.5,SIM} / AOD_{SIM} \quad [4\text{-}2].$$

η is a function of the factors that relate $PM_{2.5}$ mass to satellite observations of AOD (e.g. aerosol size, aerosol composition, diurnal variation, relative humidity, and the vertical structure of aerosol extinction (van Donkelaar et al., 2010)). A full description of the derivation of η can be found in van Donkelaar et al. (2006). To account for differences in temporal sampling of the AOD data sources, we calculate daily values of η as the ratio of 24-hr ground-level $PM_{2.5}$ for a relative humidity of 35%, to total-column AOD for ambient relative humidity sampled at satellite overpass time.

Obtaining accurate η values depends on the simulation's ability to accurately model $PM_{2.5}$ concentrations and AOD. For our simulation, we use v11-01 of the GEOS-Chem chemical transport model (http://geos-chem.org). A detailed description of the simulation is included in the Supplement. Our simulation is driven by assimilated meteorological data from the recent MERRA-2 Reanalysis of the NASA Global Modeling and Assimilation Office (GMAO), which offers a consistent assimilation from 1979 (Molod et al., 2015). We conduct our simulation for the years 2000–2017 at a spatial resolution of $2^\circ \times 2.5^\circ$ with a nested resolution of 0.5° x 0.625° over North America, Europe, and China, and 47 vertical levels. The top of lowest model layer is ~100 m. Our simulation includes improved representations of secondary organic aerosol (Pye et al., 2010; Marais et al., 2016) and fine dust (Ginoux et al., 2012; Zhang et al., 2013a) which better simulate surface PM concentrations. We also use the anthropogenic fugitive, combustion, and industrial dust (AFCID) emission inventory, which now provides a representation of anthropogenic crustal material (Philip et al., 2017b). An updated version of the Global Fire Emissions Database (GFED4) provides increased global coverage and finer resolution biomass burning emissions (Giglio et al., 2013b). We include updated regional emissions inventories (summarized in Table 4-S1) of aerosols and their precursors over China (MEIC; Li et al., 2017b), India (Lu et al., 2011), elsewhere in Asia (MIX; Li et al., 2017b), the United States (EPA/NEI11; Travis et al., 2016), and Europe (EMEP; http://www.emep.int).

4.3.3 Combined $PM_{2.5}$ estimated from satellites and simulation

We calculate geophysical $PM_{2.5}$ estimates following van Donkelaar et al. (2016), with updates to (1) ground-based $PM_{2.5}$ and AOD measurements, (2) satellite AOD products, (3) GEOS-Chem

simulation, and (4) resolution of our analysis. A detailed description of the algorithm is provided in van Donkelaar et al. (2016) and in the Supplement. There are two main steps of the algorithm: the intercalibration of the satellite and simulated AOD sources, and the calculation of combined $PM_{2.5}$ from the calibrated AOD sources.

For the intercalibration of satellite and simulated AOD sources, each source is first translated onto a common 0.05°x0.05° grid by area-weighting satellite retrievals and linearly interpolating simulated values. This resolution is finer than the 0.1°x 0.1° resolution used previously (van Donkelaar et al., 2016), given the finer resolution provided by the new versions of MISR (4.4 km) and MAIAC (1 km) AOD. For a consistent definition of uncertainty, we compare the daily satellite AOD values from each dataset with daily AOD measurements at 550 nm from AERONET (Aerosol Robotic Network) (Holben et al., 1998), a global sun photometer network that provides AOD measurements with high accuracy (uncertainty<0.02; Eck et al., 1999). We use level 2 of the recently released version 3 AERONET data (Giles et al., 2019).

The different sources of error associated with satellite and simulated AOD require care in accounting for their relative uncertainties (van Donkelaar et al., 2016). Briefly, one of the main sources of uncertainty associated with satellite retrieved AOD is the surface treatment used in the retrieval (Li et al., 2009), which we assess by comparison with AERONET as a function of land type. For the simulated AOD, to account for errors due to species-specific emissions and assumed aerosol microphysical properties, we calculate the relative uncertainty based on the simulated fractional aerosol composition applied to each daily AERONET observation following van Donkelaar et al. (2013).

The daily surface $PM_{2.5}$ concentrations from each data source are obtained by applying the daily simulated AOD to $PM_{2.5}$ ratios (η) to the coincident daily calibrated AOD sources. Monthly means are calculated from the daily $PM_{2.5}$ values. The monthly mean $PM_{2.5}$ from each source are then combined using a weighted average (equation 4-S4). Where available, spatial information from the 1 km MAIAC AOD retrieval is incorporated by applying the climatology of its retrieved relative variation between 0.01° and 0.05°. Where MAIAC is unavailable, monthly AOD and $PM_{2.5}$ are linearly interpolated onto a 0.01°x0.01° grid.

4.3.4 Hybrid $PM_{2.5}$ estimates

We use Geographically Weighted Regression (GWR) (Fotheringham et al., 1998; Brunsdon et al., 2010) to predict and account for the bias in the annual mean of our geophysical $PM_{2.5}$ estimates as described in van Donkelaar et al. (2016). We perform the GWR between our annual mean geophysical $PM_{2.5}$ estimates and annual $PM_{2.5}$ concentrations measured by ground monitors. We use monitor-specific ground-based measurements of $PM_{2.5}$ from the WHO Global Ambient Air Quality Database (World Health Organization, 2018), which provides annual measurements for the years 2010-2017. Supplemental Table 4-S2 summarizes the global number of measurements for each year. The predictor variables used in the regression are associated with uncertainties in the simulated relation of $PM_{2.5}$ to AOD, such as simulated aerosol types, sub-grid topographical variation and urban surfaces (equation 4-S5).

4.4 Results and Discussion

The first three panels of Figure 4-1 show the combined AOD, simulated η ($PM_{2.5}$/AOD), and combined $PM_{2.5}$ estimates for 2000-2017. The logarithmic $PM_{2.5}$ color-scale (bottom) is directly proportional to the logarithmic AOD (top) and η (middle) color-scales to facilitate comparison of features between plots. Several factors affect the simulated relation of AOD and $PM_{2.5}$ (van Donkelaar et al., 2010; Jin et al., 2019). Since AOD is at ambient relative humidity and $PM_{2.5}$ is at controlled relative humidity, high η values exist over desert regions in North Africa and the Middle-East where aerosols are less hygroscopic (van Donkelaar et al., 2006; van Donkelaar et al., 2010) . Values of η are lower for hygroscopic aerosols, as their dry volume is significantly smaller

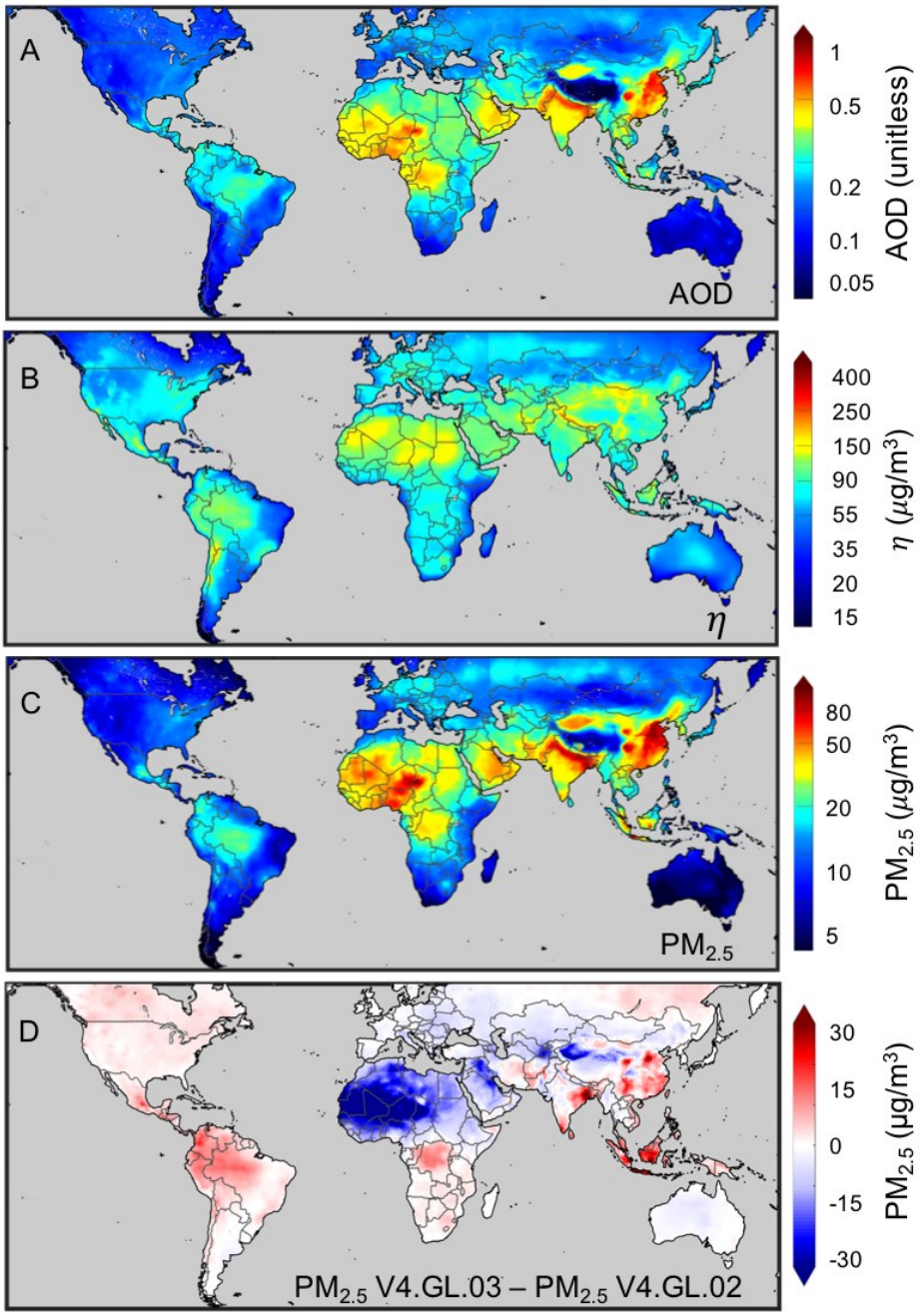

Figure 4-1: The combined AOD (A), simulated η ($PM_{2.5}$/AOD) (B), and combined $PM_{2.5}$ estimates (C) for 2000-2017. The logarithmic $PM_{2.5}$ color-scale (C) is directly proportional to the logarithmic AOD (A) and η (B) color-scales, obtained by normalizing the global average AOD and global average η to that of $PM_{2.5}$. The bottom panel (D) shows the difference between this updated version (V4.GL.03) of geophysical $PM_{2.5}$ estimates and the previous version (V4.GL.02) from van Donkelaar et al. (2016) for 2011-2016. Grey denotes water.

than under ambient conditions. Higher η values over industrial regions in India and eastern China reflect the enhanced near-surface aerosol concentrations in source regions that increase the ground level to columnar fraction. Over southern China, higher AOD compared to $PM_{2.5}$ (e.g smaller η values) in part reflect the transport of biomass burning aerosol from southeast Asia at high altitudes (Deng et al., 2008; Zhang et al., 2018). Relatively low η values over northern regions in Canada and Russia occur where $PM_{2.5}$ concentrations are lower and a higher fraction of the aerosol tends to be aloft. Enhanced η values over the Andes and the Tibetan Plateau reflect the diminished AOD column over elevated topography.

The bottom panel of Figure 4-1 shows the difference between this updated version (V4.GL.03) of geophysical $PM_{2.5}$ estimates and the previous version (van Donkelaar et al., 2016) (V4.GL.02) for 2011-2016. The largest differences are apparent over desert regions, with a decrease in $PM_{2.5}$ concentrations of ~-30 $\mu g/m^3$. This difference reflects the influence of the improved dust scheme (Ginoux et al., 2012; Zhang et al., 2013a) used in the updated GEOS-Chem simulation on simulated η. There are increases in $PM_{2.5}$ concentrations of ~5-15 $\mu g/m^3$ over South America, central Africa, India, China, and South-east Asia, with smaller increases of ~2-5 $\mu g/m^3$ over parts of North America and Russia. These differences reflect the updated emissions inventories and secondary organic aerosol chemistry scheme (Pye et al., 2010; Marais et al., 2016) used in the updated GEOS-Chem simulation.

Figure 4-2 shows the mean area-based weighting over 2000-2017 of each AOD source used in the combined estimate. For MODIS Dark Target and Deep Blue, only Terra-based retrievals are shown, although Aqua is also included in the combined estimate. Therefore a total of 8 sources contribute to the combined product, and an individual source of average quality would have a weighting of ~1/8 (12%). Values in black in the bottom-left of each panel indicate the population-

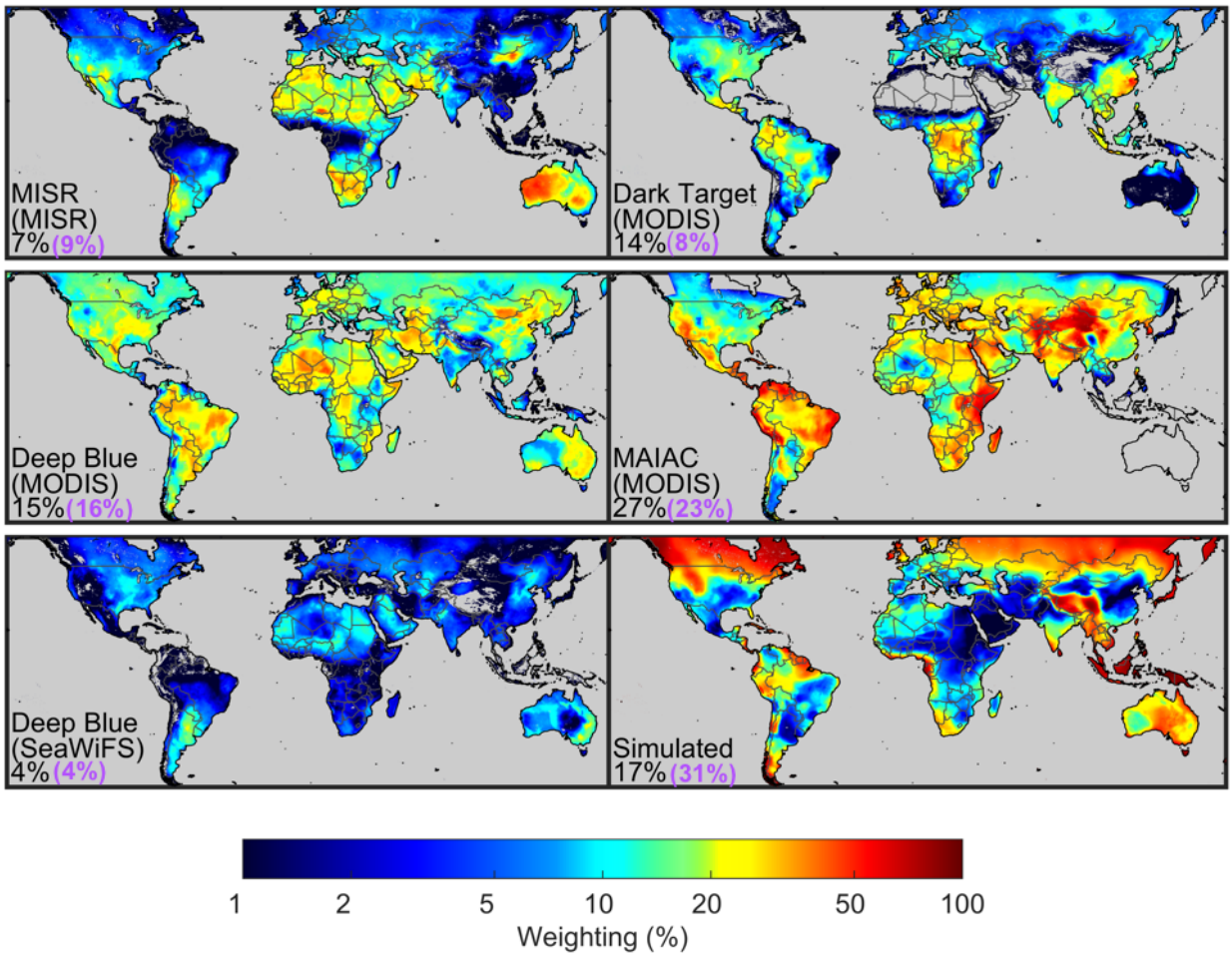

Figure 4-2: Mean contribution of each source to the combined $PM_{2.5}$ estimate for 2000-2017. Values in black in the bottom-left of each panel indicate the population-based mean weighting at locations with available data, while purple values indicate the area-based mean weighting. The retrieval algorithm name is given in the lower left of each panel, with the instrument name in brackets. Dark Target and Deep Blue MODIS correspond to Terra- based retrievals only. Grey denotes missing data or water.

based mean weighting at locations with available data, whereas purple values in parentheses indicate the area-based mean weighting. The MAIAC satellite source contributes the highest percentage to the population-based geophysical $PM_{2.5}$ estimate with a mean weighting of 27% reflecting its strong overall performance including over arid and mountainous regions with difficult surface conditions. The large increase in MAIAC contribution compared to the 12% mean contribution in earlier work (van Donkelaar et al., 2016) is related to its near global coverage, which was not previously available. MODIS Deep Blue performs well over most parts of the world, especially over deserts, with a population based mean weighting of 15%. MODIS Dark

Target (14% population-based) performs well over Central America, central Africa, and Southeast Asia. MISR (7% population-based mean weighting) is strongest over regions with difficult surface conditions such as deserts. SeaWiFS DB is weighted less heavily (4% population-based mean weighting) compared to the other sources, largely due to reduced sampling frequency. Simulated AOD has a population-based mean weighting of 17% due to large contributions over northern regions and south-eastern Asia where seasonal snow-cover and cloud-cover respectively inhibit satellite retrievals.

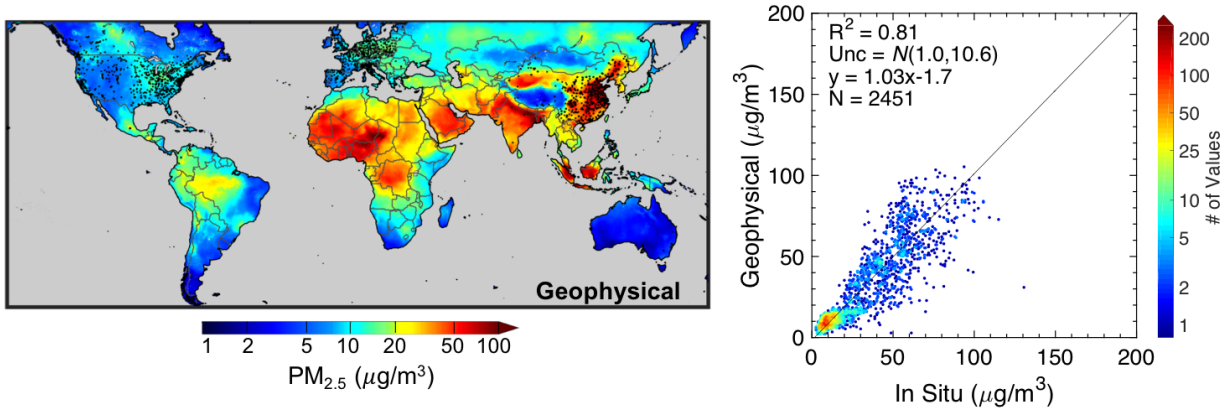

Figure 4-3: Left: Geophysical $PM_{2.5}$ for 2015. Black dots represent monitor locations. Grey denotes water. Right: Annual mean geophysical $PM_{2.5}$ versus coincident annual mean in situ values for 2015. Included on the plots are the coefficient of variation (R^2), the normal distribution of uncertainty (N(bias,variance)), the line of best fit (y), and the number of comparison points (N). The color-scale indicates the number density of observations at each point.

Figure 4-3 shows the geophysical $PM_{2.5}$ estimates for 2015. Elevated concentrations are apparent over East Asia, South Asia, the Middle-East, North Africa, and central Canada (due to biomass burning). Evaluation of these geophysical estimates versus ground-based measurements yields excellent consistency on an annual mean basis with R^2=0.81 and a slope of 1.03. This excellent agreement offers promise for satellite-derived $PM_{2.5}$ in regions with low monitor density, as our geophysical estimates are independent of ground monitor data.

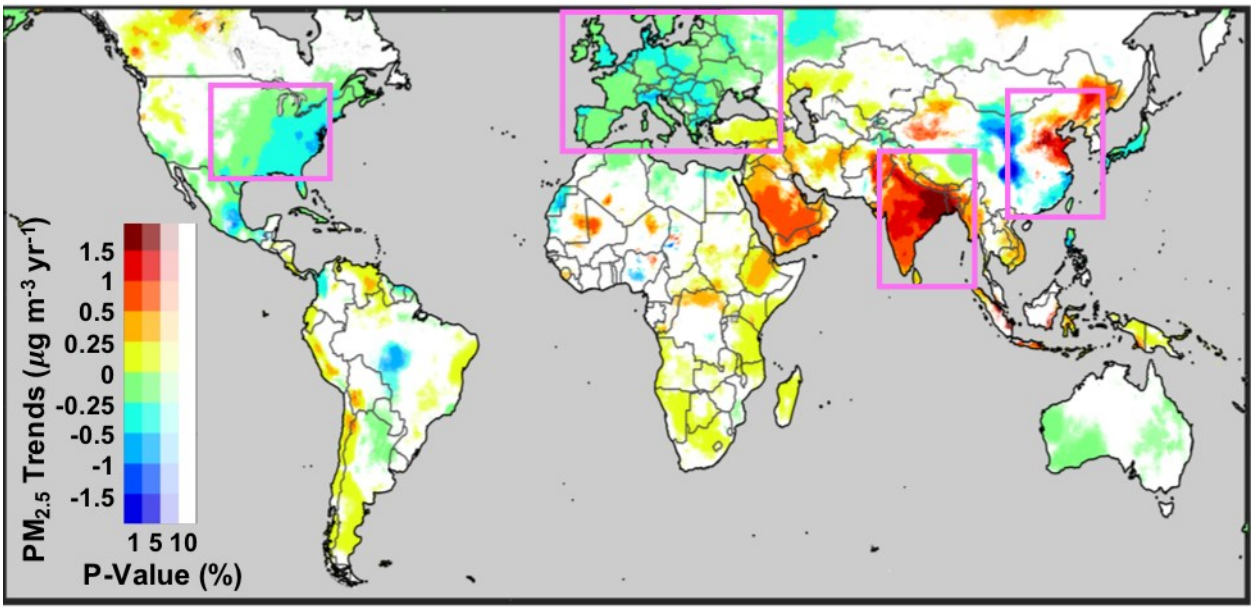

Figure 4-4: Trends in geophysical $PM_{2.5}$ values calculated from the generalized least squares regression of monthly time series values during 2000-2017. Warm colors indicate positive trends, cool colors indicate negative trends, and the opacity of the colors indicate the statistical significance of the trends. Grey denotes water. Magenta boxes indicate areas featured for regional analysis in Figure 4-5.

The long-term radiometric calibration of the newly released satellite AOD products and the long-term consistency of the meteorology and emissions used in the GEOS-Chem simulation enable assessment of trends. Figure 4-4 shows the trends in our geophysical $PM_{2.5}$ values for 2000-2017, calculated using generalized least squares regression (GLS) (Weatherhead et al., 1998, 2002) as implemented by Boys et al. (2014). There are statistically significant (p-value<0.05) positive trends in $PM_{2.5}$ of 1 to 1.5 $\mu g/m^3/yr$ over India and of 0.25 to 0.5 $\mu g/m^3/yr$ over the Middle-East, central and southern Africa, and Canada. There is a small area of positive trends of ~1 $\mu g/m^3/yr$ over eastern China and a small region of negative trends of -1 $\mu g/m^3/yr$ over northern China, however most of East Asia does not exhibit statistically significant trends when taken over the entire time period. There are statistically significant, negative trends in $PM_{2.5}$ values of -1 to -0.25 $\mu g/m^3/yr$ over the eastern US, Europe, central South America, and Australia.

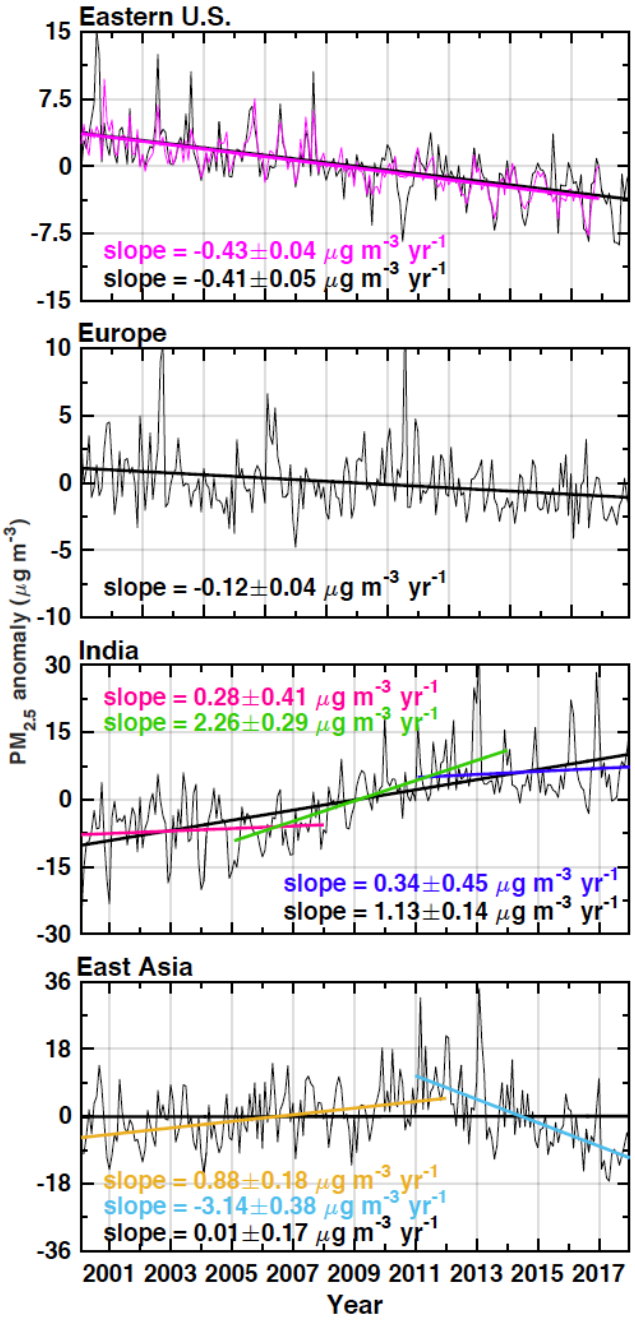

Figure 4-5: Regional monthly time series anomaly plots of geophysical $PM_{2.5}$ values for 2000-2017 with their corresponding linear fits (in black). In the top panel, magenta lines indicate the time series and corresponding linear fit for EPA measurements over the Eastern U.S. In the third panel, the 2000-2007 linear fit over India is shown in pink, the 2005-2013 linear fit is shown in green, and the 2011-2017 linear fit is shown in dark blue. In the bottom panel, the 2000-2012 linear fit over East Asia is shown in yellow, while the 2011-2017 linear fit is shown in blue.

Figure 4-5 shows the regional time-series calculated using the GLS of monthly geophysical $PM_{2.5}$ anomalies for the eastern US, Europe, East Asia, and India. The time-series plots for the eastern US and Europe exhibit negative trends, with slopes of -0.41±0.05 μg/m^3/yr and -0.12±0.04 μg/m^3/yr respectively. These negative trends reflect the emission controls implemented in these regions (Leibensperger et al., 2012; Klimont et al., 2013; Curier et al., 2014; Simon et al., 2015; Xing et al., 2015; Li et al., 2017a). Over the eastern US we evaluate the time-series coincidently sampled with EPA ground measurements for 2000-2016 and find excellent consistency with slope -0.43±0.04 μg/m^3/yr. There is a positive trend in $PM_{2.5}$ concentrations over India with a slope of 1.13±0.14 μg/m^3/yr, reflecting the increasing emissions of anthropogenic aerosol and their precursors (Lu et al., 2011; Klimont et al., 2017). Three separate regimes are visible over India: a small positive trend (slope 0.28±0.41 μg/m^3/yr; pink) for ~2000-2007, a period of a large positive trend (slope 2.26±0.29 μg/m^3/yr; green) for ~2005-2013 which seems to drive the positive 2000-2017 trend, then another small positive trend (slope 0.34±0.45 μg/m^3/yr; dark blue) for ~2011-2017. Over East Asia, there appears to be an insignificant long-term trend with a slope of 0.01±0.17 μg/m^3/yr for 2000-2017. A positive trend in $PM_{2.5}$ concentrations (slope 0.88±0.18 μg/m^3/yr; yellow) is visible until ~2012, after which the trend becomes strongly negative (-3.14±0.38 μg/m^3/yr; light blue), reflecting the emissions controls placed on SO_2 and NO_x in China around this time (Lu et al., 2011; Wang et al., 2015; Fioletov et al., 2016).

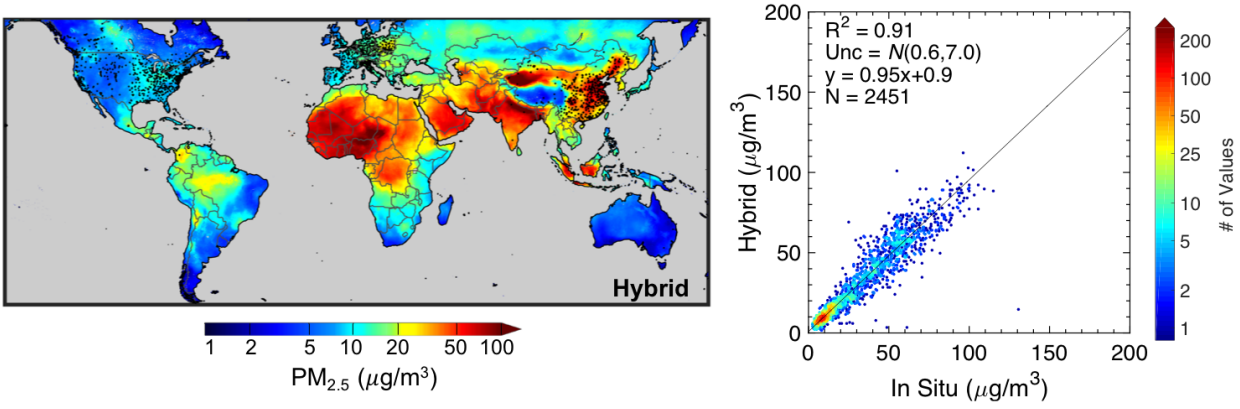

Figure 4-6: Left: Hybrid $PM_{2.5}$ for 2015. Black dots represent monitor locations. Grey denotes water. Right: Annual mean geophysical $PM_{2.5}$ versus coincident annual mean in situ values for 2015. Included on the plots are the coefficient of variation (R^2), the normal distribution of uncertainty (N(bias,variance)), the line of best fit (y), and the number of comparison points (N). The color-scale indicates the number density of observations at each point.

We next statistically fuse the geophysical estimates of $PM_{2.5}$ with the in situ ground monitor data. Figure 4-S1 shows the predicted bias from GWR, while Figure 4-S2 shows the net impact of the individual predictors on the predicted bias. Figure 4-6 shows the resulting statistically fused (hybrid) estimates for 2015. The scatterplot shows 10-fold out of sample 10% cross validation at sites that were not used in the GWR regression. Statistical fusion explains 10% of the variance in the ground-based measurements, increasing to R^2=0.91. The agreement for the entire dataset of hybrid $PM_{2.5}$ values was very similar (R^2=0.90) to the agreement of just the cross-validated sites described above, suggesting the impact of overfitting is small, and is comparable to other recent statistical fusion techniques (Shaddick et al., 2018).

The agreement of our hybrid $PM_{2.5}$ estimates (V4.GL.03) with ground monitors is significantly improved compared to the agreement of V4.GL.02 in van Donkelaar et al. (2016) for more recent years (2014-2016), as is shown in Table 4-S3. There is also improved agreement within V4.GL.03 for 2014-2016 compared to earlier years (Table 4-S3), demonstrating the value of increased ground-monitoring, particularly in China. The lack of a change in the agreement among the years 2014-2016, where there was still a significant increase in the number of comparison points, suggests that estimates would benefit from increasing the number of monitors in underrepresented regions (e.g. India, Africa, the Middle-East, and South America), rather than increasing the number of monitors in regions where they are already available (i.e. North America, Europe, and China).

The top three panels of Figure 4-7 show the regional distributions of the global population as a function of hybrid $PM_{2.5}$ concentrations for 2000, 2010, and 2017, following the method of Apte et al. (2015). The bottom panel shows the regional distributions of the global population as a function of the 2000-2017 trends from Figure 4-4. Only statistically significant (p-value<0.05) trends were considered, therefore the populations in the bottom plot reflect those exposed to statistically significant trends, not the total populations.

For all three years (top panels) the majority of the global population was exposed to $PM_{2.5}$ concentrations above the WHO air quality guideline of 10 $\mu g/m^3$. However, a significant fraction of the population in the Americas and Europe shifted toward lower $PM_{2.5}$ concentrations over 2000-2017, reflected in the fraction of these populations experiencing negative trends (bottom panel). Over 2000-2017, 85% of the total population in North America experienced statistically

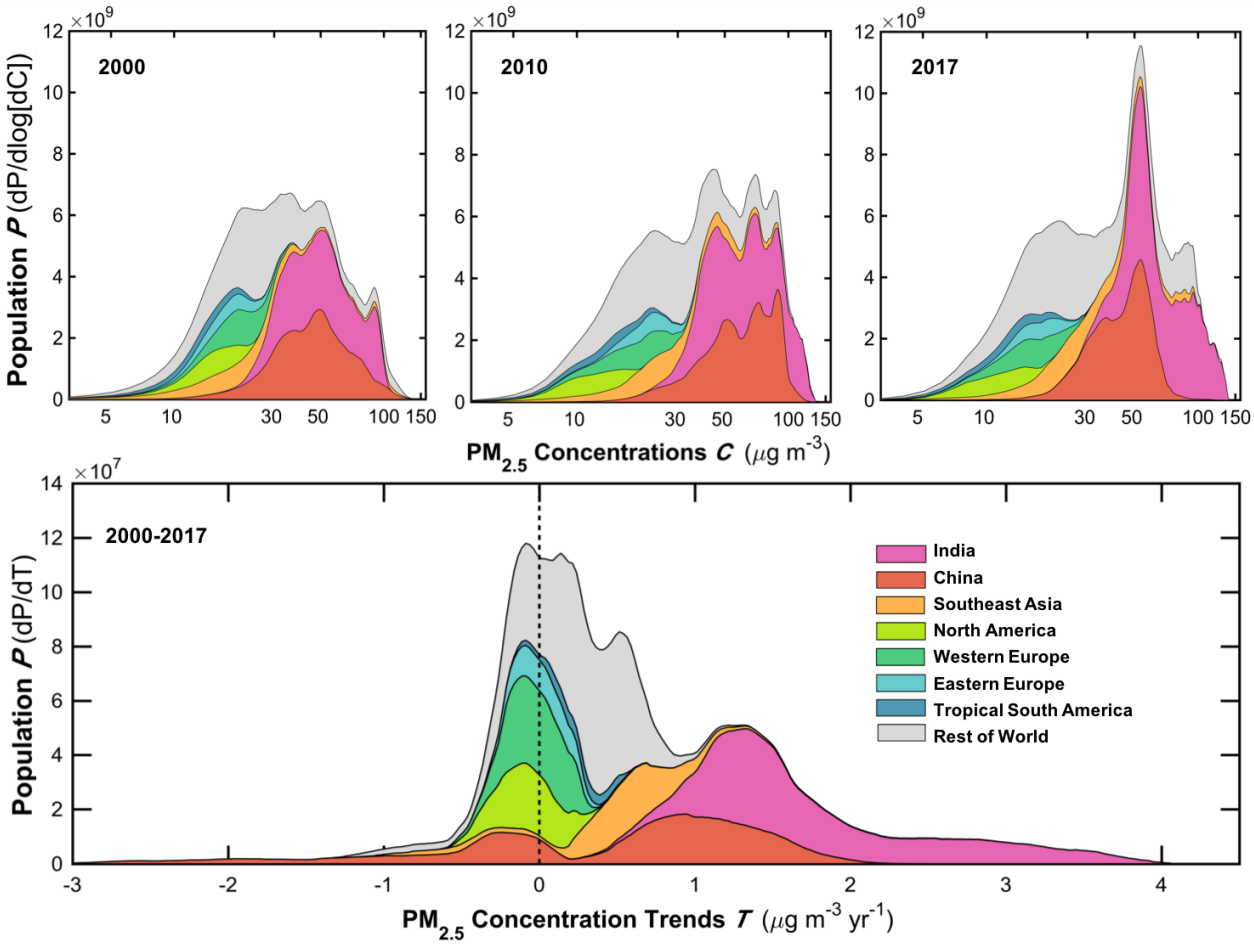

Figure 4-7: Top: Regional distribution of population as a function of $PM_{2.5}$ concentrations for 2000 (left), 2010 (middle), and 2017 (right). This data is summarized in Table 4-S4. Plotted data reflect local smoothing of bin-width normalized distributions computed over 400 logarithmically spaced bins (range 0.1-400 μg m^{-3}) following Apte et at. (2015); equal-sized plotted areas reflect equal populations. Bottom: Regional distribution of population as a function of $PM_{2.5}$ trends with statistical significance (p-value < 0.05) for 2000-2017.

significant negative trends while 0.4% experienced positive trends. An increasing amount of the population of India was exposed to $PM_{2.5}$ concentrations of 50-150 μg/m^3 over 2000-2017 (top panels), with 100% of the total population experiencing positive trends. A large fraction of the population in China shifted towards higher $PM_{2.5}$ concentrations of 50-100 μg/m^3 (top panels) between 2000 and 2010, but between 2010 and 2017 that fraction significantly decreased as a large fraction of the population shifted towards ~50 μg/m^3. The population distribution is spread out over both negative and positive trends (bottom panel). Over 2000-2017, 18% of the total

population in China experienced negative trends, while 33% experienced positive trends. Globally, 26% of the total population experienced negative trends, while 38% experienced positive trends.

4.5 Conclusions

Recent developments in satellite AOD, simulation, and ground monitor data enabled improved global $PM_{2.5}$ estimates and trends over the years 2000-2017. The updated satellite AOD sources benefited from finer resolution (MISR), increased global availability (MAIAC), and updated radiometric calibration that improves the stability of all MODIS products over time. The updated GEOS-Chem simulation benefitted from consistent long-term meteorology (MERRA-2), improved dust and SOA chemistry schemes, updated biomass burning emissions, and updated emission inventories providing improved time-varying information for more recent years, especially over China and India. The geophysical $PM_{2.5}$ estimates exhibited significant agreement with ground monitors with an R^2=0.81, providing confidence in the utility of the geophysical estimates in regions with low monitor density. Trends for 2000-2017 over the eastern United States in our geophysical $PM_{2.5}$ values (-0.41±0.05 $\mu g/m^3/yr$) were consistent with trends in measurements (-0.43±0.04 $\mu g/m^3/yr$). Statistical fusion explained an additional 10% of the variance in the $PM_{2.5}$ estimates, yielding an improved agreement (R^2=0.91) with cross-validated ground monitor sites. The populations of North America, Europe, and recently China experienced negative trends in $PM_{2.5}$, while large amounts of the global population experienced positive trends in $PM_{2.5}$ values, particularly in India. This new iteration of $PM_{2.5}$ estimates provides an improved geophysical and hybrid dataset to be used for health impact studies, and is especially valuable for regions with low monitor density.

4.6 Acknowledgements

This work was supported by the Natural Sciences and Engineering Research Council (NSERC) and the United Nations Environment Programme (UNEP). Melanie Hammer was partially supported by the Killam Trusts.

4.7 Supplement

4.7.1. Description of Satellite AOD Sources

We use AOD at 550 nm retrieved from radiances measured by four satellite instruments: twin MODerate resolution Imaging Spectroradiometer (MODIS) instruments, the Multi-angle Imaging Spectroradiometer (MISR) instrument, and the Sea-viewing Wide Field-of-view Sensor (SeaWiFS) instruments.

The twin MODIS instruments have flown on the Terra and Aqua satellites since 2000 and 2002, respectively. Terra has a descending orbit, passing the equator at 10:30 local time, while Aqua has an ascending orbit, passing equator at 13:30 local time. Both MODIS instruments have a wide spectral range of 0.41 μm to 14.5 μm and a broad swath width of 2330 km which allows for nearly global daily coverage (Sayer et al., 2014). We use AOD retrieved from three retrieval algorithms that process MODIS measured radiances: Dark Target (DT), Deep Blue (DB), and the Multi-Angle Implementation of Atmospheric Correction (MAIAC).

The DT retrieval algorithm (Levy et al., 2013) performs a simultaneous inversion of two visible (0.47 μm and 0.66 μm) and one shortwave-IR (2.12 μm) channel to retrieve AOD over dark surfaces (i.e. vegetated land surfaces and dark soils). DT also retrieves AOD over ocean, but we are not using those data here. The DB retrieval algorithm (Hsu et al., 2019) uses blue wavelength measurements where the surface reflectance over land tends to be much lower than at longer wavelengths, allowing for the retrieval of aerosol properties over both bright and dark surfaces. This is especially true over desert surfaces. Both MODIS DT and DB are reported at a nominal spatial resolution of 10 km at nadir. We use the recently reprocessed MODIS collection 6.1 (C6.1) products which employ (1) an updated radiometric calibration that improves instrument stability over time, (2) updates to the surface reflectance treatment used in the DT algorithm (Gupta et al., 2016), (3) improvement to the surface modelling in elevated terrain, (4) reduction in artifacts in heterogeneous terrain, and (5) improved internal smoke detection masks used in the DB algorithm (Hsu et al., 2019; Sayer et al., 2019).

The MAIAC algorithm (Lyapustin et al., 2018b) retrieves aerosol information over both bright and dark land surfaces simultaneously with surface bidirectional reflectance using time-series analysis of MODIS L1B radiance measurements for up to 16 days. With removal of the long-term calibration trends and cross-calibration of MODIS Terra to MODIS Aqua in Collection 6

(Lyapustin et al., 2014), MAIAC processes the two sensors jointly, which creates significantly increased observation frequency required for accurate surface characterization. MAIAC was officially released in May 2018, providing AOD at a fine spatial resolution of 1 km globally over the land and coastal ocean for the entire MODIS record. However, this work started earlier and used an internally released MAIAC dataset that lacked parts of Canada, eastern Siberia, and the large Indo-Pacific region (e.g., Indonesia, Oceania, Australia, New Zealand).

The SeaWiFS instrument flew on SeaStar, which had a noon overpass time, and was operational between 1997-2010. SeaWiFS maintained a highly accurate and stable calibration over its lifetime (Sayer et al., 2012). SeaWiFS provided measurements in eight spectral bands between 402-885 nm and had a 1500 km swath width that provided nearly daily global coverage. We used the version 4 SeaWiFS Deep Blue (Sayer et al., 2012; Hsu et al., 2013) data set that offers AOD with a horizontal pixel size of 13.5 km at nadir.

The MISR instrument is also onboard the Terra satellite and has been operational since 2000. MISR observes the earth at nine different viewing angles and four spectral bands (446, 558, 672, and 866 nm), with a swath width of 380 km all view angles that provides global coverage about once per week, every nine days at the equator, up to every two days near the poles (Diner et al., 1998). The MISR retrieval algorithm uses the same-scene multi-angular views provided by the nine view-angles to solve for surface and top-of-atmosphere reflectance contributions, providing AOD retrievals over bright and dark land surfaces without absolute surface reflectance assumptions (Martonchik et al., 2009). We use AOD retrieved from the recently released MISR v23 algorithm (Garay et al., 2017), which provides AOD at a spatial resolution of 4.4 km, which is a significant improvement over the 17.6 km resolution in the previous version of MISR AOD, along with better cloud screening and pixel-level uncertainty estimates.

4.7.2. Description of the GEOS-Chem simulation

We use v11-01 of the GEOS-Chem chemical transport model (http://geos-chem.org) to simulate η, and as an additional AOD source. The simulation is driven by assimilated meteorological data from the recent MERRA-2 Reanalysis of the NASA Global Modeling and Assimilation Office (GMAO), which offers a consistent assimilation from 1979, including updates in both the Goddard Earth Observing System Model and the assimilation system (Molod et al., 2015). Our simulation is conducted for the years 2000–2017 at a spatial resolution of $2^{\circ} \times 2.5^{\circ}$ with a nested resolution of

0.5° x 0.625° over North America, Europe, and China, and 47 vertical levels. The top of lowest model layer is approximately 100 m. We follow the recommendations of Philip et al. (2016) to use a chemical and transport operator duration of 20 min and 10 min, respectively. We include a non-local boundary layer mixing scheme (Lin and McElroy, 2010). We spin up the model for one month before each global and regional simulation to remove the effects of initial conditions.

GEOS-Chem contains a detailed oxidant-aerosol chemical mechanism (Bey et al., 2001; Park et al., 2004b). The aerosol simulation includes the sulfate–nitrate–ammonium system (Park et al., 2004b; Fountoukis and Nenes, 2007; Pye et al., 2009b), primary carbonaceous aerosol (Park et al., 2003), sea salt (Jaeglé et al., 2011), and mineral dust (Fairlie et al., 2007) with an improved fine dust size distribution(Zhang et al., 2013a). We include an anthropogenic fugitive, combustion, and industrial dust (AFCID) emissions inventory (Philip et al., 2017b). Semivolatile primary organic carbon and secondary organic aerosol (SOA) formation (Pye et al., 2010) is included with updated SOA formation from isoprene via an irreversible up-take scheme (Marais et al., 2016). HNO_3 concentrations are reduced to commensurate with prior work (Heald et al., 2012). Relative humidity dependent aerosol optical properties are based on the Global Aerosol Data Set (GADS) (Koepke et al., 1997; Martin et al., 2003) with updates for organics and secondary inorganics from aircraft observations (Drury et al., 2010), mineral dust (Lee et al., 2009; Ridley et al., 2012; Zhang et al., 2013a), and for absorbing brown carbon (Hammer et al., 2016).

The anthropogenic emissions inventories in our simulation are summarized in Table S4. Global anthropogenic emissions are from the EDGAR v4.3.1 global inventory (Crippa et al., 2016), with speciated volatile organic compound (VOC) emissions from RETRO (Schultz et al., n.d.). Emissions are over-written in areas with regional inventories, including the US (NEI11; Travis et al., 2016), Canada (CAC; http://www.ec.gc.ca/pdb/cac/), Mexico (BRAVO; Kuhns et al., 2005), Europe (EMEP; http://www.emep.int/), China (MEIC v1.2; Liu et al., 2016b), India (Lu et al., 2011) and elsewhere in Asia (MIX; Liu et al., 2016b). We doubled the Indian OC and BC emissions from Lu et al. (2011) based on Philip et al. (2014) and Fu et al. (2012). Emissions from open fires for individual years from the GFED4 inventory (Giglio et al., 2013b) are included covering the years 1998-2014.

4.7.3. Algorithm for calculating combined $PM_{2.5}$ from satellites and simulation

Our algorithm to combine information from satellites and simulation follows van Donkelaar et al. (2016), with updates to ground-based AOD measurements, to the satellite AOD products, to the GEOS-Chem simulation, and to the resolution of our analysis.

The first step in the calculation of our combined $PM_{2.5}$ estimates is the common calibration of the separate AOD sources. Each source is translated onto a common 0.05° x 0.05° grid. For a consistent definition of uncertainty, we compare each AOD source with AERONET (Aerosol Robotic Network) (Holben et al., 1998) AOD at 550 nm. AERONET is a global sun photometer network that provides multi-wavelength AOD measurements with a high level of accuracy (the uncertainty associated with AERONET measurements is <0.02). We use level 2 of the version 3 AERONET data (Giles et al., 2019).

There are different sources of error associated with satellite retrieved AOD than with simulated AOD, therefore their uncertainties need to be accounted for differently. For cloud-free and snow-free daytime scenes, one of the main sources of uncertainty associated with satellite retrieved AOD is the surface treatment used in the retrieval (Li et al., 2009). Therefore the daily satellite AOD retrievals are sampled to within 0.25° of each AERONET site and binned according to the Normalized Difference Vegetation Index (NDVI), which represents seasonally based changes in vegetation. Locally, calibrations are calculated at each AERONET site as the median slope and offset from reduced major axis linear regression of retrieved AOD with the AERONET values. The local calibrations are then expanded globally by calculating each pixel as the weighted average of all AERONET site-specific local calibrations, using inverse squared distance and the inverse of the Land Cover Similarity (LCS):

$$LCS_{i,j,k} = \sum_{n=1}^{N_{LT}} |LT_{i,j,n} - LT_{k,n}| \qquad [4\text{-S1}]$$

where $LT_{i,j,n}$ is the land cover type percentage of the pixel (i,j) for each land cover type (n) and $LT_{k,n}$ is the land cover type percentage of AERONET site (k) for each land cover type (n). The land cover type categories are defined by the MODIS land cover product (Friedl et al., 2010). The LCS allows similar mixtures of land cover to be weighted more strongly.

The residual uncertainty between the calibrated and observed AOD at each AERONET site is then calculated as the normalized root mean square difference:

$$NRMSD = \frac{\left(MEAN(AOD_{CALIBRATED} - AOD_{AERONET})^2\right)^{0.5}}{AOD_{AERONET}} \quad [4\text{-S2}]$$

Local NRMSD are globally extended using inverse squared distance and LCS, following the approach used for the local calibration factors.

For the simulated AOD, to account for errors due to species-specific emissions and assumed aerosol microphysical properties, we calculate the relative uncertainty by applying the simulated fractional aerosol composition to each daily AERONET observation following van Donkelaar et al. (2013). The local calibration factors are calculated as the absolute error of each species at each station as a function of magnitude. The local calibration factors are then extended globally using inverse distance squared and the cross-correlation weighted average of each AERONET site to each global pixel. The residual uncertainty is calculated as the component-specific NRMSD, and is extended globally using the inverse squared distance and cross correlation. The daily surface $PM_{2.5}$ concentrations from each source are obtained by applying the daily simulated AOD to $PM_{2.5}$ ratios (η).

The daily AOD and $PM_{2.5}$ values are used to calculate monthly mean values. Missing AOD and $PM_{2.5}$ values within areas of more than 50% coverage are approximated using the interpolated ratio with the same data source during other years, or if necessary the interpolated ratio with simulated values during the same time period. Monthly AOD values from all N sources are combined using a weighted average, weighted by the product of the inverse residual AOD NRMSD, the inverse absolute percent difference between calibrated and uncalibrated AOD $\left(\frac{\Delta AOD_{adj}}{AOD}\right)$ and the local data density (N_{obs}) such that:

$$AOD = \frac{\sum_{n=1}^{N} \frac{1}{NRMSD_n} \times \left(\frac{\Delta AOD_{adj,n}}{AOD_n}\right)^{-1} \times N_{obs,n}^2 \times AOD_n}{\sum_{n=1}^{N} \frac{1}{NRMSD_n} \times \left(\frac{\Delta AOD_{adj,n}}{AOD_n}\right)^{-1} \times N_{obs,n}^2} \quad [4\text{-S3}]$$

$\Delta AOD_{adj,n}$ and AOD_n are set to a minimum of 0.01, and N_{obs} is set to a maximum of 5 observations per month for the purpose of weighting, even when more observations are included in the calculation. The squaring of N_{obs} penalizes sparse observation density. Values exceeding 3 standard deviations of those within the surrounding 1° x 1° are replaced via linear interpolation.

The monthly $PM_{2.5}$ estimates are combined using similar weighting:

$$PM_{2.5} = \frac{\sum_{n=1}^{N} \frac{1}{NRMSD_n} \times \left(\frac{\Delta AOD_{adj,n}}{AOD_n}\right)^{-1} \times N_{obs,n}^2 \times PM_{2.5,n}}{\sum_{n=1}^{N} \frac{1}{NRMSD_n} \times \left(\frac{\Delta AOD_{adj,n}}{AOD_n}\right)^{-1} \times N_{obs,n}^2} \quad [4\text{-S4}]$$

Spatial information from the 1 km MAIAC AOD retrieval is then incorporated by applying the climatology of its retrieved relative variation between 0.01° and 0.05°. Where MAIAC is unavailable, monthly AOD and $PM_{2.5}$ are linearly interpolated onto a 0.01° x 0.01° grid.

We use Geographically Weighted Regression (GWR) to predict and account for the bias in the annual mean of our geophysical $PM_{2.5}$ estimates ($GEO\ PM_{2.5}$). GWR is a statistical technique that allows the modelling of processes that vary over space (Brunsdon et al., 2010). GWR is an extension of least-squares regression that allows predictor coefficients to vary spatially by weighting the estimate-observation pairs at multiple geographic locations according to their inverse squared distance from individual observation sites.

We fit our GWR model coefficients at 1° x 1° intervals using $PM_{2.5}$ measured with ground-based monitors ($GM\ PM_{2.5}$) following the form:

$$(GM\ PM_{2.5} - \ GEO\ PM_{2.5}) = \beta_1 DST + \beta_2 SNAOC + \beta_3 ED \times DU \quad [4\text{-S5}]$$

where

β_1 to β_3: represent spatially varying predictor coefficients,

ED: the log of the elevation difference between the local elevation and the mean elevation within the simulation grid cell according to the 1° x 1° ETOPO1 Global Relief Model (from the National Geophysical Data Center; http://www.ngdc.noaa.gov/mgg/global/seltopo.html),

DU: inverse distance to the nearest urban land surface based on the 1° resolution MODIS Land Cover Type Product (MCD12Q1) (Friedl et al., 2010),

DST and $SNAOC$: compositional concentrations of mineral dust (DST) and the sum of sulfate, nitrate, ammonium, and organic carbon ($SNAOC$) are represented by the simulated relative contributions of each species applied to $GEO\ PM_{2.5}$ by weighting the near-surface aerosol concentration by the simulated compositional contribution of each species (Philip et al., 2014).

We interpolate all predictors onto a common 0.01° grid.

Table 4-S1: Summary of anthropogenic emissions used in the GEOS-Chem simulation

Region	Inventory (Coverage)	Used Species	Annual Scale Factor[a]	Reference
World	EDGAR v4.3.1 (1970-2010)	CO, NO_x, SO_2, NH_3, OC, BC	N/A	Crippa et al. 2016
	RETRO (2000)	VOCs	from EDGAR v4.3.1, 1970-2010	Schultz et al., n.d.
U.S.	EPA NEI11 (2011)	CO, NO_x, SO_2, NH_3, OC, BC, VOCs	NEI historical emission, 1990-2014	US Environmental Protection Agency (Travis et al., 2016)
Canada	CAC (2002-2008)	CO, NO_x, SO_2, NH_3, OC, BC	APEI, 1990-2014	Environment Canada[b]
Mexico	BRAVO (1999)	CO, NO_x, SO_2	from EDGAR v4.3.1, 1970-2010	Kuhns et al., 2005
Europe	EMEP (1990-2012)	CO, NO_x, SO_2, NH_3	N/A	Centre on Emissions Inventories and Projections[c]
China	MEIC v1.2 (2000-2015)	NO_x, SO_2, NH_3, OC, BC	N/A	Li et al. 2017b
India	Lu et al.(Lu et al., 2011) (1998-2010)	SO_2, OC, BC	N/A	Lu et al. 2011
Asia	MIX (2008-2012)	CO, NO_x, SO_2, NH_3, OC, BC, VOCs	CO, NO_x, NH_3,VOCs, from EDGAR v4.3.1, 1970-2010, SO_2, OC, BC from Lu et al.(Lu et al., 2011)	Li et al. 2017b

a. Annual scale factors are spatially resolved and applied only when the emission inventory lacks data for a certain year. Data in the closest available year is used if outside the available range.

b. http://www.ec.gc.ca/pdb/cac/

c. http://www.emep.int/

Table 4-S2: The global number of direct $PM_{2.5}$ measurements available each year from the World Health Organization (WHO) Ambient (Outdoor) Air Quality Database.

Year	Number of measurements
2010	1591
2011	1655
2012	1739
2013	2045
2014	2673
2015	3744
2016	3541
2017	16

Table 4-S3: The agreement (R^2) between the hybrid geophysical-statistical $PM_{2.5}$ estimates (at cross validated sites) and in-situ values for V4.GL.03 (R^2_03) from this work and V4.GL.02 (R^2_02) from van Donkelaar et al. (2016). N is the number of comparison points.

Year	R^2_03	R^2_02	N
2010	0.72	0.76	1017
2011	0.74	0.73	1092
2012	0.74	0.74	1139
2013	0.68	0.70	1330
2014	0.90	0.81	1790
2015	0.91	0.87	2240
2016	0.90	0.84	2285

Table 4-S4: Population-weighted mean $PM_{2.5}$ ($\mu g/m^3$) by Global Burden of Disease (GBD) region according to geophysical (GEO), GWR-adjusted hybrid (HBR), and monitor for 2015.

				At $PM_{2.5}$ Monitor Locations			
Region	**Population [million people]**	**GEO $PM_{2.5}$**	**HBR $PM_{2.5}$**	**GEO $PM_{2.5}$**	**HBR $PM_{2.5}$**	**Monitor $PM_{2.5}$**	**N [#]**
Global	7345	43.7	45.1	44.3	43.8	44.5	3744
Asia Pacific, High Income	182	19.6	18.3	32.6	30.2	23.3	24
Asia Central	86	15.8	26.0	-	-	-	0
Asia East	1430	53.8	49.2	56.0	54.5	55.6	1453
Asia South	1721	56.0	62.8	62.3	75.0	79.8	13
Asia, Southeast	648	31.4	26.4	-	-	-	0
Australasia	28	3.0	5.0	2.9	5.6	7.4	35
Caribbean	39	7.4	9.3	-	-	-	0
Europe, Central	115	14.8	18.8	15.5	21.2	22.4	145
Europe, Eastern	209	12.4	13.6	4.4	5.3	9.7	48
Europe, Western	423	11.1	12.8	10.8	13.8	14.3	910
Latin America, Andean	57	12.2	22.5	10.0	54.0	25.0	1
Latin America, Central	251	15.1	15.7	24.7	23.6	24.6	17
Latin America, Southern	64	7.2	8.4	6.0	8.0	10.0	1
Latin America, Tropical	214	9.2	9.9	-	-	-	0
North Africa/Middle-East	488	23.0	26.9	44.4	55.6	72.4	3
North America, High Income	360	9.7	8.9	9.7	9.0	8.6	1068
Oceania	10	5.6	4.8	2	2	8	1
Sub-Saharan Africa, Central	113	30.5	30.4	-	-	-	0
Sub-Saharan Africa, East	416	17.3	18.4	-	-	-	0
Sub-Saharan Africa, Southern	78	11.5	11.5	-	-	-	0
Sub-Saharan Africa, West	391	55.4	72.5	-	-	-	0

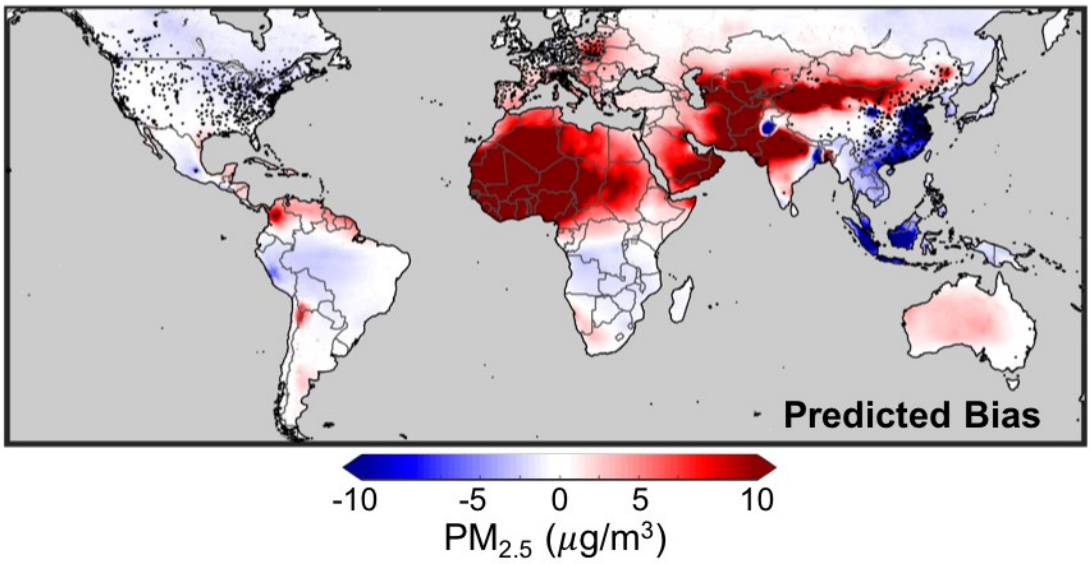

Figure 4-S1: Bias predicted by geographically weighted regression between our geophysical $PM_{2.5}$ estimates (Figure 4-3) and in situ ground monitor data for 2015. Point locations correspond to individual monitors, with black dots representing direct $PM_{2.5}$ observations. Grey denotes water.

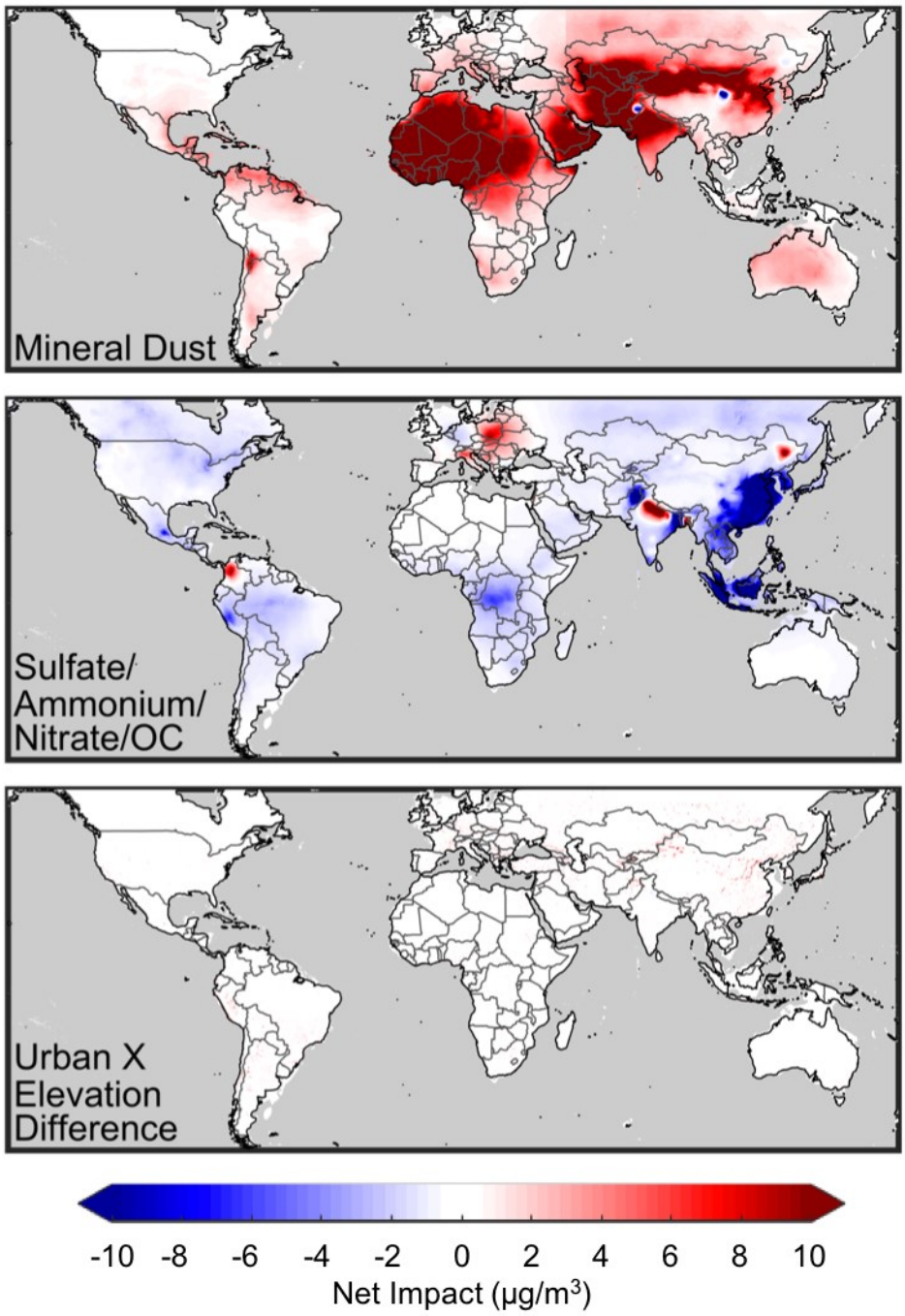

Figure 4-S2: Net impact of individual predictors on the geographically weighted regression estimate of bias in geophysical $PM_{2.5}$ for 2015. Gray denotes water.

Chapter 5: Conclusions

5.1 Summary

Atmospheric aerosols have significant impacts on climate and human health. Scattering and absorption by aerosols affects the global radiation budget. Absorption of ultraviolet (UV) radiation by aerosols also decreases photolysis frequencies, leading to a reduction in the concentrations of atmospheric oxidants. Exposure to aerosols with diameters less than 2.5 μm in diameter ($PM_{2.5}$) significantly impacts human health, causing cardiovascular and lung disease. However, the exact magnitude of the climate and health effects of aerosols remains highly uncertain, due to the large variability in aerosol physical and chemical properties. In this work, we used satellite observations of aerosol properties in conjunction with the global chemical transport model GEOS-Chem to improve our understanding of the interactions of aerosols with radiation and their impacts on health.

We interpreted OMI observations of the Ultraviolet Aerosol Index (UVAI), which provides a measure of absorbing aerosols, by developing a simulation of the UVAI using the vector radiative transfer model VLIDORT coupled with GEOS-Chem aerosol fields. Simulated and observed values are highly consistent in regions where mineral dust dominates the UVAI, but a large negative bias (−0.32 to −0.97) exists between simulated and observed values in biomass burning regions. We applied the OMI UVAI to estimate absorption by BrC. This approach exploits the strong absorption by BrC at ultraviolet wavelengths and its effect on top of atmosphere (TOA) radiance. The simulation including absorbing BrC is much more consistent than the base case at reproducing the OMI UVAI over biomass burning regions. The mean bias between simulated and OMI UVAI values is reduced from −0.57 to −0.09 over West Africa in January, from −0.32 to +0.0002 over South Asia in April, from −0.97 to −0.22 over southern Africa in July, and from −0.50 to +0.33 over South America in September.

We applied this constraint on ultraviolet absorption to examine implications for the O3 → $O(^1D)$ photolysis frequency $J(O(^1D))$. We find that the inclusion of absorbing BrC into GEOS-Chem decreased $J(O(^1D))$ and lower tropospheric OH by up to 30 % over South America in September, up to 20 % over southern Africa in July, up to 15% over West Africa in January and southern Africa in September, and up to 5 % elsewhere. The decrease in global mean OH

concentration in GEOS-Chem increased the methyl chloroform lifetime to tropospheric OH from 5.62 to 5.68 years, reducing the bias with estimates from observations of 6.0 (+0.5, −0.4) years.

We calculated the direct radiative effect (DRE) of BrC using GEOS-Chem coupled with the radiative transfer model RRTMG (GC-RT). We found that absorbing BrC changes the global annual mean all-sky top of atmosphere (TOA) DRE by +0.03 W m^{-2} and all-sky surface DRE by −0.08 W m^{-2}. Regional changes of up to +0.3 W m^{-2} at TOA and down to −1.5 W m^{-2} at the surface were found over major biomass burning regions.

We used our UVAI simulation to interpret trends in satellite observed UVAI values for 2005-2015 to improve our understanding of trends in global aerosol composition. Trends in absorption by mineral dust dominated the simulated UVAI trends over North Africa, the Middle East, East Asia, and Australia. The positive trends in the observed UVAI over Central Asia near the shrinking Aral Sea are likely due to increased dust emissions, a feature that is unlikely to be represented in most chemical transport models. Trends in absorption by BrC dominated the simulated UVAI trends over biomass burning regions. The UVAI simulation reproduced observed negative trends over central South America and West Africa, but underestimated observed UVAI trends over boreal forests. Trends in scattering by secondary inorganic aerosol dominated the simulated UVAI trends over the eastern United States and eastern India. This work demonstrated that trends in the observed UVAI offer valuable information on the evolution of global aerosol composition that can be understood through quantitative simulation of the UVAI.

We calculated geophysically based estimates of surface $PM_{2.5}$ concentrations using information from satellites, simulation, and ground monitors for the years 2000-2017. These combined $PM_{2.5}$ estimates benefited from recent updates to satellite AOD sources, developments in chemical transport models, and expanded ground monitor measurements. We found that MAIAC retrieved AOD becomes a large contributor to the combined AOD, with a mean weighting of 27%, due to its increased global availability and high performance over regions with difficult surface conditions, such as deserts. We found that our geophysical combined $PM_{2.5}$ estimates show excellent agreement with ground monitors (R^2=0.91), providing confidence in their use for regions with low monitor density.

We calculated the trends for 2000-2017 in our geophysical $PM_{2.5}$ values using Generalized Least Squares Regression. We find statistically significant positive trends over India, the Middle-

East, central and southern Africa, Canada, north western China, a small portion of east China, and parts of East Asia. The lack of statistically significant trends over East Asia is driven by a reversal in the slope of the trends after ~2012 when the slope turns negative. There are statistically significant negative trends over the eastern United States, Europe, Australia, and central South America. Statistical fusion explained an additional 10% of the variance in the $PM_{2.5}$ estimates, yielding an improved agreement (R^2=0.91) with cross-validated ground monitor sites. The populations of North America, Europe, and recently China experienced negative trends in $PM_{2.5}$, while large amounts of the global population experienced positive trends in $PM_{2.5}$ values, particularly in India.

5.2 Looking Forward

Chapters 2 and 3 of this work demonstrate that simulation of the UVAI allows for the derivation of independent aerosol composition information from satellite observations of ultraviolet radiances. The availability of UVAI observations from 1979 to the present offers a unique opportunity to understand long-term trends in aerosol absorption. Ample opportunities exist to further develop the simulation of the UVAI. The recent launch of the TROPOspheric Monitoring Instrument (TROPOMI; Veefkind et al., 2012) and the forthcoming geostationary constellation offer UVAI observations at finer spatial and temporal resolution, as well as information on diurnal variation, both of which may offer additional constraints on the evolution of aerosol species. The forthcoming Multi-Angle Imager for Aerosols (MAIA; Diner et al., 2018) satellite instrument offers an exciting opportunity to derive even more information about aerosol composition by combining measurements at ultraviolet wavelengths with multi-angle observations and polarization sensitivity.

Further investigation of the positive trend in satellite UVAI over central Asia that is not captured by simulation is required. This feature appears to be linked to the dessicating Aral Sea, which is possibly creating an increasingly important dust source, or a trend in surface reflectance. The negative trend in satellite UVAI values over Inner Mongolia that is not captured by simulation also requires further investigation.

There are several opportunities for improving the simulation of brown carbon. These opportunities include explicitly accounting for the range of processes affecting BrC such as regional treatment, burn conditions, and photochemical loss. The absorption by BrC produced

from secondary organic aerosol remains highly uncertain, and observational studies of industrial organic aerosol are necessary to quantify the optical properties of brown SOA.

Further developments in satellite retrieved AOD and chemical transport models are crucial for future $PM_{2.5}$ estimates. Using a hybrid geophysical-statistical approach for estimating $PM_{2.5}$ further improves the agreement with ground measurements. Future $PM_{2.5}$ estimates would benefit from increased monitor density, especially in regions such as Africa, the Middle-East, and South America. Future possible improvements to the simulated $PM_{2.5}$/AOD relationship include improvements to the representation of hygroscopic growth for organic and inorganic aerosols suggested by Latimer and Martin (2018), and improvements to the dust emissions scheme such as those suggested by Ridley et al. (2016). Inclusion of additional satellite sources should be explored, such as that from the Visible Infrared Radiometer Suite (VIIRS). Alternative statistical frameworks for the inclusion of ground monitor data could also be explored, such as deep learning or a Bayesian Hierarchical Framework similar to that used by Shaddick et al. (2018).

References

Adams, P. J., Seinfeld, J. H. and Koch, D. M.: Global concentrations of tropospheric sulfate, nitrate, and ammonium aerosol simulated in a general circulation model, J. Geophys. Res. Atmos., 104(D11), 13791–13823, doi:10.1029/1999JD900083, 1999.

Andela, N. and van der Werf, G. R.: Recent trends in African fires driven by cropland expansion and El Niño to La Niña transition, Nat. Clim. Chang., 4(9), 791–795, doi:10.1038/nclimate2313, 2014.

Andreae, M. O. and Gelencsér, a.: Black carbon or brown carbon? The nature of light-absorbing carbonaceous aerosols, Atmos. Chem. Phys. Discuss., 6(3), 3419–3463, doi:10.5194/acpd-6-3419-2006, 2006a.

Andreae, M. O. and Gelencsér, A.: Black carbon or brown carbon? The nature of light-absorbing carbonaceous aerosols, Atmos. Chem. Phys., 6(10), 3131–3148, doi:10.5194/acp-6-3131-2006, 2006b.

Apte, J. S., Marshall, J. D., Cohen, A. J. and Brauer, M.: Addressing Global Mortality from Ambient PM $_{2.5}$, Environ. Sci. Technol., 49(13), 8057–8066, doi:10.1021/acs.est.5b01236, 2015.

Arola, A., Schuster, G., Myhre, G., Kazadzis, S., Dey, S. and Tripathi, S. N.: Inferring absorbing organic carbon content from AERONET data, Atmos. Chem. Phys., 11(1), 215–225, doi:10.5194/acp-11-215-2011, 2011.

Arola, A., Schuster, G. L., Pitkänen, M. R. A., Dubovik, O., Kokkola, H., Lindfors, A. V., Mielonen, T., Raatikainen, T., Romakkaniemi, S., Tripathi, S. N. and Lihavainen, H.: Measurement-based direct radiative effect by brown carbon over Indo-Gangetic Plain, Atmos. Chem. Phys. Discuss., 15(15), 21583–21606, doi:10.5194/acpd-15-21583-2015, 2015.

Ayash, T., Gong, S., Jia, C. Q., Ayash, T., Gong, S. and Jia, C. Q.: Direct and Indirect Shortwave Radiative Effects of Sea Salt Aerosols, J. Clim., 21(13), 3207–3220, doi:10.1175/2007JCLI2063.1, 2008.

Badarinath, K. V. S., Kharol, S. K., Kaskaoutis, D. G., Sharma, A. R., Ramaswamy, V. and Kambezidis, H. D.: Long-range transport of dust aerosols over the Arabian Sea and Indian region — A case study using satellite data and ground-based measurements, Glob. Planet. Change, 72(3), 164–181, doi:10.1016/j.gloplacha.2010.02.003, 2010.

Bergstrom, R. W., Russell, P. B., Hignett, P., Bergstrom, R. W., Russell, P. B. and Hignett, P.: Wavelength Dependence of the Absorption of Black Carbon Particles: Predictions and Results from the TARFOX Experiment and Implications for the Aerosol Single Scattering Albedo, J. Atmos. Sci., 59(3), 567–577, doi:10.1175/1520-0469(2002)059<0567:WDOTAO>2.0.CO;2, 2002a.

Bergstrom, R. W., Russell, P. B. and Hignett, P.: Wavelength Dependence of the Absorption of Black Carbon Particles: Predictions and Results from the TARFOX Experiment and Implications for the Aerosol Single Scattering Albedo, J. Atmos. Sci., 59(3), 567–577, doi:10.1175/1520-0469(2002)059<0567:WDOTAO>2.0.CO;2, 2002b.

Bergstrom, R. W., Pilewskie, P., Russell, P. B., Redemann, J., Bond, T. C., Quinn, P. K. and Sierau, B.: Spectral absorption properties of atmospheric aerosols, Atmos. Chem. Phys., 7(23), 5937–5943, doi:10.5194/acp-7-5937-2007, 2007.

Bey, I., Jacob, D. J., Yantosca, R. M., Logan, J. A., Field, B. D., Fiore, A. M., Li, Q., Liu, H. Y., Mickley, L. J. and Schultz, M. G.: Global modeling of tropospheric chemistry with assimilated meteorology: Model description and evaluation, J. Geophys. Res., 106(D19), 23073, doi:10.1029/2001JD000807, 2001.

Bond, T. C.: Spectral dependence of visible light absorption by carbonaceous particles emitted from coal combustion, Geophys. Res. Lett., 28(21), 4075–4078, doi:10.1029/2001GL013652, 2001.

Bond, T. C. and Bergstrom, R. W.: Light Absorption by Carbonaceous Particles: An Investigative Review, Aerosol Sci. Technol., 40(1), 27–67, doi:10.1080/02786820500421521, 2006.

Bond, T. C., Bhardwaj, E., Dong, R., Jogani, R., Jung, S., Roden, C., Streets, D. G. and Trautmann, N. M.: Historical emissions of black and organic carbon aerosol from energy-related combustion, 1850-2000, Global Biogeochem. Cycles, 21(2), GB2018, doi:10.1029/2006GB002840, 2007.

Bond, T. C., Doherty, S. J., Fahey, D. W., Forster, P. M., Berntsen, T., DeAngelo, B. J., Flanner, M. G., Ghan, S., Kärcher, B., Koch, D., Kinne, S., Kondo, Y., Quinn, P. K., Sarofim, M. C., Schultz, M. G., Schulz, M., Venkataraman, C., Zhang, H., Zhang, S., Bellouin, N., Guttikunda, S. K., Hopke, P. K., Jacobson, M. Z., Kaiser, J. W., Klimont, Z., Lohmann, U., Schwarz, J. P., Shindell, D., Storelvmo, T., Warren, S. G. and Zender, C. S.: Bounding the role of black carbon in the climate system: A scientific assessment, J. Geophys. Res. Atmos., 118(11), 5380–5552, doi:10.1002/jgrd.50171, 2013.

Boys, B. L., Martin, R. V., van Donkelaar, A., MacDonell, R. J., Hsu, N. C., Cooper, M. J., Yantosca, R. M., Lu, Z., Streets, D. G., Zhang, Q. and Wang, S. W.: Fifteen-Year Global Time Series of Satellite-Derived Fine Particulate Matter, Environ. Sci. Technol., 48(19), 11109–11118, doi:10.1021/es502113p, 2014.

Brasseur, G. P. and Jacob, D. J.: Modeling of Atmospheric Chemistry, Cambridge University Press, Cambridge., 2017.

Brunsdon, C., Fotheringham, A. S. and Charlton, M. E.: Geographically Weighted Regression: A Method for Exploring Spatial Nonstationarity, Geogr. Anal., 28(4), 281–298, doi:10.1111/j.1538-4632.1996.tb00936.x, 2010.

Buchard, V., da Silva, A. M., Colarco, P. R., Darmenov, A., Randles, C. A., Govindaraju, R., Torres, O., Campbell, J. and Spurr, R.: Using the OMI aerosol index and absorption aerosol optical depth to evaluate the NASA MERRA Aerosol Reanalysis, Atmos. Chem. Phys., 15(10), 5743–5760, doi:10.5194/acp-15-5743-2015, 2015.

Canagaratna, M. R., Jimenez, J. L., Kroll, J. H., Chen, Q., Kessler, S. H., Massoli, P., Hildebrandt Ruiz, L., Fortner, E., Williams, L. R., Wilson, K. R., Surratt, J. D., Donahue, N. M., Jayne, J. T. and Worsnop, D. R.: Elemental ratio measurements of organic compounds using aerosol mass spectrometry: characterization, improved calibration, and implications, Atmos. Chem. Phys., 15(1), 253–272, doi:10.5194/acp-15-253-2015, 2015.

Chen, Y. and Bond, T. C.: Light absorption by organic carbon from wood combustion, Atmos. Chem. Phys., 10(4), 1773–1787, doi:10.5194/acp-10-1773-2010, 2010.

Chen, Y., Morton, D. C., Jin, Y., Collatz, G. J., Kasibhatla, P. S., van der Werf, G. R., DeFries, R. S. and Randerson, J. T.: Long-term trends and interannual variability of forest, savanna and agricultural fires in South America, Carbon Manag., 4(6), 617–638, doi:10.4155/cmt.13.61, 2013.

Chin, M., Diehl, T., Tan, Q., Prospero, J. M., Kahn, R. A., Remer, L. A., Yu, H., Sayer, A. M., Bian, H., Geogdzhayev, I. V., Holben, B. N., Howell, S. G., Huebert, B. J., Hsu, N. C., Kim, D., Kucsera, T. L., Levy, R. C., Mishchenko, M. I., Pan, X., Quinn, P. K., Schuster, G. L., Streets, D. G., Strode, S. A., Torres, O. and Zhao, X.-P.: Multi-decadal aerosol variations from 1980 to 2009: a perspective from observations and a global model, Atmos. Chem. Phys., 14(7), 3657–3690, doi:10.5194/acp-14-3657-2014, 2014.

Chung, C. E., Ramanathan, V. and Decremer, D.: Observationally constrained estimates of carbonaceous aerosol radiative forcing., Proc. Natl. Acad. Sci. U. S. A., 109(29), 11624–9, doi:10.1073/pnas.1203707109, 2012.

Clarke, A., McNaughton, C., Kapustin, V., Shinozuka, Y., Howell, S., Dibb, J., Zhou, J., Anderson, B. E., Brekhovskikh, V., Turner, H. and Pinkerton, M.: Biomass burning and pollution aerosol over North America: Organic components and their influence on spectral optical properties and humidification response, J. Geophys. Res. Atmos., 112(12), 1–13, doi:10.1029/2006JD007777, 2007.

Colarco, P. R., Toon, O. B., Torres, O. and Rasch, P. J.: Determining the UV imaginary index of refraction of Saharan dust particles from Total Ozone Mapping Spectrometer data using a three-dimensional model of dust transport, J. Geophys. Res., 107(D16), 4289, doi:10.1029/2001JD000903, 2002.

Corr, C. A., Hall, S. R., Ullmann, K., Anderson, B. E., Beyersdorf, A. J., Thornhill, K. L., Cubison, M. J., Jimenez, J. L., Wisthaler, A. and Dibb, J. E.: Spectral absorption of biomass burning aerosol determined from retrieved single scattering albedo during ARCTAS, Atmos. Chem. Phys., 12(21), 10505–10518, doi:10.5194/acp-12-10505-2012, 2012.

Crippa, M., Janssens-Maenhout, G., Dentener, F., Guizzardi, D., Sindelarova, K., Muntean, M., Van Dingenen, R. and Granier, C.: Forty years of improvements in European air quality: regional policy-industry interactions with global impacts, Atmos. Chem. Phys., 16(6), 3825–3841, doi:10.5194/acp-16-3825-2016, 2016.

Cui, H., Mao, P., Zhao, Y., Nielsen, C. P. and Zhang, J.: Patterns in atmospheric carbonaceous aerosols in China: emission estimates and observed concentrations, Atmos. Chem. Phys., 15(15), 8657–8678, doi:10.5194/acp-15-8657-2015, 2015.

Curci, G., Hogrefe, C., Bianconi, R., Im, U., Balzarini, A., Baró, R., Brunner, D., Forkel, R., Giordano, L., Hirtl, M., Honzak, L., Jiménez-Guerrero, P., Knote, C., Langer, M., Makar, P. A., Pirovano, G., Pérez, J. L., San José, R., Syrakov, D., Tuccella, P., Werhahn, J., Wolke, R., Žabkar, R., Zhang, J. and Galmarini, S.: Uncertainties of simulated aerosol optical properties induced by assumptions on aerosol physical and chemical properties: An AQMEII-2 perspective, Atmos. Environ., 115, 541–552, doi:10.1016/j.atmosenv.2014.09.009, 2015.

Curier, L., Kranenburg, R., Timmermans, R., Segers, A., Eskes, H. and Schaap, M.: Synergistic Use of LOTOS-EUROS and NO2 Tropospheric Columns to Evaluate the NOX Emission Trends Over Europe, pp. 239–245., 2014.

Dai, A.: Recent Climatology, Variability, and Trends in Global Surface Humidity, J. Clim., 19(15), 3589–3606, doi:10.1175/JCLI3816.1, 2006.

Dave, J. V: Effect of Aerosols on the Estimation of Total Ozone in an Atmospheric Column from the Measurements of Its Ultraviolet Radiance, J. Atmos. Sci., 35(5), 899–911, doi:10.1175/1520-0469(1978)035<0899:EOAOTE>2.0.CO;2, 1978.

Deirmendjian, D.: Scattering and Polarization Properties of Water Clouds and Hazes in the Visible and Infrared, Appl. Opt., 3(2), 187, doi:10.1364/AO.3.000187, 1964.

Deng, X., Tie, X., Zhou, X., Wu, D., Zhong, L., Tan, H., Li, F., Huang, X., Bi, X. and Deng, T.: Effects of Southeast Asia biomass burning on aerosols and ozone concentrations over the Pearl River Delta (PRD) region, Atmos. Environ., 42(36), 8493–8501, doi:10.1016/J.ATMOSENV.2008.08.013, 2008.

Dey, S. and Di Girolamo, L.: A decade of change in aerosol properties over the Indian subcontinent, Geophys. Res. Lett., 38(14), n/a-n/a, doi:10.1029/2011GL048153, 2011.

Di, Q., Koutrakis, P. and Schwartz, J.: A hybrid prediction model for PM2.5 mass and components using a chemical transport model and land use regression, Atmos. Environ., 131, 390–399, doi:10.1016/J.ATMOSENV.2016.02.002, 2016.

Dickerson, R. R., Kondragunta, S., Stenchikov, G., Civerolo, K. L., Doddridge, B. G. and Holben, B. N.: The impact of aerosols on solar ultraviolet radiation and photochemical smog., Science, 278(5339), 827–830, doi:10.1126/science.278.5339.827, 1997.

Diner, D. J., Beckert, J. C., Reilly, T. H., Bruegge, C. J., Conel, J. E., Kahn, R. A., Martonchik, J. V., Ackerman, T. P., Davies, R., Gerstl, S. A. W., Gordon, H. R., Muller, J., Myneni, R. B., Sellers, P. J., Pinty, B. and Verstraete, M. M.: Multi-angle Imaging SpectroRadiometer (MISR) instrument description and experiment overview, IEEE Trans. Geosci. Remote Sens., 36(4), 1072–1087, doi:10.1109/36.700992, 1998.

Diner, D. J., Boland, S. W., Brauer, M., Bruegge, C., Burke, K. A., Chipman, R., Di Girolamo, L., Garay, M. J., Hasheminassab, S., Hyer, E., Jerrett, M., Jovanovic, V., Kalashnikova, O. V., Liu, Y., Lyapustin, A. I., Martin, R. V., Nastan, A., Ostro, B. D., Ritz, B., Schwartz, J., Wang, J. and Xu, F.: Advances in multiangle satellite remote sensing of speciated airborne particulate matter and association with adverse health effects: from MISR to MAIA, J. Appl. Remote Sens., 12(04), 1, doi:10.1117/1.JRS.12.042603, 2018.

van Donkelaar, A., Martin, R. V., Leaitch, W. R., Macdonald, A. M., Walker, T. W., Streets, D. G., Zhang, Q., Dunlea, E. J., Jimenez, J. L., Dibb, J. E., Huey, L. G., Weber, R. and Andreae, M. O.: Analysis of aircraft and satellite measurements from the Intercontinental Chemical Transport Experiment (INTEX-B) to quantify long-range transport of East Asian sulfur to Canada, Atmos. Chem. Phys., 8(11), 2999–3014, doi:10.5194/acp-8-2999-2008, 2008.

van Donkelaar, A., Martin, R. V., Brauer, M., Kahn, R., Levy, R., Verduzco, C. and Villeneuve, P. J.: Global Estimates of Ambient Fine Particulate Matter Concentrations from Satellite-Based Aerosol Optical Depth: Development and Application, Environ. Health Perspect., 118(6), 847–855, doi:10.1289/ehp.0901623, 2010.

van Donkelaar, A., Martin, R. V., Spurr, R. J. D., Drury, E., Remer, L. A., Levy, R. C. and Wang, J.: Optimal estimation for global ground-level fine particulate matter concentrations, J. Geophys. Res. Atmos., 118(11), 5621–5636, doi:10.1002/jgrd.50479, 2013.

van Donkelaar, A., Martin, R. V., Brauer, M. and Boys, B. L.: Use of Satellite Observations for Long-Term Exposure Assessment of Global Concentrations of Fine Particulate Matter, Environ. Health Perspect., 123(2), 135–143, doi:10.1289/ehp.1408646, 2015.

van Donkelaar, A., Martin, R. V., Brauer, M., Hsu, N. C., Kahn, R. A., Levy, R. C., Lyapustin, A., Sayer, A. M. and Winker, D. M.: Global Estimates of Fine Particulate Matter using a Combined Geophysical-Statistical Method with Information from Satellites, Models, and Monitors, Environ. Sci. Technol., 50(7), 3762–3772, doi:10.1021/acs.est.5b05833, 2016.

van Donkelaar, A., Martin, R. V and Park, R. J.: Estimating ground-level PM 2.5 using aerosol optical depth determined from satellite remote sensing, J. Geophys. Res, 111, 21201, doi:10.1029/2005JD006996, 2006.

Drury, E., Jacob, D. J., Spurr, R. J. D., Wang, J., Shinozuka, Y., Anderson, B. E., Clarke, A. D., Dibb, J., McNaughton, C. and Weber, R.: Synthesis of satellite (MODIS), aircraft (ICARTT), and surface (IMPROVE, EPA-AQS, AERONET) aerosol observations over eastern North America to improve MODIS aerosol retrievals and constrain surface aerosol concentrations and sources, J. Geophys. Res., 115(D14), D14204, doi:10.1029/2009JD012629, 2010.

Duncan, B. N., Martin, R. V., Staudt, A. C., Yevich, R. and Logan, J. A.: Interannual and seasonal variability of biomass burning emissions constrained by satellite observations, J. Geophys. Res., 108(D2), 4100, doi:10.1029/2002JD002378, 2003.

Duncan Fairlie, T., Jacob, D. J. and Park, R. J.: The impact of transpacific transport of mineral dust in the United States, Atmos. Environ., 41(6), 1251–1266, doi:10.1016/J.ATMOSENV.2006.09.048, 2007.

Duplissy, J., DeCarlo, P. F., Dommen, J., Alfarra, M. R., Metzger, A., Barmpadimos, I., Prevot, A. S. H., Weingartner, E., Tritscher, T., Gysel, M., Aiken, A. C., Jimenez, J. L., Canagaratna, M. R., Worsnop, D. R., Collins, D. R., Tomlinson, J. and Baltensperger, U.: Relating hygroscopicity and composition of organic aerosol particulate matter, Atmos. Chem. Phys., 11(3), 1155–1165, doi:10.5194/acp-11-1155-2011, 2011.

Eck, T. F., Holben, B. N., Reid, J. S., Dubovik, O., Smirnov, A., O'Neill, N. T., Slutsker, I. and Kinne, S.: Wavelength dependence of the optical depth of biomass burning, urban, and desert dust aerosols, J. Geophys. Res. Atmos., 104(D24), 31333–31349, doi:10.1029/1999JD900923, 1999.

Fairlie, D. J., Jacob, D. J. and Park, R. J.: The impact of transpacific transport of mineral dust in the United States, Atmos. Environ., 41(6), 1251–1266, doi:10.1016/j.atmosenv.2006.09.048, 2007.

Feng, Y., Ramanathan, V. and Kotamarthi, V. R.: Brown carbon: A significant atmospheric absorber of solar radiation, Atmos. Chem. Phys., 13(17), 8607–8621, doi:10.5194/acp-13-8607-2013, 2013.

Fioletov, V. E., McLinden, C. A., Krotkov, N., Li, C., Joiner, J., Theys, N., Carn, S. and Moran, M. D.: A global catalogue of large SO2 sources and emissions derived from the Ozone Monitoring Instrument, Atmos. Chem. Phys., 16(18), 11497–11519, doi:10.5194/acp-16-11497-2016, 2016.

Flores, J. M., Washenfelder, R. A., Adler, G., Lee, H. J., Segev, L., Laskin, J., Laskin, A., Nizkorodov, S. A., Brown, S. S. and Rudich, Y.: Complex refractive indices in the near-ultraviolet spectral region of biogenic secondary organic aerosol aged with ammonia., Phys. Chem. Chem. Phys., 16(22), 10629–42, doi:10.1039/c4cp01009d, 2014.

Forrister, H., Liu, J., Scheuer, E., Dibb, J., Ziemba, L., Thornhill, K. L., Anderson, B., Diskin, G., Perring, A. E., Schwarz, J. P., Campuzano-Jost, P., Day, D. A., Palm, B. B., Jimenez, J. L., Nenes, A. and Weber, R. J.: Evolution of brown carbon in wildfire plumes, Geophys. Res. Lett., 42(11), 4623–4630, doi:10.1002/2015GL063897, 2015.

Fotheringham, A. S., Charlton, M. E. and Brunsdon, C.: Geographically Weighted Regression: A Natural Evolution of the Expansion Method for Spatial Data Analysis, Environ. Plan. A Econ. Sp., 30(11), 1905–1927, doi:10.1068/a301905, 1998.

Fountoukis, C. and Nenes, A.: ISORROPIA II: a computationally efficient thermodynamic equilibrium model for K^+–Ca^{2+}–Mg^{2+}–NH_4^+–Na^+–SO_4^{2-}–NO_3^-–Cl^-–H_2O aero, Atmos. Chem. Phys., 7(17), 4639–4659, doi:10.5194/acp-7-4639-2007, 2007.

Franklin, M., Kalashnikova, O. V. and Garay, M. J.: Size-resolved particulate matter concentrations derived from 4.4 km-resolution size-fractionated Multi-angle Imaging SpectroRadiometer (MISR) aerosol optical depth over Southern California, Remote Sens. Environ., 196, 312–323, doi:10.1016/J.RSE.2017.05.002, 2017.

Friberg, M. D., Kahn, R. A., Holmes, H. A., Chang, H. H., Sarnat, S. E., Tolbert, P. E., Russell, A. G. and Mulholland, J. A.: Daily ambient air pollution metrics for five cities: Evaluation of data-fusion-based estimates and uncertainties, Atmos. Environ., 158, 36–50, doi:10.1016/J.ATMOSENV.2017.03.022, 2017.

Friedl, M. A., Sulla-Menashe, D., Tan, B., Schneider, A., Ramankutty, N., Sibley, A. and Huang, X.: MODIS Collection 5 global land cover: Algorithm refinements and characterization of new datasets, Remote Sens. Environ., 114(1), 168–182, doi:10.1016/J.RSE.2009.08.016, 2010.

Fu, T.-M., Cao, J. J., Zhang, X. Y., Lee, S. C., Zhang, Q., Han, Y. M., Qu, W. J., Han, Z., Zhang, R., Wang, Y. X., Chen, D. and Henze, D. K.: Carbonaceous aerosols in China: top-down constraints on primary sources and estimation of secondary contribution, Atmos. Chem. Phys., 12(5), 2725–2746, doi:10.5194/acp-12-2725-2012, 2012.

Garay, M.J.; Witek, M.L.; Kahn, R.A.; Seidel, F.C.; Limbacher, J.A; Bull, M.A.; Diner, D.J.; Hansen, E.G.; Kalashnikova, O.V.; Lee, H.; Nastan, A.M.; and Yu, Y.: Introducing the 4.4 km Spatial Resolution MISR Aerosol Products., Atmos. Meas. Tech., (In preparation)., n.d.

Garay, M. J., Kalashnikova, O. V. and Bull, M. A.: Development and assessment of a higher-spatial-resolution (4.4 km) MISR aerosol optical depth product using AERONET-DRAGON data, Atmos. Chem. Phys., 17(8), 5095–5106, doi:10.5194/acp-17-5095-2017, 2017.

GBD 2016 Risk Factors Collaborators, E., Afshin, A., Abajobir, A. A., Abate, K. H., Abbafati, C., Abbas, K. M., Abd-Allah, F., Abdulle, A. M., Abera, S. F., Aboyans, V., Abu-Raddad, L. J., Abu-Rmeileh, N. M. E., Abyu, G. Y., Adedeji, I. A., Adetokunboh, O., Afarideh, M., Agrawal, A., Agrawal, S., Ahmadieh, H., Ahmed, M. B., Aichour, M. T. E., Aichour, A. N., Aichour, I., Akinyemi, R. O., Akseer, N., Alahdab, F., Al-Aly, Z., Alam, K., Alam, N., Alam, T., Alasfoor, D., Alene, K. A., Ali, K., Alizadeh-Navaei, R., Alkerwi, A., Alla, F., Allebeck, P., Al-Raddadi, R., Alsharif, U., Altirkawi, K. A., Alvis-Guzman, N., Amare, A. T., Amini, E., Ammar, W., Amoako, Y. A., Ansari, H., Antó, J. M., Antonio, C. A. T., Anwari, P., Arian, N., Ärnlöv, J., Artaman, A., Aryal, K. K., Asayesh, H., Asgedom, S. W., Atey, T. M., Avila-Burgos, L., Avokpaho, E. F. G. A., Awasthi, A., Azzopardi, P., Bacha, U., Badawi, A., Balakrishnan, K., Ballew, S. H., Barac, A., Barber, R. M., Barker-Collo, S. L., Bärnighausen, T., Barquera, S., Barregard, L., Barrero, L. H., Batis, C., Battle, K. E., Baumgarner, B. R., Baune, B. T., Beardsley, J., Bedi, N., Beghi, E., Bell, M. L., Bennett, D. A., Bennett, J. R., Bensenor, I. M., Berhane, A., Berhe, D. F., Bernabé, E., Betsu, B. D., Beuran, M., Beyene, A. S., Bhansali, A., Bhutta, Z. A., Bicer, B. K., Bikbov, B., Birungi, C., Biryukov, S., Blosser, C. D., Boneya, D. J., Bou-Orm, I. R., Brauer, M., Breitborde, N. J. K., et al.: Global, regional, and national comparative risk assessment of 84 behavioural, environmental and occupational, and metabolic risks or clusters of risks, 1990-2016: a systematic analysis for the Global Burden of Disease Study 2016., Lancet (London, England), 390(10100), 1345–1422, doi:10.1016/S0140-6736(17)32366-8, 2017.

Gelaro, R., McCarty, W., Suárez, M. J., Todling, R., Molod, A., Takacs, L., Randles, C. A., Darmenov, A., Bosilovich, M. G., Reichle, R., Wargan, K., Coy, L., Cullather, R., Draper, C., Akella, S., Buchard, V., Conaty, A., da Silva, A. M., Gu, W., Kim, G.-K., Koster, R., Lucchesi, R., Merkova, D., Nielsen, J. E., Partyka, G., Pawson, S., Putman, W., Rienecker, M., Schubert, S. D., Sienkiewicz, M., Zhao, B., Gelaro, R., McCarty, W., Suárez, M. J., Todling, R., Molod, A., Takacs, L., Randles, C. A., Darmenov, A., Bosilovich, M. G., Reichle, R., Wargan, K., Coy, L., Cullather, R., Draper, C., Akella, S., Buchard, V., Conaty, A., Silva, A. M. da, Gu, W., Kim, G.-K., Koster, R., Lucchesi, R., Merkova, D., Nielsen, J. E., Partyka, G., Pawson, S., Putman, W., Rienecker, M., Schubert, S. D., Sienkiewicz, M. and Zhao, B.: The Modern-Era Retrospective Analysis for Research and Applications, Version 2 (MERRA-2), J. Clim., 30(14), 5419–5454, doi:10.1175/JCLI-D-16-0758.1, 2017.

Giglio, L., Randerson, J. T. and van der Werf, G. R.: Analysis of daily, monthly, and annual burned area using the fourth-generation global fire emissions database (GFED4), J. Geophys. Res. Biogeosciences, 118(1), 317–328, doi:10.1002/jgrg.20042, 2013a.

Giglio, L., Randerson, J. T. and van der Werf, G. R.: Analysis of daily, monthly, and annual burned area using the fourth-generation global fire emissions database (GFED4), J. Geophys. Res. Biogeosciences, 118(1), 317–328, doi:10.1002/jgrg.20042, 2013b.

Giles, D. M., Sinyuk, A., Sorokin, M. G., Schafer, J. S., Smirnov, A., Slutsker, I., Eck, T. F., Holben, B. N., Lewis, J. R., Campbell, J. R., Welton, E. J., Korkin, S. V. and Lyapustin, A. I.: Advancements in the Aerosol Robotic Network (AERONET) Version 3 database – automated near-real-time quality control algorithm with improved cloud screening for Sun photometer aerosol optical depth (AOD) measurements, Atmos. Meas. Tech., 12(1), 169–209, doi:10.5194/amt-12-169-2019, 2019.

Ginoux, P., Prospero, J. M., Gill, T. E., Hsu, N. C. and Zhao, M.: Global-scale attribution of anthropogenic and natural dust sources and their emission rates based on MODIS Deep Blue aerosol products, Rev. Geophys., 50(3), doi:10.1029/2012RG000388, 2012.

de Graaf, M., Stammes, P., Torres, O. and Koelemeijer, R. B. A.: Absorbing Aerosol Index: Sensitivity analysis, application to GOME and comparison with TOMS, J. Geophys. Res., 110(D1), D01201, doi:10.1029/2004JD005178, 2005.

Guan, H., Esswein, R., Lopez, J., Bergstrom, R., Warnock, A., Follette-Cook, M., Fromm, M. and Iraci, L. T.: A multi-decadal history of biomass burning plume heights identified using aerosol index measurements, Atmos. Chem. Phys., 10(14), 6461–6469, doi:10.5194/acp-10-6461-2010, 2010.

Guan, Q., Sun, X., Yang, J., Pan, B., Zhao, S., Wang, L., Guan, Q., Sun, X., Yang, J., Pan, B., Zhao, S. and Wang, L.: Dust Storms in Northern China: Long-Term Spatiotemporal Characteristics and Climate Controls, J. Clim., 30(17), 6683–6700, doi:10.1175/JCLI-D-16-0795.1, 2017.

Guan, X., Huang, J., Zhang, Y., Xie, Y. and Liu, J.: The relationship between anthropogenic dust and population over global semi-arid regions, Atmos. Chem. Phys., 16(8), 5159–5169, doi:10.5194/acp-16-5159-2016, 2016.

Guo, Y., Tian, B., Kahn, R. A., Kalashnikova, O., Wong, S. and Waliser, D. E.: Tropical Atlantic dust and smoke aerosol variations related to the Madden-Julian Oscillation in MODIS and MISR observations, J. Geophys. Res. Atmos., 118(10), 4947–4963, doi:10.1002/jgrd.50409, 2013.

Gupta, P., Levy, R. C., Mattoo, S., Remer, L. A. and Munchak, L. A.: A surface reflectance scheme for retrieving aerosol optical depth over urban surfaces in MODIS Dark Target retrieval algorithm, Atmos. Meas. Tech., 9(7), 3293–3308, doi:10.5194/amt-9-3293-2016, 2016.

Hallquist, M., Wenger, J. C., Baltensperger, U., Rudich, Y., Simpson, D., Claeys, M., Dommen, J., Donahue, N. M., George, C., Goldstein, A. H., Hamilton, J. F., Herrmann, H., Hoffmann, T., Iinuma, Y., Jang, M., Jenkin, M. E., Jimenez, J. L., Kiendler-Scharr, A., Maenhaut, W., McFiggans, G., Mentel, T. F., Monod, A., Prévôt, A. S. H., Seinfeld, J. H., Surratt, J. D., Szmigielski, R. and Wildt, J.: The formation, properties and impact of secondary organic aerosol: current and emerging issues, Atmos. Chem. Phys., 9(14), 5155–5236, doi:10.5194/acp-9-5155-2009, 2009a.

Hallquist, M., Wenger, J. C., Baltensperger, U., Rudich, Y., Simpson, D., Claeys, M., Dommen, J., Donahue, N. M., George, C., Goldstein, A. H., Hamilton, J. F., Herrmann, H., Hoffmann, T., Iinuma, Y., Jang, M., Jenkin, M. E., Jimenez, J. L., Kiendler-Scharr, A., Maenhaut, W., McFiggans, G., Mentel, T. F., Monod, A., Prévôt, A. S. H., Seinfeld, J. H., Surratt, J. D., Szmigielski, R. and Wildt, J.: The formation, properties and impact of secondary organic aerosol: current and emerging issues, Atmos. Chem. Phys., 9(14), 5155–5236, doi:10.5194/acp-9-5155-2009, 2009b.

Hammer, M. S., Martin, R. V., van Donkelaar, A., Buchard, V., Torres, O., Ridley, D. A. and Spurr, R. J. D.: Interpreting the ultraviolet aerosol index observed with the OMI satellite instrument to understand absorption by organic aerosols: implications for atmospheric oxidation and direct radiative effects, Atmos. Chem. Phys., 16(4), 2507–2523, doi:10.5194/acp-16-2507-2016, 2016.

He, T., Liang, S. and Song, D.-X.: Analysis of global land surface albedo climatology and spatial-temporal variation during 1981-2010 from multiple satellite products, J. Geophys. Res. Atmos., 119(17), 10,281-10,298, doi:10.1002/2014JD021667, 2014.

Heald, C. L., J. L. Collett Jr., J. L., Lee, T., Benedict, K. B., Schwandner, F. M., Li, Y., Clarisse, L., Hurtmans, D. R., Van Damme, M., Clerbaux, C., Coheur, P.-F., Philip, S., Martin, R. V. and Pye, H. O. T.: Atmospheric ammonia and particulate inorganic nitrogen over the United States, Atmos. Chem. Phys., 12(21), 10295–10312, doi:10.5194/acp-12-10295-2012, 2012.

Heald, C. L., Ridley, D. A., Kroll, J. H., Barrett, S. R. H., Cady-Pereira, K. E., Alvarado, M. J. and Holmes, C. D.: Contrasting the direct radiative effect and direct radiative forcing of aerosols, Atmos. Chem. Phys., 14(11), 5513–5527, doi:10.5194/acp-14-5513-2014, 2014.

Health Effects Institute: State of Global Air 2019., 2019.

HEI: State of Global Air 2018. Special Report., Boston, MA., 2018.

Henze, D. K. and Seinfeld, J. H.: Global secondary organic aerosol from isoprene oxidation, Geophys. Res. Lett., 33, L09812, doi:doi:10.1029/2006GL025976, 2006.

Henze, D. K., Seinfeld, J. H., Ng, N. L., Kroll, J. H., Fu, T.-M., Jacob, D. J. and Heald, C. L.: Global modeling of secondary organic aerosol formation from aromatic hydrocarbons: high- vs. low-yield pathways, Atmos. Chem. Phys., 8(9), 2405–2420, doi:10.5194/acp-8-2405-2008, 2008.

Herman, J. R., Bhartia, P. K., Torres, O., Hsu, C., Seftor, C. and Celarier, E.: Global distribution of UV-absorbing aerosols from Nimbus 7/TOMS data, J. Geophys. Res., 102(D14), 16911, doi:10.1029/96JD03680, 1997.

Holben, B. N., Eck, T. F., Slutsker, I., Tanré, D., Buis, J. P., Setzer, A., Vermote, E., Reagan, J. A., Kaufman, Y. J., Nakajima, T., Lavenu, F., Jankowiak, I. and Smirnov, A.: AERONET—A Federated Instrument Network and Data Archive for Aerosol Characterization, Remote Sens. Environ., 66(1), 1–16, doi:10.1016/S0034-4257(98)00031-5, 1998.

de Hoogh, K., Chen, J., Gulliver, J., Hoffmann, B., Hertel, O., Ketzel, M., Bauwelinck, M., van Donkelaar, A., Hvidtfeldt, U. A., Katsouyanni, K., Klompmaker, J., Martin, R. V., Samoli, E., Schwartz, P. E., Stafoggia, M., Bellander, T., Strak, M., Wolf, K., Vienneau, D., Brunekreef, B. and Hoek, G.: Spatial PM2.5, NO2, O3 and BC models for Western Europe – Evaluation of spatiotemporal stability, Environ. Int., 120, 81–92, doi:10.1016/j.envint.2018.07.036, 2018.

Hsu, N. C., Gautam, R., Sayer, A. M., Bettenhausen, C., Li, C., Jeong, M. J., Tsay, S.-C. and Holben, B. N.: Global and regional trends of aerosol optical depth over land and ocean using SeaWiFS measurements from 1997 to 2010, Atmos. Chem. Phys. Atmos. Chem. Phys., 12, 8037–8053, doi:10.5194/acp-12-8037-2012, 2012.

Hsu, N. C., Jeong, M.-J., Bettenhausen, C., Sayer, A. M., Hansell, R., Seftor, C. S., Huang, J. and Tsay, S.-C.: Enhanced Deep Blue aerosol retrieval algorithm: The second generation, J. Geophys. Res. Atmos., 118(16), 9296–9315, doi:10.1002/jgrd.50712, 2013.

Hsu, N. C., Lee, J., Sayer, A. M., Kim, W., Bettenhausen, C. and Tsay, S. -C.: VIIRS Deep Blue Aerosol Products Over Land: Extending the EOS Long-Term Aerosol Data Records, J. Geophys. Res. Atmos., 124(7), 4026–4053, doi:10.1029/2018JD029688, 2019.

Huang, J., Minnis, P., Yan, H., Yi, Y., Chen, B., Zhang, L. and Ayers, J. K.: Dust aerosol effect on semi-arid climate over Northwest China detected from A-Train satellite measurements, Atmos. Chem. Phys., 10(14), 6863–6872, doi:10.5194/acp-10-6863-2010, 2010.

Huang, J. P., Liu, J. J., Chen, B. and Nasiri, S. L.: Detection of anthropogenic dust using CALIPSO lidar measurements, Atmos. Chem. Phys., 15(20), 11653–11665, doi:10.5194/acp-15-11653-2015, 2015.

Iacono, M. J., Delamere, J. S., Mlawer, E. J., Shephard, M. W., Clough, S. A. and Collins, W. D.: Radiative forcing by long-lived greenhouse gases: Calculations with the AER radiative transfer models, J. Geophys. Res., 113(D13), D13103, doi:10.1029/2008JD009944, 2008.

Indoitu, R., Kozhoridze, G., Batyrbaeva, M., Vitkovskaya, I., Orlovsky, N., Blumberg, D. and Orlovsky, L.: Dust emission and environmental changes in the dried bottom of the Aral Sea, Aeolian Res., 17, 101–115, doi:10.1016/j.aeolia.2015.02.004, 2015.

IPCC: Climate Change 2014: Impacts, Adaptation, and Vulnerability. Part A: Global and Sectoral Aspects. Contribution of Working Group II to the Fifth Assessment Report of the Intergovernmental Panel on Climate Change [Field, C.B., V.R. Barros, D.J. Dokken, K.J., Cambridge University Press, Cambridge, United Kingdom and New York, NY, USA., 2014.

Israelevich, P. L., Levin, Z., Joseph, J. H. and Ganor, E.: Desert aerosol transport in the Mediterranean region as inferred from the TOMS aerosol index, J. Geophys. Res. Atmos., 107(D21), AAC 13-1-AAC 13-13, doi:10.1029/2001JD002011, 2002.

Jacobson, M. Z.: Studying the effects of aerosols on vertical photolysis rate coefficient and temperature profiles over an urban airshed, J. Geophys. Res., 103(D9), 10593, doi:10.1029/98JD00287, 1998.

Jaeglé, L., Quinn, P. K., Bates, T. S., Alexander, B. and Lin, J.-T.: Global distribution of sea salt aerosols: new constraints from in situ and remote sensing observations, Atmos. Chem. Phys., 11(7), 3137–3157, doi:10.5194/acp-11-3137-2011, 2011.

Jethva, H. and Torres, O.: Satellite-based evidence of wavelength-dependent aerosol absorption in biomass burning smoke inferred from Ozone Monitoring Instrument, Atmos. Chem. Phys., 11(20), 10541–10551, doi:10.5194/acp-11-10541-2011, 2011.

Jin, X., Fiore, A. M., Curci, G., Lyapustin, A., Civerolo, K., Ku, M., van Donkelaar, A. and Martin, R. V.: Assessing uncertainties of a geophysical approach to estimate surface fine particulate matter distributions from satellite-observed aerosol optical depth, Atmos. Chem. Phys., 19(1), 295–313, doi:10.5194/acp-19-295-2019, 2019.

Kahn, R. A. and Gaitley, B. J.: An analysis of global aerosol type as retrieved by MISR, J. Geophys. Res. Atmos., 120(9), 4248–4281, doi:10.1002/2015JD023322, 2015.

Kalashnikova, O. V. and Kahn, R. A.: Mineral dust plume evolution over the Atlantic from MISR and MODIS aerosol retrievals, J. Geophys. Res., 113(D24), D24204, doi:10.1029/2008JD010083, 2008.

Kaskaoutis, D. G., Kharol, S. K., Sifakis, N., Nastos, P. T., Sharma, A. R., Badarinath, K. V. S. and Kambezidis, H. D.: Satellite monitoring of the biomass-burning aerosols during the wildfires of August 2007 in Greece: Climate implications, Atmos. Environ., 45(3), 716–726, doi:10.1016/j.atmosenv.2010.09.043, 2011.

Kirchstetter, T. W. and Thatcher, T. L.: Contribution of organic carbon to wood smoke particulate matter absorption of solar radiation, Atmos. Chem. Phys., 12(14), 6067–6072, doi:10.5194/acp-12-6067-2012, 2012.

Kirchstetter, T. W., Novakov, T. and Hobbs, P. V.: Evidence that the spectral dependence of light absorption by aerosols is affected by organic carbon, J. Geophys. Res. D Atmos., 109(21), D21208, doi:10.1029/2004JD004999, 2004.

Klimont, Z., Smith, S. J. and Cofala, J.: The last decade of global anthropogenic sulfur dioxide: 2000–2011 emissions, Environ. Res. Lett. Environ. Res. Lett, 8(8), 14003–6, doi:10.1088/1748-9326/8/1/014003, 2013.

Klimont, Z., Kupiainen, K., Heyes, C., Purohit, P., Cofala, J., Rafaj, P., Borken-Kleefeld, J. and Schöpp, W.: Global anthropogenic emissions of particulate matter including black carbon, Atmos. Chem. Phys., 17(14), 8681–8723, doi:10.5194/acp-17-8681-2017, 2017.

Koepke, P., Hess, M., Schult, I. and Shettle, E. P.: Global Aerosol Dataset, report, Max-Planck Inst. fur Meteorol., Hamburg, Germany., 1997.

Kristiansen, N. I., Stohl, A., Olivié, D. J. L., Croft, B., Søvde, O. A., Klein, H., Christoudias, T., Kunkel, D., Leadbetter, S. J., Lee, Y. H., Zhang, K., Tsigaridis, K., Bergman, T., Evangeliou, N., Wang, H., Ma, P.-L., Easter, R. C., Rasch, P. J., Liu, X., Pitari, G., Di Genova, G., Zhao, S. Y., Balkanski, Y., Bauer, S. E., Faluvegi, G. S., Kokkola, H., Martin, R. V., Pierce, J. R., Schulz, M., Shindell, D., Tost, H. and Zhang, H.: Evaluation of observed and modelled aerosol lifetimes using radioactive tracers of opportunity and an ensemble of 19 global models, Atmos. Chem. Phys., 16(5), 3525–3561, doi:10.5194/acp-16-3525-2016, 2016.

Kuhns, H., Knipping, E. M. and Vukovich, J. M.: Development of a United States–Mexico Emissions Inventory for the Big Bend Regional Aerosol and Visibility Observational (BRAVO) Study, J. Air Waste Manage. Assoc., 55(5), 677–692, doi:10.1080/10473289.2005.10464648, 2005.

Kumar, N., Chu, A. and Foster, A.: An empirical relationship between PM2.5 and aerosol optical depth in Delhi Metropolitan, Atmos. Environ., 41(21), 4492–4503, doi:10.1016/J.ATMOSENV.2007.01.046, 2007.

Kuwata, M., Zorn, S. R. and Martin, S. T.: Using elemental ratios to predict the density of organic material composed of carbon, hydrogen, and oxygen., Environ. Sci. Technol., 46(2), 787–94, doi:10.1021/es202525q, 2012.

Lack, D. A. and Langridge, J. M.: On the attribution of black and brown carbon light absorption using the Ångström exponent, Atmos. Chem. Phys., 13(20), 10535–10543, doi:10.5194/acp-13-10535-2013, 2013.

Lack, D. A., Tie, X. X., Bofinger, N. D., Wiegand, A. N. and Madronich, S.: Seasonal variability of secondary organic aerosol: A global modeling study, J. Geophys. Res., 109(D3), D03203, doi:10.1029/2003JD003418, 2004.

Lee, C., Martin, R. V., van Donkelaar, A., O'Byrne, G., Krotkov, N., Richter, A., Huey, L. G. and Holloway, J. S.: Retrieval of vertical columns of sulfur dioxide from SCIAMACHY and OMI: Air mass factor algorithm development, validation, and error analysis, J. Geophys. Res., 114(D22), D22303, doi:10.1029/2009JD012123, 2009.

Leibensperger, E. M., Mickley, L. J., Jacob, D. J., Chen, W.-T., Seinfeld, J. H., Nenes, A., Adams, P. J., Streets, D. G., Kumar, N. and Rind, D.: Climatic effects of 1950–2050 changes in US anthropogenic aerosols – Part 2: Climate response, Atmos. Chem. Phys., 12(7), 3349–3362, doi:10.5194/acp-12-3349-2012, 2012.

Levy, R. C., Mattoo, S., Munchak, L. A., Remer, L. A., Sayer, A. M., Patadia, F. and Hsu, N. C.: The Collection 6 MODIS aerosol products over land and ocean, Atmos. Meas. Tech., 6(11), 2989–3034, doi:10.5194/amt-6-2989-2013, 2013.

Li, C., Martin, R. V., van Donkelaar, A., Boys, B. L., Hammer, M. S., Xu, J.-W., Marais, E. A., Reff, A., Strum, M., Ridley, D. A., Crippa, M., Brauer, M. and Zhang, Q.: Trends in Chemical Composition of Global and Regional Population-Weighted Fine Particulate Matter Estimated for 25 Years, Environ. Sci. Technol., acs.est.7b02530, doi:10.1021/acs.est.7b02530, 2017a.

Li, M., Zhang, Q., Kurokawa, J., Woo, J.-H., He, K., Lu, Z., Ohara, T., Song, Y., Streets, D. G., Carmichael, G. R., Cheng, Y., Hong, C., Huo, H., Jiang, X., Kang, S., Liu, F., Su, H. and Zheng, B.: MIX: a mosaic Asian anthropogenic emission inventory under the international collaboration framework of the MICS-Asia and HTAP, Atmos. Chem. Phys., 17(2), 935–963, doi:10.5194/acp-17-935-2017, 2017b.

Li, Z., Zhao, X., Kahn, R., Mishchenko, M., Remer, L., Lee, K.-H., Wang, M., Laszlo, I., Nakajima, T. and Maring, H.: Uncertainties in satellite remote sensing of aerosols and impact on monitoring its long-term trend: a review and perspective, Ann. Geophys., 27(7), 2755–2770, doi:10.5194/angeo-27-2755-2009, 2009.

Liao, H., Adams, P. J., Chung, S. H., Seinfeld, J. H., Mickley, L. J. and Jacob, D. J.: Interactions between tropospheric chemistry and aerosols in a unified general circulation model, J. Geophys. Res., 108(D1), 4001, doi:10.1029/2001JD001260, 2003.

Liao, H., Henze, D. K., Seinfeld, J. H., Wu, S. and Mickley, L. J.: Biogenic secondary organic aerosol over the United States: Comparison of climatological simulations with observations, J. Geophys. Res., 112(D6), D06201, doi:10.1029/2006JD007813, 2007.

Lin, G., Penner, J. E., Flanner, M. G., Sillman, S., Xu, L. and Zhou, C.: Radiative forcing of organic aerosol in the atmosphere and on snow: Effects of SOA and brown carbon, J. Geophys. Res. Atmos., 119(12), 7453–7476, doi:10.1002/2013JD021186, 2014.

Lin, J.-T. and McElroy, M. B.: Impacts of boundary layer mixing on pollutant vertical profiles in the lower troposphere: Implications to satellite remote sensing, Atmos. Environ., 44(14), 1726–1739, doi:10.1016/J.ATMOSENV.2010.02.009, 2010.

Liu, F., Zhang, Q., van der A, R. J., Zheng, B., Tong, D., Yan, L., Zheng, Y. and He, K.: Recent reduction in NO $_x$ emissions over China: synthesis of satellite observations and emission inventories, Environ. Res. Lett., 11(11), 114002, doi:10.1088/1748-9326/11/11/114002, 2016a.

Liu, F., Zhang, Q., van der A, R. J., Zheng, B., Tong, D., Yan, L., Zheng, Y. and He, K.: Recent reduction in NO $_x$ emissions over China: synthesis of satellite observations and emission inventories, Environ. Res. Lett., 11(11), 114002, doi:10.1088/1748-9326/11/11/114002, 2016b.

Liu, J., Bergin, M., Guo, H., King, L., Kotra, N., Edgerton, E. and Weber, R. J.: Size-resolved measurements of brown carbon in water and methanol extracts and estimates of their contribution to ambient fine-particle light absorption, Atmos. Chem. Phys., 13(24), 12389–12404, doi:10.5194/acp-13-12389-2013, 2013.

Liu, J., Scheuer, E., Dibb, J., Diskin, G. S., Ziemba, L. D., Thornhill, K. L., Anderson, B. E., Wisthaler, A., Mikoviny, T., Devi, J. J., Bergin, M., Perring, A. E., Markovic, M. Z., Schwarz, J. P., Campuzano-Jost, P., Day, D. A., Jimenez, J. L. and Weber, R. J.: Brown carbon aerosol in the North American continental troposphere: sources, abundance, and radiative forcing, Atmos. Chem. Phys., 15(14), 7841–7858, doi:10.5194/acp-15-7841-2015, 2015.

Liu, P. F., Abdelmalki, N., Hung, H.-M., Wang, Y., Brune, W. H. and Martin, S. T.: Ultraviolet and visible complex refractive indices of secondary organic material produced by photooxidation of the aromatic compounds toluene and *m*-Xylene, Atmos. Chem. Phys. Discuss., 14(14), 20585–20615, doi:10.5194/acpd-14-20585-2014, 2014.

Liu, Y., Sarnat, J. A., Kilaru, V., Jacob, D. J. and Koutrakis, P.: Estimating ground-level PM2.5 in the eastern United States using satellite remote sensing., Environ. Sci. Technol., 39(9), 3269–78 [online] Available from: http://www.ncbi.nlm.nih.gov/pubmed/15926578 (Accessed 16 February 2019), 2005.

Liu, Y., Koutrakis, P. and Kahn, R.: Estimating fine particulate matter component concentrations and size distributions using satellite-retrieved fractional aerosol optical depth: part 1--method development., J. Air Waste Manag. Assoc., 57(11), 1351–9 [online] Available from: http://www.ncbi.nlm.nih.gov/pubmed/18069458 (Accessed 6 September 2017), 2007.

Lu, Z., Zhang, Q. and Streets, D. G.: Sulfur dioxide and primary carbonaceous aerosol emissions in China and India, Atmos. Chem. Phys. Atmos. Chem. Phys., 11, 9839–9864, doi:10.5194/acp-11-9839-2011, 2011.

Lyapustin, A., Wang, Y., Xiong, X., Meister, G., Platnick, S., Levy, R., Franz, B., Korkin, S., Hilker, T., Tucker, J., Hall, F., Sellers, P., Wu, A. and Angal, A.: Scientific impact of MODIS C5 calibration degradation and C6+ improvements, Atmos. Meas. Tech., 7(12), 4353–4365, doi:10.5194/amt-7-4353-2014, 2014.

Lyapustin, A., Wang, Y., Korkin, S. and Huang, D.: MODIS Collection 6 MAIAC algorithm, Atmos. Meas. Tech., 11(10), 5741–5765, doi:10.5194/amt-11-5741-2018, 2018a.

Lyapustin, A., Wang, Y., Korkin, S. and Huang, D.: MODIS Collection 6 MAIAC algorithm, Atmos. Meas. Tech., 11(10), 5741–5765, doi:10.5194/amt-11-5741-2018, 2018b.

Ma, Z., Hu, X., Huang, L., Bi, J. and Liu, Y.: Estimating Ground-Level PM $_{2.5}$ in China Using Satellite Remote Sensing, Environ. Sci. Technol., 48(13), 7436–7444, doi:10.1021/es5009399, 2014.

Ma, Z., Hu, X., Sayer, A. M., Levy, R., Zhang, Q., Xue, Y., Tong, S., Bi, J., Huang, L. and Liu, Y.: Satellite-Based Spatiotemporal Trends in PM2.5 Concentrations: China, 2004-2013., Environ. Health Perspect., 124(2), 184–92, doi:10.1289/ehp.1409481, 2016.

Mann, M. E. and Emanuel, K. A.: Atlantic hurricane trends linked to climate change, Eos, Trans. Am. Geophys. Union, 87(24), 233, doi:10.1029/2006EO240001, 2006.

Mao, J., Fan, S., Jacob, D. J. and Travis, K. R.: Radical loss in the atmosphere from Cu-Fe redox coupling in aerosols, Atmos. Chem. Phys., 13(2), 509–519, doi:10.5194/acp-13-509-2013, 2013.

Mao, K. B., Ma, Y., Xia, L., Chen, W. Y., Shen, X. Y., He, T. J. and Xu, T. R.: Global aerosol change in the last decade: An analysis based on MODIS data, Atmos. Environ., 94, 680–686, doi:10.1016/j.atmosenv.2014.04.053, 2014.

Marais, E. A., Jacob, D. J., Jimenez, J. L., Campuzano-Jost, P., Day, D. A., Hu, W., Krechmer, J., Zhu, L., Kim, P. S., Miller, C. C., Fisher, J. A., Travis, K., Yu, K., Hanisco, T. F., Wolfe, G. M., Arkinson, H. L., Pye, H. O. T., Froyd, K. D., Liao, J. and McNeill, V. F.: Aqueous-phase mechanism for secondary organic aerosol formation from isoprene: application to the southeast United States and co-benefit of SO₂ emission controls, Atmos. Chem. Phys., 16(3), 1603–1618, doi:10.5194/acp-16-1603-2016, 2016.

Martin, R. V., Jacob, D. J., Yantosca, R. M., Chin, M. and Ginoux, P.: Global and regional decreases in tropospheric oxidants from photochemical effects of aerosols, J. Geophys. Res., 108(D3), 4097, doi:10.1029/2002JD002622, 2003.

Martins, J. V., Artaxo, P., Kaufman, Y. J., Castanho, A. D. and Remer, L. A.: Spectral absorption properties of aerosol particles from 350–2500nm, Geophys. Res. Lett., 36(13), 1–5, doi:10.1029/2009GL037435, 2009.

Martonchik, J. V., Kahn, R. A. and Diner, D. J.: Retrieval of aerosol properties over land using MISR observations, in Satellite Aerosol Remote Sensing over Land, pp. 267–293, Springer Berlin Heidelberg, Berlin, Heidelberg., 2009.

Mauritsen, T.: Arctic climate change: Greenhouse warming unleashed, Nat. Geosci., 9(4), 271–272, doi:10.1038/ngeo2677, 2016.

Mehta, M., Singh, R., Singh, A., Singh, N. and Anshumali: Recent global aerosol optical depth variations and trends — A comparative study using MODIS and MISR level 3 datasets, Remote Sens. Environ., 181, 137–150, doi:10.1016/j.rse.2016.04.004, 2016.

de Meij, A., Pozzer, A. and Lelieveld, J.: Trend analysis in aerosol optical depths and pollutant emission estimates between 2000 and 2009, Atmos. Environ., 51, 75–85, doi:10.1016/j.atmosenv.2012.01.059, 2012.

Mielonen, T., Portin, H., Komppula, M., Leskinen, A., Tamminen, J., Ialongo, I., Hakkarainen, J., Lehtinen, K. E. J. and Arola, A.: Biomass burning aerosols observed in Eastern Finland during the Russian wildfires in summer 2010 – Part 2: Remote sensing, Atmos. Environ., 47, 279–287, doi:10.1016/j.atmosenv.2011.07.016, 2012.

Molod, A., Takacs, L., Suarez, M. and Bacmeister, J.: Development of the GEOS-5 atmospheric general circulation model: evolution from MERRA to MERRA2, Geosci. Model Dev., 8(5), 1339–1356, doi:10.5194/gmd-8-1339-2015, 2015.

Moosmüller, H., Chakrabarty, R. K. and Arnott, W. P.: Aerosol light absorption and its measurement: A review, J. Quant. Spectrosc. Radiat. Transf., 110(11), 844–878, doi:10.1016/j.jqsrt.2009.02.035, 2009.

Mu, M., Randerson, J. T., van der Werf, G. R., Giglio, L., Kasibhatla, P., Morton, D., Collatz, G. J., DeFries, R. S., Hyer, E. J., Prins, E. M., Griffith, D. W. T., Wunch, D., Toon, G. C., Sherlock, V. and Wennberg, P. O.: Daily and 3-hourly variability in global fire emissions and consequences for atmospheric model predictions of carbon monoxide, J. Geophys. Res. Atmos., 116(D24), D24303, doi:10.1029/2011JD016245, 2011.

Naik, V., Voulgarakis, A., Fiore, A. M., Horowitz, L. W., Lamarque, J.-F., Lin, M., Prather, M. J., Young, P. J., Bergmann, D., Cameron-Smith, P. J., Cionni, I., Collins, W. J., Dalsøren, S. B., Doherty, R., Eyring, V., Faluvegi, G., Folberth, G. A., Josse, B., Lee, Y. H., MacKenzie, I. A., Nagashima, T., van Noije, T. P. C., Plummer, D. A., Righi, M., Rumbold, S. T., Skeie, R., Shindell, D. T., Stevenson, D. S., Strode, S., Sudo, K., Szopa, S. and Zeng, G.: Preindustrial to present-day changes in tropospheric hydroxyl radical and methane lifetime from the Atmospheric Chemistry and Climate Model Intercomparison Project (ACCMIP), Atmos. Chem. Phys., 13(10), 5277–5298, doi:10.5194/acp-13-5277-2013, 2013.

Norris, J. R. and Wild, M.: Trends in aerosol radiative effects over Europe inferred from observed cloud cover, solar "dimming," and solar "brightening," J. Geophys. Res., 112(D8), D08214, doi:10.1029/2006JD007794, 2007.

Olivier, J. G. J., Van Aardenne, J. A., Dentener, F. J., Pagliari, V., Ganzeveld, L. N. and Peters, J. A. H. W.: Recent trends in global greenhouse gas emissions:regional trends 1970–2000 and spatial distributionof key sources in 2000, Environ. Sci., 2(2–3), 81–99, doi:10.1080/15693430500400345, 2005.

Park, R. J., Jacob, D. J., Chin, M. and Martin, R. V.: Sources of carbonaceous aerosols over the United States and implications for natural visibility, J. Geophys. Res., 108(D12), 4355, doi:10.1029/2002JD003190, 2003.

Park, R. J., Jacob, D. J., Field, B. D., Yantosca, R. M. and Chin, M.: Natural and transboundary pollution influences on sulfate-nitrate-ammonium aerosols in the United States: Implications for policy, J. Geophys. Res., 109(D15), D15204, doi:10.1029/2003JD004473, 2004a.

Park, R. J., Jacob, D. J., Field, B. D., Yantosca, R. M. and Chin, M.: Natural and transboundary pollution influences on sulfate-nitrate-ammonium aerosols in the United States: Implications for policy, J. Geophys. Res., 109(D15), D15204, doi:10.1029/2003JD004473, 2004b.

Park, R. J., Kim, M. J., Jeong, J. I., Youn, D. and Kim, S.: A contribution of brown carbon aerosol to the aerosol light absorption and its radiative forcing in East Asia, Atmos. Environ., 44(11), 1414–1421, doi:10.1016/j.atmosenv.2010.01.042, 2010.

Pelletier, J. D. and Turcotte, D. L.: Long-range persistence in climatological and hydrological time series: analysis, modeling and application to drought hazard assessment, J. Hydrol., 203(1–4), 198–208, doi:10.1016/S0022-1694(97)00102-9, 1997.

Penning de Vries, M. J. M., Beirle, S. and Wagner, T.: UV Aerosol Indices from SCIAMACHY: introducing the SCattering Index (SCI), Atmos. Chem. Phys., 9(24), 9555–9567, doi:10.5194/acp-9-9555-2009, 2009.

Penning de Vries, M. J. M., Beirle, S., Hörmann, C., Kaiser, J. W., Stammes, P., Tilstra, L. G., Tuinder, O. N. E. and Wagner, T.: A global aerosol classification algorithm incorporating multiple satellite data sets of aerosol and trace gas abundances, Atmos. Chem. Phys., 15(18), 10597–10618, doi:10.5194/acp-15-10597-2015, 2015.

Philip, S., Martin, R. V., van Donkelaar, A., Lo, J. W.-H., Wang, Y., Chen, D., Zhang, L., Kasibhatla, P. S., Wang, S., Zhang, Q., Lu, Z., Streets, D. G., Bittman, S. and Macdonald, D. J.: Global Chemical Composition of Ambient Fine Particulate Matter for Exposure Assessment, Environ. Sci. Technol., 48(22), 13060–13068, doi:10.1021/es502965b, 2014.

Philip, S., Martin, R. V. and Keller, C. A.: Sensitivity of chemistry-transport model simulations to the duration of chemical and transport operators: a case study with GEOS-Chem v10-01, Geosci. Model Dev., 9(5), 1683–1695, doi:10.5194/gmd-9-1683-2016, 2016.

Philip, S., Martin, R. V, Snider, G., Weagle, C. L., van Donkelaar, A., Brauer, M., Henze, D. K., Klimont, Z., Venkataraman, C., Guttikunda, S. K. and Zhang, Q.: Anthropogenic fugitive, combustion and industrial dust is a significant, underrepresented fine particulate matter source in global atmospheric models, Environ. Res. Lett., 12(4), 044018, doi:10.1088/1748-9326/aa65a4, 2017a.

Philip, S., Martin, R. V, Snider, G., Weagle, C. L., van Donkelaar, A., Brauer, M., Henze, D. K., Klimont, Z., Venkataraman, C., Guttikunda, S. K. and Zhang, Q.: Anthropogenic fugitive, combustion and industrial dust is a significant, underrepresented fine particulate matter source in global atmospheric models, Environ. Res. Lett., 12(4), 044018, doi:10.1088/1748-9326/aa65a4, 2017b.

Pope, C. A., Ezzati, M. and Dockery, D. W.: Fine-Particulate Air Pollution and Life Expectancy in the United States, N. Engl. J. Med., 360(4), 376–386, doi:10.1056/NEJMsa0805646, 2009.

Pöschl, U.: Atmospheric Aerosols: Composition, Transformation, Climate and Health Effects, Angew. Chemie Int. Ed., 44(46), 7520–7540, doi:10.1002/anie.200501122, 2005.

Povey, A. C. and Grainger, R. G.: Known and unknown unknowns: uncertainty estimation in satellite remote sensing, Atmos. Meas. Tech., 8(11), 4699–4718, doi:10.5194/amt-8-4699-2015, 2015.

Prather, M. J., Holmes, C. D. and Hsu, J.: Reactive greenhouse gas scenarios: Systematic exploration of uncertainties and the role of atmospheric chemistry, Geophys. Res. Lett., 39(9), L09803, doi:10.1029/2012GL051440, 2012.

Prinn, R., Cunnold, D., Simmonds, P., Alyea, F., Boldi, R., Crawford, A., Fraser, P., Gutzler, D., Hartley, D., Rosen, R. and Rasmussen, R.: Global average concentration and trend for hydroxyl radicals deduced from ALE/GAGE trichloroethane (methyl chloroform) data for 1978–1990, J. Geophys. Res., 97(D2), 2445, doi:10.1029/91JD02755, 1992.

Prinn, R. G., Huang, J., Weiss, R. F., Cunnold, D. M., Fraser, P. J., Simmonds, P. G., McCulloch, A., Harth, C., Reimann, S., Salameh, P., O'Doherty, S., Wang, R. H. J., Porter, L. W., Miller, B. R. and Krummel, P. B.: Evidence for variability of atmospheric hydroxyl radicals over the past quarter century, Geophys. Res. Lett., 32(7), L07809, doi:10.1029/2004GL022228, 2005.

Pye, H. O. T., Liao, H., Wu, S., Mickley, L. J., Jacob, D. J., Henze, D. K. and Seinfeld, J. H.: Effect of changes in climate and emissions on future sulfate-nitrate-ammonium aerosol levels in the United States, J. Geophys. Res., 114(D1), D01205, doi:10.1029/2008JD010701, 2009a.

Pye, H. O. T., Liao, H., Wu, S., Mickley, L. J., Jacob, D. J., Henze, D. K. and Seinfeld, J. H.: Effect of changes in climate and emissions on future sulfate-nitrate-ammonium aerosol levels in the United States, J. Geophys. Res. Atmos., 114(D1), doi:10.1029/2008JD010701, 2009b.

Pye, H. O. T., Chan, A. W. H., Barkley, M. P. and Seinfeld, J. H.: Global modeling of organic aerosol: the importance of reactive nitrogen (NO_x and NO₃), Atmos. Chem. Phys., 10(22), 11261–11276, doi:10.5194/acp-10-11261-2010, 2010.

Ramanathan, V. and Carmichael, G.: Global and regional climate changes due to black carbon, Nat. Geosci., 1(4), 221–227, doi:10.1038/ngeo156, 2008.

Reynolds, R. W. and Reynolds, R. W.: A Real-Time Global Sea Surface Temperature Analysis, J. Clim., 1(1), 75–87, doi:10.1175/1520-0442(1988)001<0075:ARTGSS>2.0.CO;2, 1988.

Ridley, D. A., Heald, C. L. and Ford, B.: North African dust export and deposition: A satellite and model perspective, J. Geophys. Res., 117(D2), D02202, doi:10.1029/2011JD016794, 2012.

Rizzo, L. V., Correia, A. L., Artaxo, P., Procápio, A. S. and Andreae, M. O.: Spectral dependence of aerosol light absorption over the Amazon Basin, Atmos. Chem. Phys., 11(17), 8899–8912, doi:10.5194/acp-11-8899-2011, 2011.

Russell, P. B., Bergstrom, R. W., Shinozuka, Y., Clarke, A. D., DeCarlo, P. F., Jimenez, J. L., Livingston, J. M., Redemann, J., Holben, B., Dubovik, O. and Strawa, A.: Absorption Angstrom Exponent in AERONET and related data as an indicator of aerosol composition, Atmos. Chem. Phys. Discuss., 9(5), 21785–21817, doi:10.5194/acpd-9-21785-2009, 2009.

Saleh, R., Robinson, E. S., Tkacik, D. S., Ahern, A. T., Liu, S., Aiken, A. C., Sullivan, R. C., Presto, A. A., Dubey, M. K., Yokelson, R. J., Donahue, N. M. and Robinson, A. L.: Brownness of organics in aerosols from biomass burning linked to their black carbon content, Nat. Geosci., 7(9), 647–650, doi:10.1038/ngeo2220, 2014.

Sayer, A. M., Hsu, N. C., Bettenhausen, C., Jeong, M.-J., Holben, B. N. and Zhang, J.: Global and regional evaluation of over-land spectral aerosol optical depth retrievals from SeaWiFS, Atmos. Meas. Tech., 5(7), 1761–1778, doi:10.5194/amt-5-1761-2012, 2012.

Sayer, A. M., Munchak, L. A., Hsu, N. C., Levy, R. C., Bettenhausen, C. and Jeong, M.-J.: MODIS Collection 6 aerosol products: Comparison between Aqua's e-Deep Blue, Dark Target, and "merged" data sets, and usage recommendations, J. Geophys. Res. Atmos., 119(24), 13,965-13,989, doi:10.1002/2014JD022453, 2014.

Sayer, A. M., Hsu, N. C., Lee, J., Kim, W. V. and Dutcher, S. T.: Validation, Stability, and Consistency of MODIS Collection 6.1 and VIIRS Version 1 Deep Blue Aerosol Data Over Land, J. Geophys. Res. Atmos., 124(8), 4658–4688, doi:10.1029/2018JD029598, 2019.

Schenkeveld, V. M. E., Jaross, G., Marchenko, S., Haffner, D., Kleipool, Q. L., Rozemeijer, N. C., Veefkind, J. P. and Levelt, P. F.: In-flight performance of the Ozone Monitoring Instrument, Atmos. Meas. Tech., 10(5), 1957–1986, doi:10.5194/amt-10-1957-2017, 2017.

Schepanski, K., Tegen, I., Laurent, B., Heinold, B. and Macke, A.: A new Saharan dust source activation frequency map derived from MSG-SEVIRI IR-channels, Geophys. Res. Lett., 34(18), L18803, doi:10.1029/2007GL030168, 2007.

Schultz, M., Rast, S., for Meteorology, M., Authors, H., van het Bolscher, M., Pulles, T., Brand, R., Jose Pereira, A., Mota, B., Allan Spessa, L., for Biogeochemistry, M. and Szopa, S.: REanalysis of the TROpospheric chemical composition over the past 40 years A long-term global modeling study of tropospheric chemistry funded under the 5 th EU framework programme EU-Contract N o Emission data sets and methodologies for estimating emissions Work Package 1, Deliverable D1-6 Editor: (modified Annex 4) RETRO deliverable D1-6: Report on emissions / 2 RETRO deliverable D1-6: Report on emissions / 3. [online] Available from: http://citeseerx.ist.psu.edu/viewdoc/download?doi=10.1.1.612.9945&rep=rep1&type=pdf (Accessed 31 July 2019), n.d.

Schwartz, S. E.: The whitehouse effect—Shortwave radiative forcing of climate by anthropogenic aerosols: an overview, J. Aerosol Sci., 27(3), 359–382, doi:10.1016/0021-8502(95)00533-1, 1996.

Scollo, S., Kahn, R. A., Nelson, D. L., Coltelli, M., Diner, D. J., Garay, M. J. and Realmuto, V. J.: MISR observations of Etna volcanic plumes, J. Geophys. Res. Atmos., 117(D6), n/a-n/a, doi:10.1029/2011JD016625, 2012.

Seinfeld, J. H. and Pandis, S. N.: Atmospheric chemistry and physics : from air pollution to climate change. [online] Available from: https://www.wiley.com/en-us/Atmospheric+Chemistry+and+Physics%3A+From+Air+Pollution+to+Climate+Change%2C+3rd+Edition-p-9781118947401 (Accessed 6 February 2019).

Shaddick, G., Thomas, M. L., Green, A., Brauer, M., van Donkelaar, A., Burnett, R., Chang, H. H., Cohen, A., Dingenen, R. Van, Dora, C., Gumy, S., Liu, Y., Martin, R., Waller, L. A., West, J., Zidek, J. V. and Prüss-Ustün, A.: Data integration model for air quality: a hierarchical approach to the global estimation of exposures to ambient air pollution, J. R. Stat. Soc. Ser. C (Applied Stat., 67(1), 231–253, doi:10.1111/rssc.12227, 2018.

Shao, Y., Klose, M. and Wyrwoll, K.-H.: Recent global dust trend and connections to climate forcing, J. Geophys. Res. Atmos., 118(19), 11,107-11,118, doi:10.1002/jgrd.50836, 2013.

Shi, W. and Wang, M.: Decadal changes of water properties in the Aral Sea observed by MODIS-Aqua, J. Geophys. Res. Ocean., 120(7), 4687–4708, doi:10.1002/2015JC010937, 2015.

Shi, W., Wang, M. and Guo, W.: Long-term hydrological changes of the Aral Sea observed by satellites, J. Geophys. Res. Ocean., 119(6), 3313–3326, doi:10.1002/2014JC009988, 2014.

Simon, H., Reff, A., Wells, B., Xing, J. and Frank, N.: Ozone Trends Across the United States over a Period of Decreasing NOx and VOC Emissions, Environ. Sci. Technol., 49(1), 186–195, doi:10.1021/es504514z, 2015.

Sokolik, I. N. and Toon, O. B.: Direct radiative forcing by anthropogenic airborne mineral aerosols, Nature, 381(6584), 681–683, doi:10.1038/381681a0, 1996.

Sokolik, I. N. and Toon, O. B.: Incorporation of mineralogical composition into models of the radiative properties of mineral aerosol from UV to IR wavelengths, J. Geophys. Res. Atmos., 104(D8), 9423–9444, doi:10.1029/1998JD200048, 1999.

Song, W., Jia, H., Huang, J. and Zhang, Y.: A satellite-based geographically weighted regression model for regional PM2.5 estimation over the Pearl River Delta region in China, Remote Sens. Environ., 154, 1–7, doi:10.1016/J.RSE.2014.08.008, 2014.

Spivak, L., Terechov, A., Vitkovskaya, I., Batyrbayeva, M. and Orlovsky, L.: Dynamics of Dust Transfer from the Desiccated Aral Sea Bottom Analysed by Remote Sensing, pp. 97–106, Springer, Berlin, Heidelberg., 2012.

Spivakovsky, C. M., Logan, J. A., Montzka, S. A., Balkanski, Y. J., Foreman-Fowler, M., Jones, D. B. A., Horowitz, L. W., Fusco, A. C., Brenninkmeijer, C. A. M., Prather, M. J., Wofsy, S. C. and McElroy, M. B.: Three-dimensional climatological distribution of tropospheric OH: Update and evaluation, J. Geophys. Res., 105(D7), 8931, doi:10.1029/1999JD901006, 2000.

Spurr, R. J. D.: VLIDORT: A linearized pseudo-spherical vector discrete ordinate radiative transfer code for forward model and retrieval studies in multilayer multiple scattering media, J. Quant. Spectrosc. Radiat. Transf., 102(2), 316–342, doi:10.1016/j.jqsrt.2006.05.005, 2006.

Stier, P., Seinfeld, J. H., Kinne, S. and Boucher, O.: Aerosol absorption and radiative forcing, Atmos. Chem. Phys., 7(19), 5237–5261, doi:10.5194/acp-7-5237-2007, 2007.

Storelvmo, T., Leirvik, T., Lohmann, U., Phillips, P. C. B. and Wild, M.: Disentangling greenhouse warming and aerosol cooling to reveal Earth's climate sensitivity, Nat. Geosci., 9(4), 286–289, doi:10.1038/ngeo2670, 2016.

Sun, H., Biedermann, L. and Bond, T. C.: Color of brown carbon: A model for ultraviolet and visible light absorption by organic carbon aerosol, Geophys. Res. Lett., 34(17), L17813, doi:10.1029/2007GL029797, 2007.

Tegen, I. and Lacis, A. A.: Modeling of particle size distribution and its influence on the radiative properties of mineral dust aerosol, J. Geophys. Res. Atmos., 101(D14), 19237–19244, doi:10.1029/95JD03610, 1996.

Torres, O., Bhartia, P. K., Herman, J. R., Ahmad, Z. and Gleason, J.: Derivation of aerosol properties from satellite measurements of backscattered ultraviolet radiation: Theoretical basis, J. Geophys. Res., 103(D14), 17099, doi:10.1029/98JD00900, 1998.

Torres, O., Bhartia, P. K., Sinyuk, A., Welton, E. J. and Holben, B.: Total Ozone Mapping Spectrometer measurements of aerosol absorption from space: Comparison to SAFARI 2000 ground-based observations, J. Geophys. Res., 110(D10), D10S18, doi:10.1029/2004JD004611, 2005.

Torres, O., Tanskanen, A., Veihelmann, B., Ahn, C., Braak, R., Bhartia, P. K., Veefkind, P. and Levelt, P.: Aerosols and surface UV products from Ozone Monitoring Instrument observations: An overview, J. Geophys. Res., 112(D24), D24S47, doi:10.1029/2007JD008809, 2007.

Torres, O., Chen, Z., Jethva, H., Ahn, C., Freitas, S. R. and Bhartia, P. K.: OMI and MODIS observations of the anomalous 2008–2009 Southern Hemisphere biomass burning seasons, Atmos. Chem. Phys., 10(8), 3505–3513, doi:10.5194/acp-10-3505-2010, 2010.

Torres, O., Ahn, C. and Chen, Z.: Improvements to the OMI near-UV aerosol algorithm using A-train CALIOP and AIRS observations, Atmos. Meas. Tech., 6(11), 3257–3270, doi:10.5194/amt-6-3257-2013, 2013.

Torres, O., Bhartia, P. K., Jethva, H. and Ahn, C.: Impact of the ozone monitoring instrument row anomaly on the long-term record of aerosol products, Atmos. Meas. Tech., 11(5), 2701–2715, doi:10.5194/amt-11-2701-2018, 2018.

Travis, K. R., Jacob, D. J., Fisher, J. A., Kim, P. S., Marais, E. A., Zhu, L., Yu, K., Miller, C. C., Yantosca, R. M., Sulprizio, M. P., Thompson, A. M., Wennberg, P. O., Crounse, J. D., St. Clair, J. M., Cohen, R. C., Laughner, J. L., Dibb, J. E., Hall, S. R., Ullmann, K., Wolfe, G. M., Pollack, I. B., Peischl, J., Neuman, J. A. and Zhou, X.: Why do models overestimate surface ozone in the Southeast United States?, Atmos. Chem. Phys., 16(21), 13561–13577, doi:10.5194/acp-16-13561-2016, 2016.

Tsigaridis, K. and Kanakidou, M.: Global modelling of secondary organic aerosol in the troposphere: a sensitivity analysis, Atmos. Chem. Phys., 3(5), 1849–1869, doi:10.5194/acp-3-1849-2003, 2003.

Turnock, S. T., Butt, E. W., Richardson, T. B., Mann, G. W., Reddington, C. L., Forster, P. M., Haywood, J., Crippa, M., Janssens-Maenhout, G., Johnson, C. E., Bellouin, N., Carslaw, K. S. and Spracklen, D. V: Environmental Research Letters The impact of European legislative and technology measures to reduce air pollutants on air quality, human health and climate, Environ. Res. Lett, 11, 24010, doi:10.1088/1748-9326/11/2/024010, 2016.

Veefkind, J. P., Aben, I., McMullan, K., Förster, H., de Vries, J., Otter, G., Claas, J., Eskes, H. J., de Haan, J. F., Kleipool, Q., van Weele, M., Hasekamp, O., Hoogeveen, R., Landgraf, J., Snel, R., Tol, P., Ingmann, P., Voors, R., Kruizinga, B., Vink, R., Visser, H. and Levelt, P. F.: TROPOMI on the ESA Sentinel-5 Precursor: A GMES mission for global observations of the atmospheric composition for climate, air quality and ozone layer applications, Remote Sens. Environ., 120, 70–83, doi:10.1016/J.RSE.2011.09.027, 2012.

Wang, S., Zhang, Q., Martin, R. V, Philip, S., Liu, F., Li, M., Jiang, X. and He, K.: Satellite measurements oversee China's sulfur dioxide emission reductions from coal-fired power plants, Environ. Res. Lett., 10(11), 114015, doi:10.1088/1748-9326/10/11/114015, 2015.

Wang, X., Heald, C. L., Ridley, D. A., Schwarz, J. P., Spackman, J. R., Perring, A. E., Coe, H., Liu, D. and Clarke, A. D.: Exploiting simultaneous observational constraints on mass and absorption to estimate the global direct radiative forcing of black carbon and brown carbon, Atmos. Chem. Phys., 14(20), 10989–11010, doi:10.5194/acp-14-10989-2014, 2014.

Weatherhead, E. C., Reinsel, G. C., Tiao, G. C., Meng, X.-L., Choi, D., Cheang, W.-K., Keller, T., DeLuisi, J., Wuebbles, D. J., Kerr, J. B., Miller, A. J., Oltmans, S. J. and Frederick, J. E.: Factors affecting the detection of trends: Statistical considerations and applications to environmental data, J. Geophys. Res. Atmos., 103(D14), 17149–17161, doi:10.1029/98JD00995, 1998.

Weatherhead, E. C., Stevermer, A. J. and Schwartz, B. E.: Detecting environmental changes and trends, Phys. Chem. Earth, Parts A/B/C, 27(6–8), 399–403, doi:10.1016/S1474-7065(02)00019-0, 2002.

West, J. J., Cohen, A., Dentener, F., Brunekreef, B., Zhu, T., Armstrong, B., Bell, M. L., Brauer, M., Carmichael, G., Costa, D. L., Dockery, D. W., Kleeman, M., Krzyzanowski, M., Künzli, N., Liousse, C., Lung, S.-C. C., Martin, R. V., Pöschl, U., Pope, C. A., Roberts, J. M., Russell, A. G. and Wiedinmyer, C.: "What We Breathe Impacts Our Health: Improving Understanding of the Link between Air Pollution and Health," Environ. Sci. Technol., 50(10), 4895–4904, doi:10.1021/acs.est.5b03827, 2016.

Wilks, D. S.: Statistical methods in the atmospheric sciences, Academic Press., 2011.

World Health Organization: WHO Global Ambient Air Quality Database (update 2018), 2018.

Xie, M., Chen, X., Hays, M. D., Lewandowski, M., Offenberg, J., Kleindienst, T. E. and Holder, A. L.: Light Absorption of Secondary Organic Aerosol: Composition and Contribution of Nitroaromatic Compounds, Environ. Sci. Technol., 51(20), 11607–11616, doi:10.1021/acs.est.7b03263, 2017.

Xing, J., Mathur, R., Pleim, J., Hogrefe, C., Gan, C.-M., Wong, D. C., Wei, C., Gilliam, R. and Pouliot, G.: Observations and modeling of air quality trends over 1990–2010 across the Northern Hemisphere: China, the United States and Europe, Atmos. Chem. Phys., 15(5), 2723–2747, doi:10.5194/acp-15-2723-2015, 2015.

Yang, M., Howell, S. G., Zhuang, J. and Huebert, B. J.: Attribution of aerosol light absorption to black carbon, brown carbon, and dust in China- interpretations of atmospheric measurements during EAST-AIRE, Atmos. Chem. Phys. Discuss., 8(3), 10913–10954, doi:10.5194/acpd-8-10913-2008, 2008.

Yevich, R. and Logan, J. A.: An assessment of biofuel use and burning of agricultural waste in the developing world, Global Biogeochem. Cycles, 17(4), 1095, doi:10.1029/2002GB001952, 2003.

Zhang, L., Jacob, D. J., Kopacz, M., Henze, D. K., Singh, K. and Jaffe, D. A.: Intercontinental source attribution of ozone pollution at western U.S. sites using an adjoint method, Geophys. Res. Lett., 36, L11810 [online] Available from: http://dash.harvard.edu/handle/1/3627131 (Accessed 9 May 2015), 2009.

Zhang, L., Kok, J. F., Henze, D. K., Li, Q. and Zhao, C.: Improving simulations of fine dust surface concentrations over the western United States by optimizing the particle size distribution, Geophys. Res. Lett., 40(12), 3270–3275, doi:10.1002/grl.50591, 2013a.

Zhang, L., Henze, D. K., Grell, G. A., Torres, O., Jethva, H. and Lamsal, L. N.: What factors control the trend of increasing AAOD over the United States in the last decade?, J. Geophys. Res. Atmos., 122(3), 1797–1810, doi:10.1002/2016JD025472, 2017.

Zhang, M., Wang, Y., Ma, Y., Wang, L., Gong, W. and Liu, B.: Spatial distribution and temporal variation of aerosol optical depth and radiative effect in South China and its adjacent area, Atmos. Environ., 188, 120–128, doi:10.1016/J.ATMOSENV.2018.06.028, 2018.

Zhang, X., Lin, Y.-H., Surratt, J. D. and Weber, R. J.: Sources, composition and absorption Ångström exponent of light-absorbing organic components in aerosol extracts from the Los Angeles Basin., Environ. Sci. Technol., 47(8), 3685–93, doi:10.1021/es305047b, 2013b.

Zhang, Y., Wallace, J. M., Battisti, D. S., Zhang, Y., Wallace, J. M. and Battisti, D. S.: ENSO-like Interdecadal Variability: 1900–93, J. Clim., 10(5), 1004–1020, doi:10.1175/1520-0442(1997)010<1004:ELIV>2.0.CO;2, 1997.

Zhao, B., Wang, S. X., Liu, H., Xu, J. Y., Fu, K., Klimont, Z., Hao, J. M., He, K. B., Cofala, J. and Amann, M.: NO x emissions in China: historical trends and future perspectives, Atmos. Chem. Phys, 13, 9869–9897, doi:10.5194/acp-13-9869-2013, 2013.

Zhong, M. and Jang, M.: Dynamic light absorption of biomass-burning organic carbon photochemically aged under natural sunlight, Atmos. Chem. Phys., 14(3), 1517–1525, doi:10.5194/acp-14-1517-2014, 2014.